NIST Special Publication 1018-5

Fire Dynamics Simulator (Version 5) Technical Reference Guide

Volume 1: Mathematical Model

Kevin McGrattan
Simo Hostikka
Jason Floyd
Howard Baum
Ronald Rehm
William Mell
Randall McDermott

In cooperation with:
VTT Technical Research Centre of Finland

NIST

**National Institute of
Standards and Technology**
U.S. Department of Commerce

NIST Special Publication 1018-5

Fire Dynamics Simulator (Version 5) Technical Reference Guide

Volume 1: Mathematical Model

Kevin McGrattan
Howard Baum
Ronald Rehm
William Mell
Randall McDermott
Fire Research Division
Building and Fire Research Laboratory

Simo Hostikka
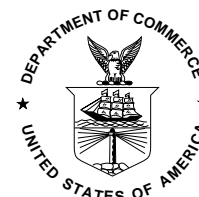*VTT Technical Research Centre of Finland*
Espoo, Finland

Jason Floyd
Hughes Associates, Inc.
Baltimore, Maryland, USA

U.S. Department of Commerce
Gary Locke, Secretary

National Institute of Standards and Technology
Patrick Gallagher, Acting Director

Preface

This document provides the theoretical basis for the Fire Dynamics Simulator (FDS), following the general framework set forth in the "Standard Guide for Evaluating the Predictive Capability of Deterministic Fire Models," ASTM E 1355 [1]. It is the first of a four volume set of companion documents, referred to collectively as the FDS Technical Reference Guide [2]. Volumes 2, 3 and 4 describe the model verification, experimental validation, and configuration management, respectively.

A separate document, *Fire Dynamics Simulator, User's Guide* [3] describes how the FDS software is actually used.

Disclaimer

The US Department of Commerce makes no warranty, expressed or implied, to users of the Fire Dynamics Simulator (FDS), and accepts no responsibility for its use. Users of FDS assume sole responsibility under Federal law for determining the appropriateness of its use in any particular application; for any conclusions drawn from the results of its use; and for any actions taken or not taken as a result of analysis performed using these tools.

Users are warned that FDS is intended for use only by those competent in the fields of fluid dynamics, thermodynamics, heat transfer, combustion, and fire science, and is intended only to supplement the informed judgment of the qualified user. The software package is a computer model that may or may not have predictive capability when applied to a specific set of factual circumstances. Lack of accurate predictions by the model could lead to erroneous conclusions with regard to fire safety. All results should be evaluated by an informed user.

Throughout this document, the mention of computer hardware or commercial software does not constitute endorsement by NIST, nor does it indicate that the products are necessarily those best suited for the intended purpose.

About the Authors

Kevin McGrattan is a mathematician in the Building and Fire Research Laboratory (BFRL) of NIST. He received a bachelors of science degree from the School of Engineering and Applied Science of Columbia University in 1987 and a doctorate at the Courant Institute of New York University in 1991. He joined the NIST staff in 1992 and has since worked on the development of fire models, most notably the Fire Dynamics Simulator.

Simo Hostikka is a Senior Research Scientist at VTT Technical Research Centre of Finland. He received a master of science (technology) degree in 1997 and a doctorate in 2008 from the Department of Engineering Physics and Mathematics of the Helsinki University of Technology. He is the principal developer of the radiation and solid phase sub-models within FDS.

Jason Floyd is a Senior Engineer at Hughes Associates, Inc., in Baltimore, Maryland. He received a bachelors of science and Ph.D. in the Nuclear Engineering Program of the University of Maryland. After graduating, he won a National Research Council Post-Doctoral Fellowship at the Building and Fire Research Laboratory of NIST, where he developed the combustion algorithm within FDS. He is currently funded by NIST under grant 70NANB8H8161 from the Fire Research Grants Program (15 USC 278f). He is the principal developer of the multi-parameter mixture fraction combustion model and control logic within FDS.

Howard Baum is a NIST Fellow *emeritus*. He received a bachelors of science degree from Brooklyn Polytechnic Institute in 1957 and a doctorate from Harvard University in 1964. After joining the staff of the National Bureau of Standards (now NIST), he, along with Ronald Rehm, developed the low Mach number formulation of the Navier-Stokes equations that is still the core transport algorithm within FDS.

Ronald Rehm is a former NIST fellow, currently retired but still active in a number of projects at NIST. He received a bachelors of science degree from Purdue University in 1960 and a doctorate from the Massachusetts Institute of Technology in 1965. Along with Howard Baum, he formulated the original numerical scheme that evolved over 25 years into the current FDS solver.

Randall McDermott joined the research staff of the Building and Fire Research Lab in 2008. He received a B.S. degree from the University of Tulsa in Chemical Engineering in 1994 and a doctorate at the University of Utah in 2005. His research interests include subgrid-scale models and numerical methods for large-eddy simulation, adaptive mesh refinement, immersed boundary methods, and Lagrangian particle methods.

William (Ruddy) Mell is an applied mathematician in BFRL. He holds a B.S. degree from the University of Minnesota (1994) and doctorate from the University of Washington (1994). His research interests include the development of large eddy simulation methods and sub-models applicable to the physics of large fires in buildings, vegetation, and the wildland-urban interface.

Acknowledgments

The development and maintenance of the Fire Dynamics Simulator has been made possible through a partnership of public and private organizations, both in the United States and abroad. Following is a list of contributors from the various sectors of the fire research, fire protection engineering and fire services communities:

FDS is supported financially via internal funding at both NIST and VTT, Finland. In addition, support is provided by other agencies of the US Federal Government:

- The US Nuclear Regulatory Commission Office of Research has funded key validation experiments, the preparation of the FDS manuals, and the development of various sub-models that are of importance in the area of nuclear power plant safety. Special thanks to Mark Salley and Jason Dreisbach for their efforts and support. The Office of Nuclear Material Safety and Safeguards, another branch of the US NRC, has supported modeling studies of tunnel fires under the direction of Chris Bajwa and Allen Hansen.

- The Micro-Gravity Combustion Program of the National Aeronautics and Space Administration (NASA) has supported several projects that directly or indirectly benefited FDS development.

- The US Forest Service has supported the development of sub-models in FDS designed to simulate the spread of fire in the Wildland Urban Interface (WUI). Special thanks to Mark Finney and Tony Bova for their support.

- The Minerals Management Service of the US Department of the Interior funded research at NIST aimed at characterizing the burning behavior of oil spilled on the open sea or ice. Part of this research led to the development of the ALOFT (A Large Outdoor Fire plume Trajectory) model, a forerunner of FDS. Special thanks to Joe Mullin for his encouragement of the modeling efforts.

The following individuals and organizations played a role in the development of the underlying mathematical model of FDS.

- Originally, the basic hydrodynamic solver was designed by Ronald Rehm and Howard Baum with programming help from Darcy Barnett, Dan Lozier and Hai Tang of the Computing and Applied Mathematics Laboratory (CAML) at NIST, and Dan Corley of the Building and Fire Research Laboratory (BFRL). Jim Sims of CAML developed the original visualization software. The direct pressure solver was written by Roland Sweet of the National Center for Atmospheric Research (NCAR), Boulder, Colorado.

- Kuldeep Prasad added the multiple-mesh data structures, paving the way for parallel processing. Charles Bouldin devised the basic framework of the parallel version of the code.

- William Grosshandler and Tom Cleary, both currently at NIST, developed an enhancement to the smoke detector activation algorithm, originally conceived by Gunnar Heskestad of Factory Mutual.

Contents

Chapter 1

Introduction

Howard Baum, NIST Fellow Emeritus

The idea that the dynamics of a fire might be studied numerically dates back to the beginning of the computer age. Indeed, the fundamental conservation equations governing fluid dynamics, heat transfer, and combustion were first written down over a century ago. Despite this, practical mathematical models of fire (as distinct from controlled combustion) are relatively recent due to the inherent complexity of the problem. Indeed, in his brief history of the early days of fire research, Hoyt Hottel noted "A case can be made for fire being, next to the life processes, the most complex of phenomena to understand" [4].

The difficulties revolve about three issues: First, there are an enormous number of possible fire scenarios to consider due to their accidental nature. Second, the physical insight and computing power required to perform all the necessary calculations for most fire scenarios are limited. Any fundamentally based study of fires must consider at least some aspects of bluff body aerodynamics, multi-phase flow, turbulent mixing and combustion, radiative transport, and conjugate heat transfer; all of which are active research areas in their own right. Finally, the "fuel" in most fires was never intended as such. Thus, the mathematical models and the data needed to characterize the degradation of the condensed phase materials that supply the fuel may not be available. Indeed, the mathematical modeling of the physical and chemical transformations of real materials as they burn is still in its infancy.

In order to make progress, the questions that are asked have to be greatly simplified. To begin with, instead of seeking a methodology that can be applied to all fire problems, we begin by looking at a few scenarios that seem to be most amenable to analysis. Hopefully, the methods developed to study these "simple" problems can be generalized over time so that more complex scenarios can be analyzed. Second, we must learn to live with idealized descriptions of fires and approximate solutions to our idealized equations. Finally, the methods should be capable of systematic improvement. As our physical insight and computing power grow more powerful, the methods of analysis can grow with them.

To date, three distinct approaches to the simulation of fires have emerged. Each of these treats the fire as an inherently three dimensional process evolving in time. The first to reach maturity, the "zone" models, describe compartment fires. Each compartment is divided into two spatially homogeneous volumes, a hot upper layer and a cooler lower layer. Mass and energy balances are enforced for each layer, with additional models describing other physical processes appended as differential or algebraic equations as appropriate. Examples of such phenomena include fire plumes, flows through doors, windows and other vents, radiative and convective heat transfer, and solid fuel pyrolysis. Descriptions of the physical and mathematical assumptions behind the zone modeling concept are given in separate papers by Jones [5] and Quintiere [6], who chronicle developments through 1983. Model development since then has progressed to the point where documented and supported software implementing these models are widely available [7].

The relative physical and computational simplicity of the zone models has led to their widespread use in

1

the analysis of fire scenarios. So long as detailed spatial distributions of physical properties are not required, and the two layer description reasonably approximates reality, these models are quite reliable. However, by their very nature, there is no way to systematically improve them. The rapid growth of computing power and the corresponding maturing of computational fluid dynamics (CFD), has led to the development of CFD based "field" models applied to fire research problems. Virtually all this work is based on the conceptual framework provided by the Reynolds-averaged form of the Navier-Stokes equations (RANS), in particular the $k - \varepsilon$ turbulence model pioneered by Patankar and Spalding [8]. The use of CFD models has allowed the description of fires in complex geometries, and the incorporation of a wide variety of physical phenomena. However, these models have a fundamental limitation for fire applications – the averaging procedure at the root of the model equations.

RANS models were developed as a time-averaged approximation to the conservation equations of fluid dynamics. While the precise nature of the averaging time is not specified, it is clearly long enough to require the introduction of large eddy transport coefficients to describe the unresolved fluxes of mass, momentum and energy. This is the root cause of the smoothed appearance of the results of even the most highly resolved fire simulations. The smallest resolvable length scales are determined by the product of the local velocity and the averaging time rather than the spatial resolution of the underlying computational grid. This property of RANS models is typically exploited in numerical computations by using implicit numerical techniques to take large time steps.

Unfortunately, the evolution of large eddy structures characteristic of most fire plumes is lost with such an approach, as is the prediction of local transient events. It is sometimes argued that the averaging process used to define the equations is an "ensemble average" over many replicates of the same experiment or postulated scenario. However, this is a moot point in fire research since neither experiments nor real scenarios are replicated in the sense required by that interpretation of the equations. The application of "Large Eddy Simulation" (LES) techniques to fire is aimed at extracting greater temporal and spatial fidelity from simulations of fire performed on the more finely meshed grids allowed by ever faster computers.

The phrase LES refers to the description of turbulent mixing of the gaseous fuel and combustion products with the local atmosphere surrounding the fire. This process, which determines the burning rate in most fires and controls the spread of smoke and hot gases, is extremely difficult to predict accurately. This is true not only in fire research but in almost all phenomena involving turbulent fluid motion. The basic idea behind the LES technique is that the eddies that account for most of the mixing are large enough to be calculated with reasonable accuracy from the equations of fluid dynamics. The hope (which must ultimately be justified by comparison to experiments) is that small-scale eddy motion can either be crudely accounted for or ignored.

The equations describing the transport of mass, momentum, and energy by the fire-induced flows must be simplified so that they can be efficiently solved for the fire scenarios of interest. The general equations of fluid dynamics describe a rich variety of physical processes, many of which have nothing to do with fires. Retaining this generality would lead to an enormously complex computational task that would shed very little additional insight on fire dynamics. The simplified equations, developed by Rehm and Baum [9], have been widely adopted by the larger combustion research community, where they are referred to as the "low Mach number" combustion equations. They describe the low speed motion of a gas driven by chemical heat release and buoyancy forces. Oran and Boris provide a useful discussion of the technique as applied to various reactive flow regimes in the chapter entitled "Coupled Continuity Equations for Fast and Slow Flows" in Ref. [10]. They comment that "There is generally a heavy price for being able to use a single algorithm for both fast and slow flows, a price that translates into many computer operations per time step often spent in solving multiple and complicated matrix operations."

The low Mach number equations are solved numerically by dividing the physical space where the fire is to be simulated into a large number of rectangular cells. Within each cell the gas velocity, temperature, *etc.*, are assumed to be uniform; changing only with time. The accuracy with which the fire dynamics can

be simulated depends on the number of cells that can be incorporated into the simulation. This number is ultimately limited by the computing power available. Present day, single processor desktop computers limit the number of such cells to at most a few million. This means that the ratio of largest to smallest eddy length scales that can be resolved by the computation (the "dynamic range" of the simulation) is on the order of 100. Parallel processing can be used to extend this range to some extent, but the range of length scales that need to be accounted for if all relevant fire processes are to be simulated is roughly 10^4 to 10^5 because combustion processes take place at length scales of 1 mm or less, while the length scales associated with building fires are of the order of tens of meters. The form of the numerical equations discussed below depends on which end of the spectrum one wants to capture directly, and which end is to be ignored or approximated.

Chapter 2

Model Overview

This chapter presents general information about the Fire Dynamics Simulator, following the basic framework set forth in ASTM E 1355 [1].

2.1 Basic Description of FDS

2.1.1 Type of Model

FDS is a Computational Fluid Dynamics (CFD) model of fire-driven fluid flow. The model solves numerically a form of the Navier-Stokes equations appropriate for low-speed, thermally-driven flow with an emphasis on smoke and heat transport from fires. The partial derivatives of the conservation equations of mass, momentum and energy are approximated as finite differences, and the solution is updated in time on a three-dimensional, rectilinear grid. Thermal radiation is computed using a finite volume technique on the same grid as the flow solver. Lagrangian particles are used to simulate smoke movement, sprinkler discharge, and fuel sprays.

Smokeview is a companion program to FDS that produces images and animations of the results. In recent years, its developer, Glenn Forney, has added to Smokeview the ability to visualize fire and smoke in a fairly realistic way. In a sense, Smokeview now is, via its three-dimensional renderings, an integral part of the physical model, as it allows one to assess the visibility within a fire compartment in ways that ordinary scientific visualization software cannot.

Although not part of the FDS/Smokeview suite maintained at NIST, there are several third-party and proprietary "add-ons" to FDS either available commercially or privately maintained by individual users. Most notably, there are several Graphical User Interfaces (GUIs) that can be used to create the input file containing all the necessary information needed to perform a simulation.

2.1.2 Version History

Version 1 of FDS was publicly released in February 2000, version 2 in December 2001, version 3 in November 2002, and version 4 in July 2004. The present version of FDS is 5, first released in October, 2007.

Starting with FDS 5, a formal revision management system has been implemented to track changes to the FDS source code. The open-source program development tools are provided by an Internet-based organization known as Google Code (code.google.com).

The version number for FDS has three parts. For example, FDS 5.2.12 indicates that this is FDS 5, the fifth major release. The 2 indicates a significant upgrade, but still within the framework of FDS 5. The 12 indicates the twelveth minor upgrade of 5.2, mostly bug fixes and minor user requests.

2.1.3   Model Developers

Currently, FDS is maintained by the Building and Fire Research Laboratory (BFRL) of National Institute of Standards and Technology. The developers at NIST have formed a loose collaboration of interested stakeholders, including:

- VTT Technical Research Centre of Finland, a research and testing laboratory similar to NIST

- The Society of Fire Protection Engineers (SFPE) who conduct training classes on the use of FDS

- Fire protection engineering firms that use the software

- Engineering departments at various universities with a particular emphasis on fire

BFRL awards grants on a competitive basis to external organizations who conduct research in fire science and engineering. Some of these grants have been used to assist the development of FDS. The role of the grantee in supporting day to day development varies. Not all of the developers outside of NIST are grantees.

Starting with Version 5, the FDS development team uses an Internet-based development environment called GoogleCode, a free service of the search engine company, Google. GoogleCode is a widely used service designed to assist open source software development by providing a repository for source code, revision control, program distribution, bug tracking, and various other very useful services.

Each member of the FDS development team has an account and password access to the FDS repository. In addition, anonymous access is available to all interested users, who can receive the latest versions of the source code, manuals, and other items. Anonymous users simply do not have the power to commit changes to any of these items. The power to commit changes to FDS or its manuals can be granted to anyone on a case by case basis.

The FDS manuals are typeset using LaTeX, specifically, PDF LaTeX. The LaTeXfiles are essentially text files that are under SVN (Subversion) control. The figures are either in the form of PDF or jpeg files, depending on whether they are vector or raster format. There are a variety of LaTeXpackages available, including MiKTeX. The FDS developers edit the manuals as part of the day to day upkeep of the model. Different editions of the manuals are distinguished by date.

2.1.4   Intended Uses

Throughout its development, FDS has been aimed at solving practical fire problems in fire protection engineering, while at the same time providing a tool to study fundamental fire dynamics and combustion. FDS can be used to model the following phenomena:

- Low speed transport of heat and combustion products from fire
- Radiative and convective heat transfer between the gas and solid surfaces
- Pyrolysis
- Flame spread and fire growth
- Sprinkler, heat detector, and smoke detector activation
- Sprinkler sprays and suppression by water

Although FDS was designed specifically for fire simulations, it can be used for other low-speed fluid flow simulations that do not necessarily include fire or thermal effects. To date, about half of the applications of the model have been for design of smoke control systems and sprinkler/detector activation studies. The other half consist of residential and industrial fire reconstructions.

2.1.5 Input Parameters

All of the input parameters required by FDS to describe a particular scenario are conveyed via a single text file created by the user. The file contains information about the numerical grid, ambient environment, building geometry, material properties, combustion kinetics, and desired output quantities. The numerical grid consists of one or more rectilinear meshes with (usually) uniform cells. All geometric features of the scenario must conform to this numerical grid. Objects smaller than a single grid cell are either approximated as a single cell, or rejected. The building geometry is input as a series of rectangular blocks. Boundary conditions are applied to solid surfaces as rectangular patches. Materials are defined by their thermal conductivity, specific heat, density, thickness, and burning behavior. There are various ways that this information is conveyed, depending on the desired level of detail.

Any simulation of a real fire scenario involves specifying material properties for the walls, floor, ceiling, and furnishings. FDS treats all of these objects as multi-layered solids, thus the physical parameters for many real objects can only be viewed as approximations to the actual properties. Describing these materials in the input file is the single most challenging task for the user. Thermal properties such as conductivity, specific heat, density, and thickness can be found in various handbooks, or in manufacturers literature, or from bench-scale measurements. The burning behavior of materials at different heat fluxes is more difficult to describe, and the properties more difficult to obtain. Even though entire books are devoted to the subject [11], it is still difficult to find information on a particular item.

A significant part of the FDS input file directs the code to output various quantities in various ways. Much like in an actual experiment, the user must decide before the calculation begins what information to save. There is no way to recover information after the calculation is over if it was not requested at the start.

A complete description of the input parameters required by FDS can be found in the FDS User's Guide [3].

2.1.6 Output Quantities

FDS computes the temperature, density, pressure, velocity and chemical composition within each numerical grid cell at each discrete time step. There are typically hundreds of thousands to millions of grid cells and thousands to hundreds of thousands of time steps. In addition, FDS computes at solid surfaces the temperature, heat flux, mass loss rate, and various other quantities. The user must carefully select what data to save, much like one would do in designing an actual experiment. Even though only a small fraction of the computed information can be saved, the output typically consists of fairly large data files. Typical output quantities for the gas phase include:

- Gas temperature

- Gas velocity

- Gas species concentration (water vapor, CO_2, CO, N_2)

- Smoke concentration and visibility estimates

- Pressure

- Heat release rate per unit volume

- Mixture fraction (or air/fuel ratio)

- Gas density

- Water droplet mass per unit volume

On solid surfaces, FDS predicts additional quantities associated with the energy balance between gas and solid phase, including

- Surface and interior temperature

- Heat flux, both radiative and convective

- Burning rate

- Water droplet mass per unit area

Global quantities recorded by the program include:

- Total Heat Release Rate (HRR)

- Sprinkler and detector activation times

- Mass and energy fluxes through openings or solids

Time histories of various quantities at a single point in space or global quantities like the fire's heat release rate (HRR) are saved in simple, comma-delimited text files that can be plotted using a spreadsheet program. However, most field or surface data are visualized with a program called Smokeview, a tool specifically designed to analyze data generated by FDS. FDS and Smokeview are used in concert to model and visualize fire phenomena. Smokeview performs this visualization by presenting animated tracer particle flow, animated contour slices of computed gas variables and animated surface data. Smokeview also presents contours and vector plots of static data anywhere within a scene at a fixed time.

A complete list of FDS output quantities and formats is given in Ref. [3]. Details on the use of Smokeview are found in Ref. [12].

2.1.7 Governing Equations, Assumptions and Numerics

Following is a brief description of the major components of FDS. Detailed information regarding the assumptions and governing equations associated with the model is provided in Section 3.1.

Hydrodynamic Model FDS solves numerically a form of the Navier-Stokes equations appropriate for low-speed, thermally-driven flow with an emphasis on smoke and heat transport from fires. The core algorithm is an explicit predictor-corrector scheme that is second order accurate in space and time. Turbulence is treated by means of the Smagorinsky form of Large Eddy Simulation (LES). It is possible to perform a Direct Numerical Simulation (DNS) if the underlying numerical grid is fine enough. LES is the default mode of operation.

Combustion Model For most applications, FDS uses a combustion model based on the mixture fraction concept. The mixture fraction is a conserved scalar quantity that is defined as the fraction of gas at a given point in the flow field that originates as fuel. Unlike versions of FDS prior to 5, the reaction of fuel and oxygen is not necessarily instantaneous and complete, and there are several optional schemes that are designed to predict the extent of combustion in under-ventilated spaces. The mass fractions of all of the major reactants and products can be derived from the mixture fraction by means of "state relations," expressions arrived at by a combination of simplified analysis and measurement.

Radiation Transport Radiative heat transfer is included in the model via the solution of the radiation transport equation for a gray gas. In a limited number of cases, a wide band model can be used in place of the gray gas model to provide a better spectral accuracy. The radiation equation is solved using a technique similar to a finite volume method for convective transport, thus the name given to it is the Finite Volume Method (FVM). Using approximately 100 discrete angles, the finite volume solver requires about 20 % of the total CPU time of a calculation, a modest cost given the complexity of radiation heat transfer. Water droplets can absorb and scatter thermal radiation. This is important in

8

cases involving mist sprinklers, but also plays a role in all sprinkler cases. The absorption and scattering coefficients are based on Mie theory. The scattering from the gaseous species and soot is not included in the model.

Geometry FDS approximates the governing equations on one or more rectilinear grids. The user prescribes rectangular obstructions that are forced to conform with the underlying grid.

Boundary Conditions All solid surfaces are assigned thermal boundary conditions, plus information about the burning behavior of the material. Heat and mass transfer to and from solid surfaces is usually handled with empirical correlations, although it is possible to compute directly the heat and mass transfer when performing a Direct Numerical Simulation (DNS).

Sprinklers and Detectors The activation of sprinklers and heat and smoke detectors is modeled using fairly simple correlations of thermal inertia for sprinklers and heat detectors, and transport lag for smoke detectors. Sprinkler sprays are modeled by Lagrangian particles that represent a sampling of the water droplets ejected from the sprinkler.

2.1.8 Limitations

Although FDS can address most fire scenarios, there are limitations in all of its various algorithms. Some of the more prominent limitations of the model are listed here. More specific limitations are discussed as part of the description of the governing equations in Section 3.1.

Low Speed Flow Assumption The use of FDS is limited to low-speed[1] flow with an emphasis on smoke and heat transport from fires. This assumption rules out using the model for any scenario involving flow speeds approaching the speed of sound, such as explosions, choke flow at nozzles, and detonations.

Rectilinear Geometry The efficiency of FDS is due to the simplicity of its rectilinear numerical grid and the use of a fast, direct solver for the pressure field. This can be a limitation in some situations where certain geometric features do not conform to the rectangular grid, although most building components do. There are techniques in FDS to lessen the effect of "sawtooth" obstructions used to represent non-rectangular objects, but these cannot be expected to produce good results if, for example, the intent of the calculation is to study boundary layer effects. For most practical large-scale simulations, the increased grid resolution afforded by the fast pressure solver offsets the approximation of a curved boundary by small rectangular grid cells.

Fire Growth and Spread Because the model was originally designed to analyze industrial-scale fires, it can be used reliably when the heat release rate (HRR) of the fire is specified and the transport of heat and exhaust products is the principal aim of the simulation. In these cases, the model predicts flow velocities and temperatures to an accuracy within 10 % to 20 % of experimental measurements, depending on the resolution of the numerical grid [2]. However, for fire scenarios where the heat release rate is *predicted* rather than *specified*, the uncertainty of the model is higher. There are several reasons for this: (1) properties of real materials and real fuels are often unknown or difficult to obtain, (2) the physical processes of combustion, radiation and solid phase heat transfer are more complicated than their mathematical representations in FDS, (3) the results of calculations are sensitive to both

---

[1]Mach numbers less than about 0.3

[2]It is extremely rare to find measurements of local velocities and/or temperatures from fire experiments that have reported error estimates that are less than 10 %. Thus, the most accurate calculations using FDS do not introduce significantly greater errors in these quantities than the vast majority of fire experiments.

the numerical and physical parameters. Current research is aimed at improving this situation, but it is safe to say that modeling fire growth and spread will always require a higher level of user skill and judgment than that required for modeling the transport of smoke and heat from specified fires.

Combustion For most applications, FDS uses a mixture fraction-based combustion model. The mixture fraction is a conserved scalar quantity that is defined as the fraction of gas at a given point in the flow field that originated as fuel. In its simplest form, the model assumes that combustion is mixing-controlled, and that the reaction of fuel and oxygen is infinitely fast, regardless of the temperature. For large-scale, well-ventilated fires, this is a good assumption. However, if a fire is in an under-ventilated compartment, or if a suppression agent like water mist or CO_2 is introduced, fuel and oxygen are allowed to mix and not burn, according to a few empirically-based criteria. The physical mechanisms underlying these phenomena are complex, and are tied closely to the flame temperature and local strain rate, neither of which are readily-available in a large scale fire simulation. Subgrid-scale modeling of gas phase suppression and extinction is still an area of active research in the combustion community. Until reliable models can be developed for building-scale fire simulations, simple empirical rules can be used that prevent burning from taking place when the atmosphere immediately surrounding the fire cannot sustain the combustion. Details are found in Section 3.2.

Radiation Radiative heat transfer is included in the model via the solution of the radiation transport equation (RTE) for a gray gas, and in some limited cases using a wide band model. The RTE is solved using a technique similar to finite volume methods for convective transport, thus the name given to it is the Finite Volume Method (FVM). There are several limitations of the model. First, the absorption coefficient for the smoke-laden gas is a complex function of its composition and temperature. Because of the simplified combustion model, the chemical composition of the smokey gases, especially the soot content, can effect both the absorption and emission of thermal radiation. Second, the radiation transport is discretized via approximately 100 solid angles, although the user may choose to use more angles. For targets far away from a localized source of radiation, like a growing fire, the discretization can lead to a non-uniform distribution of the radiant energy. This error is called "ray effect" and can be seen in the visualization of surface temperatures, where "hot spots" show the effect of the finite number of solid angles. The problem can be lessened by the inclusion of more solid angles, but at a price of longer computing times. In most cases, the radiative flux to far-field targets is not as important as those in the near-field, where coverage by the default number of angles is much better.

2.2 Peer Review Process

FDS is reviewed both internally and externally. All documents issued by the National Institute of Standards and Technology are formally reviewed internally by members of the staff. The theoretical basis of FDS is laid out in the present document, and is subject to internal review by staff members who are not active participants in the development of the model, but who are members of the Fire Research Division and are considered experts in the fields of fire and combustion. Externally, papers detailing various parts of FDS are regularly published in peer-reviewed journals and conference proceedings. In addition, FDS is used world-wide by fire protection engineering firms who review the technical details of the model related to their particular application. Some of these firms also publish in the open literature reports documenting internal efforts to validate the model for a particular use. Many of these studies are referenced in Volume 3 of the FDS Technical Reference Guide [2].

2.2.1 Survey of the Relevant Fire and Combustion Literature

FDS has two separate manuals – the FDS Technical Reference Guide [2] and the FDS User's Guide [3]. The Technical Reference Guide is broken into three volumes: (1) Mathematical Model, (2) Verification, and (3) Experimental Validation. Smokeview has its own User's Guide [12]. The FDS and Smokeview User Guides only describe the mechanics of using the computer programs. The Technical Reference Guides provides the theory, algorithm details, and verification and validation work.

There are numerous sources that describe various parts of the model. The basic set of equations solved in FDS was formulated by Rehm and Baum in the *Journal of Research of the National Bureau of Standards* [9]. The basic hydrodynamic algorithm evolved at NIST through the 1980s and 1990s, incorporating fairly well-known numerical schemes that are documented in books by Anderson, Tannehill and Pletcher [13], Peyret and Taylor [14], and Ferziger and Perić [15]. This last book provides a good description of the large eddy simulation technique and provides references to many current publications on the subject. Numerical techniques appropriate for combustion systems are described by Oran and Boris [10]. The mixture fraction combustion model is described in a review article by Bilger [16]. Basic heat transfer theory is provided by Holman [17] and Incropera [18]. Thermal radiation is described in Siegel and Howell [19].

Much of the current knowledge of fire science and engineering is found in the *SFPE Handbook of Fire Protection Engineering* [20]. Popular textbooks in fire protection engineering include those by Drysdale [21] and Quintiere [22]. On-going research in fire and combustion is documented in several periodicals and conference proceedings. The International Association of Fire Safety Science (IAFSS) organizes a conference every two years, the proceedings of which are frequently referenced by fire researchers. Interscience Communications, a London-based publisher of several fire-related journals, hosts a conference known as Interflam roughly every three years in the United Kingdom. The Combustion Institute hosts an international symposium on combustion every two years, and in addition to the proceedings of this symposium, the organization publishes its own journal, *Combustion and Flame*. The papers appearing in the IAFSS conference proceedings, the Combustion Symposium proceedings, and *Combustion and Flame* are all peer-reviewed, while those appearing in the Interflam proceedings are selected based on the submission of a short abstract. Both the Society for Fire Protection Engineers (SFPE) and the National Fire Protection Association (NFPA) publish peer-reviewed technical journals entitled the *Journal of Fire Protection Engineering* and *Fire Technology*. Other often-cited, peer-reviewed technical journals include the *Fire Safety Journal*, *Fire and Materials*, *Combustion Science and Technology*, *Combustion Theory and Modeling* and the *Journal of Heat Transfer*.

Research at NIST is documented in various ways beyond contributions made by staff to external journals and conferences. NIST publishes several forms of internal reports, special publications, and its own journal called the *Journal of Research of NIST*. An internal report, referred to as a NISTIR (NIST Inter-agency

Report), is a convenient means to disseminate information, especially when the quantity of data exceeds what could normally be accepted by a journal. Often parts of a NISTIR are published externally, with the NISTIR itself serving as the complete record of the work performed. Previous versions of the FDS Technical Reference Guide and User's Guide were published as NISTIRs. The current FDS and Smokeview manuals are being published as NIST Special Publications, distinguished from NISTIRs by the fact that they are permanently archived. Work performed by an outside person or organization working under a NIST grant or contract is published in the form of a NIST Grant/Contract Report (GCR). All work performed by the staff of the Building and Fire Research Laboratory at NIST beyond 1993 is permanently stored in electronic form and made freely available via the Internet and yearly-released compact disks (CDs) or other electronic media.

2.2.2 Review of the Theoretical Basis of the Model

The technical approach and assumptions of the model have been presented in the peer-reviewed scientific literature and at technical conferences cited in the previous section. The major assumptions of the model, for example the large eddy simulation technique and the mixture fraction combustion model, have undergone a roughly 40 year development and are now documented in popular introductory text books. More specific sub-models, like the sprinkler spray routine or the various pyrolysis models, have yet to be developed to this extent. As a consequence, all documents produced by NIST staff are required to go through an internal editorial review and approval process. This process is designed to ensure compliance with the technical requirements, policy, and editorial quality required by NIST. The technical review includes a critical evaluation of the technical content and methodology, statistical treatment of data, uncertainty analysis, use of appropriate reference data and units, and bibliographic references. The FDS and Smokeview manuals are first reviewed by a member of the Fire Research Division, then by the immediate supervisor of the author of the document, then by the chief of the Fire Research Division, and finally by a reader from outside the division. Both the immediate supervisor and the division chief are technical experts in the field. Once the document has been reviewed, it is then brought before the Editorial Review Board (ERB), a body of representatives from all the NIST laboratories. At least one reader is designated by the Board for each document that it accepts for review. This last reader is selected based on technical competence and impartiality. The reader is usually from outside the division producing the document and is responsible for checking that the document conforms with NIST policy on units, uncertainty and scope. He/she does not need to be a technical expert in fire or combustion.

Recently, the US Nuclear Regulatory Commission (US NRC) published a seven-volume report on its own verification and validation study of five different fire models used for nuclear power plant applications [23]. Two of the models are essentially a set of empirically-based correlations in the form of engineering "spread sheets." Two of the models are classic two-zone fire models, one of which is the NIST developed CFAST. FDS is the sole CFD model in the study. More on the study and its results can be found in Volume 3 of the FDS Technical Reference Guide [2].

Besides formal internal and peer review, FDS is subjected to continuous scrutiny because it is available free of charge to the general public and is used internationally by those involved in fire safety design and post-fire reconstruction. The quality of the FDS and Smokeview User Guides is checked implicitly by the fact that the majority of model users have not taken a formal training course in the actual use of the model, but are able to read the supporting documents, perform a few sample simulations, and then systematically build up a level of expertise appropriate for their applications. The developers receive daily feedback from users on the clarity of the documentation and add clarifications when needed. Before new versions of the model are released, there is a several month "beta test" period in which users test the new version using the updated documentation. This process is similar, although less formal, to that which most computer software programs undergo. Also, the source code for FDS is released publicly, and has been used at various

universities world-wide, both in the classroom as a teaching tool as well as for research. As a result, flaws in the theoretical development and the computer program itself have been identified and corrected. As FDS continues to evolve, the user base will continue to serve as a means to evaluate the model. We consider this process as important to the development of FDS as the formal internal and external peer-review processes.

2.3 Development Process

Changes are made to the FDS source code daily, and tracked via revision control software. However, these daily changes do not constitute a change to the version number. After the developers determine that enough changes have been made to the source, they release a new minor upgrade, 5.2.12 to 5.2.13, for example. This happens every few weeks. A change from 5.2 to 5.3 might happen only a few times a year, when significant improvements have been made to the model physics.

There is no formal process by which FDS is updated. Each developer works on various routines, and makes changes as warranted. Minor bugs are fixed without any communication (the developers are in different locations), but more significant changes are discussed via email or telephone calls. A suite of simple verification calculations (included in this document) are routinely run to ensure that the daily bug fixes have not altered any of the important algorithms. A suite of validation calculations (also included here) are run with each significant upgrade. Significant changes to FDS are made based on the following criteria, in no particular order:

Better Physics: The goal of any model is to be *predictive*, but it also must be reliable. FDS is a blend of empirical and deterministic sub-models, chosen based on their robustness, consistency, and reliability. Any new sub-model must demonstrate that it is of comparable or superior accuracy to its empirical counterpart.

Modest CPU Increase: If a proposed algorithm doubles the calculation time but yields only a marginal improvement in accuracy, it is likely to be rejected. Also, the various routines in FDS are expected to consume CPU time in proportion to their overall importance. For example, the radiation transport algorithm consumes about 25 % of the CPU time, consistent with the fact that about one-fourth to one-third of the fire's energy is emitted as thermal radiation.

Simpler Algorithm: If a new algorithm does what the old one did using less lines of code, it is almost always accepted, so long as it does not decrease functionality.

Increased or Comparable Accuracy: The validation experiments that are part of this guide serve as the metric for new routines. It is not enough for a new algorithm to perform well in a few cases. It must show clear improvement across the suite of experiments. If the accuracy is only comparable to the previous version, then some other criteria must be satisfied.

Acceptance by the Fire Protection Community: Especially in regard to fire-specific devices, like sprinklers and smoke detectors, the algorithms in FDS often are based on their acceptance among the practicing engineers.

Chapter 3

Governing Equations

This chapter presents the governing equations of FDS. The numerical algorithm is presented in the next chapter. The governing equations are presented as a set of partial differential equations, with appropriate simplifications and approximations noted. The numerical method essentially consists of a finite difference approximation of the governing equations and a procedure for updating these equations in time.

3.1 Hydrodynamic Model

An approximate form of the Navier-Stokes equations appropriate for low Mach number applications is used in the model. The approximation involves the filtering out of acoustic waves while allowing for large variations in temperature and density [9]. This gives the equations an elliptic character, consistent with low speed, thermal convective processes. The computation can either be treated as a Direct Numerical Simulation (DNS), in which the dissipative terms are computed directly, or as a Large Eddy Simulation (LES), in which the large-scale eddies are computed directly and the subgrid-scale dissipative processes are modeled. The numerical algorithm is designed so that LES becomes DNS as the grid is refined. Most applications of FDS are LES. For example, in simulating the flow of smoke through a large, multi-room enclosure, it is not possible to resolve the combustion and transport processes directly. However, for small-scale combustion experiments, it is possible to compute the transport and combustion processes directly.

3.1.1 The Fundamental Conservation Equations

The conservation equations for mass, momentum and energy for a Newtonian fluid are presented here. These are the same equations that can be found in almost any textbook on fluid dynamcs or CFD. A particularly useful reference for a description of the equations, the notation used, and the various approximations employed is Anderson *et al.* [13].

Conservation of Mass

$$\frac{\partial \rho}{\partial t} + \nabla \cdot \rho \mathbf{u} = \dot{m}_b''' \tag{3.1}$$

Conservation of Momentum (Newton's Second Law)

$$\frac{\partial}{\partial t}(\rho \mathbf{u}) + \nabla \cdot \rho \mathbf{u}\mathbf{u} + \nabla p = \rho \mathbf{g} + \mathbf{f}_b + \nabla \cdot \tau_{ij} \tag{3.2}$$

Transport of Sensible Enthalpy

$$\frac{\partial}{\partial t}(\rho h_s) + \nabla \cdot \rho h_s \mathbf{u} = \frac{\mathrm{D}p}{\mathrm{D}t} + \dot{q}''' - \dot{q}_b''' - \nabla \cdot \dot{\mathbf{q}}'' + \varepsilon \tag{3.3}$$

Equation of State for a Perfect Gas

$$p = \frac{\rho \mathcal{R} T}{\overline{W}} \tag{3.4}$$

Note that this is a set of partial differential equations consisting of six equations for six unknowns, all functions of three spatial dimensions and time: the density ρ, the three components of velocity $\mathbf{u} = [u, v, w]^T$, the temperature T, and the pressure p. The sensible enthalpy $h_s = \sum_\alpha Y_\alpha h_{s,\alpha}$ is a function of the temperature: $h_{s,\alpha}(T) = \int_{T_0}^T c_{p,\alpha}(T') \, dT'$.

The notation adopted above is intended to render the equations in as simple and compact a form as possible. However, when all of the terms are expanded, the equations appear unwieldy. For the model developers, this is unavoidable. For the model user, it is sufficient to understand the basic conservation laws to appreciate what the model does, and does not, represent. Following is a brief description of the terms. Note that boldfaced quantities represent vectors. Boldfaced quantities with the subscripts ij represent tensors, which can be best understood as 3×3 matrices.

The mass conservation equation is often written in terms of the mass fractions of the individual gaseous species, Y_α:

$$\frac{\partial}{\partial t}(\rho Y_\alpha) + \nabla \cdot \rho Y_\alpha \mathbf{u} = \nabla \cdot \rho D_\alpha \nabla Y_\alpha + \dot{m}_\alpha''' + \dot{m}_{b,\alpha}''' \tag{3.5}$$

Here $\dot{m}_{b,\alpha}'''$ is the production of species α by evaporating droplets or particles. Summing these equations over all species yields the original mass conservation equation because $\sum Y_\alpha = 1$ and $\sum \dot{m}_\alpha''' = 0$ and $\sum \dot{m}_{b,\alpha}''' = \dot{m}_b'''$, by definition, and because it is assumed that $\sum \rho D_\alpha \nabla Y_\alpha = 0$. This last assertion is not true, in general. However, transport equations are solved for total mass and all but one of the species, implying that the diffusion coefficient of the implicit species is chosen so that the sum of all the diffusive fluxes is zero.

In the momentum equation, the term $\mathbf{uu}$ is a diadic tensor. In matrix notation, with $\mathbf{u} = [u, v, w]^T$, the diadic is given by the tensor product of the vectors $\mathbf{u}$ and $\mathbf{u}^T$. The term $\nabla \cdot \rho \mathbf{uu}$ is thus a vector formed by applying the vector operator $\nabla = (\frac{\partial}{\partial x}, \frac{\partial}{\partial y}, \frac{\partial}{\partial z})$ to the tensor. The force term $\mathbf{f}_b$ in the momentum equation represents external forces such as the drag exerted by liquid droplets. The stress tensor τ_{ij} is defined:

$$\tau_{ij} = \mu \left(2 \, \mathbf{S}_{ij} - \frac{2}{3} \delta_{ij} (\nabla \cdot \mathbf{u}) \right) \quad ; \quad \delta_{ij} = \left\{ \begin{array}{ll} 1 & i = j \\ 0 & i \neq j \end{array} \right. \quad ; \quad \mathbf{S}_{ij} = \frac{1}{2} \left(\frac{\partial u_i}{\partial x_j} + \frac{\partial u_j}{\partial x_i} \right) \quad i, j = 1, 2, 3 \tag{3.6}$$

The term $\mathbf{S}_{ij}$ is the symmetric rate-of-strain tensor, written using conventional tensor notation. The symbol μ is the dynamic viscosity of the fluid.

In the sensible enthalpy equation, note the use of the material derivative, $D(\,)/Dt = \partial(\,)/\partial t + \mathbf{u} \cdot \nabla(\,)$. The term $\dot{q}'''$ is the heat release rate per unit volume from a chemical reaction. The term $\dot{q}_b'''$ is the energy transferred to the evaporating droplets. The term $\dot{\mathbf{q}}''$ represents the conductive and radiative heat fluxes:

$$\dot{\mathbf{q}}'' = -k \nabla T - \sum_\alpha h_{s,\alpha} \rho D_\alpha \nabla Y_\alpha + \dot{\mathbf{q}}_r'' \tag{3.7}$$

where k is the thermal conductivity.

The term ε in the sensible enthalpy equation is known as the *dissipation rate*. It is the rate at which

kinetic energy is transferred to thermal energy due to the viscosity of the fluid:

$$\varepsilon \equiv \tau_{ij} \cdot \nabla \mathbf{u} \quad = \quad \mu \left(2\,\mathbf{S}_{ij} \cdot \mathbf{S}_{ij} - \frac{2}{3}(\nabla \cdot \mathbf{u})^2 \right)$$

$$= \mu \left[2\left(\frac{\partial u}{\partial x}\right)^2 + 2\left(\frac{\partial v}{\partial y}\right)^2 + 2\left(\frac{\partial w}{\partial z}\right)^2 + \right.$$

$$\left. \left(\frac{\partial v}{\partial x}+\frac{\partial u}{\partial y}\right)^2 + \left(\frac{\partial w}{\partial y}+\frac{\partial v}{\partial z}\right)^2 + \left(\frac{\partial u}{\partial z}+\frac{\partial w}{\partial x}\right)^2 - \frac{2}{3}\left(\frac{\partial u}{\partial x}+\frac{\partial v}{\partial y}+\frac{\partial w}{\partial z}\right)^2 \right] \tag{3.8}$$

This term is usually neglected because it is very small relative to the heat release rate of the fire. However, it is included here because it plays a role in the discussion of large eddy simulation.

The equations presented here form the basis for a wide variety of engineering applications, but not without the further application of simplifying assumptions unique to each field. The only assumptions made thus far are that the fluid is a perfect gas, that the stress is linearly dependent on the strain, that heat is conducted according to Fourier's Law, and that gas species diffuse according to Fick's Law. In the sections to follow, additional assumptions will be imposed on the governing equations to apply them to fire and other low speed thermal processes. The most important of these assumptions involves the treatment of the diffusion and source terms that differentiates one type of CFD model from another.

3.1.2 The Low Mach Number Assumption and the Equation of State

A distinguishing feature of a CFD model is the regime of flow speeds (relative to the speed of sound) for which it is designed. High speed flow codes involve compressibility effects and shock waves. Low speed solvers, however, explicitly eliminate compressibity effects that give rise to acoustic (sound) waves. As written in Section 3.1.1, the Navier-Stokes equations describe the propagation of information at speeds comparable to that of the fluid flow (for fire, 10-20 m/s), but also at speeds comparable to that of sound waves (for still air, 300 m/s). Solving a discretized form of these equations would require extremely small time steps in order to account for information traveling at the speed of sound, making practical simulations difficult.

Following the work of Rehm and Baum [9], an approximation to the equation of state (3.4) is made by decomposing the pressure into a "background" component and a perturbation. The original version of FDS assumed that the background component of the pressure applied to the entire computational domain, most often a single compartment. Starting in FDS version 5, it is now assumed that the background component of pressure can differ from compartment to compartment. If a volume within the computational domain is isolated from other volumes, except via leak paths or ventilation ducts, it is referred to as a "pressure zone" and assigned its own background pressure. The pressure within the mth zone, for example, is a linear combination of its background component and the flow-induced perturbation:

$$p(\mathbf{x},t) = \overline{p}_m(z,t) + \tilde{p}(\mathbf{x},t) \tag{3.9}$$

Note that the background pressure is a function of z, the vertical spatial coordinate, and time. For most compartment fire applications, $\overline{p}_m$ changes very little with height or time. However, for situations where the pressure increases due to a fire in a tightly sealed enclosure, or when the height of the domain is significant, $\overline{p}_m$ takes these effects into account [24]. The ambient pressure field is denoted $\overline{p}_0(z)$. Note that the subscript 0 denotes the exterior of the computational domain, not time 0. This is the assumed atmospheric pressure stratification that serves as both the initial and boundary condition for the governing equations.

The purpose of decomposing the pressure is that for low-Mach number flows, it can be assumed that the temperature and density are inversely proportional, and thus the equation of state (in the mth pressure zone)

can be approximated

$$\overline{p}_m = \rho T \mathcal{R} \sum_\alpha \frac{Y_\alpha}{W_\alpha} = \frac{\rho T \mathcal{R}}{\overline{W}} \tag{3.10}$$

The pressure, p, in the state and energy equations is replaced by the background pressure $\overline{p}_m$ to filter out sound waves that travel at speeds that are much faster than typical flow speeds expected in fire applications. The low Mach number assumption serves two purposes. First, the filtering of acoustic waves means that the time step in the numerical algorithm is bound only by the flow speed as opposed to the speed of sound, and second, the modified state equation leads to a reduction in the number of dependent variables in the system of equations by one. The energy equation (3.3) is never explicitly solved, but its source terms are included in the expression for the flow divergence, to be derived presently.

The stratification of the atmosphere is derived from the relation

$$\frac{d\overline{p}_0}{dz} = -\rho_0(z) g \tag{3.11}$$

where ρ_0 is the background density and $g = 9.8$ m/s^2. Using Eq. (3.10), the background pressure can be written as a function of the background temperature, $T_0(z)$,

$$\overline{p}_0(z) = p_\infty \exp\left(-\int_{z_\infty}^z \frac{\overline{W} g}{\mathcal{R} T_0(z')} dz'\right) \tag{3.12}$$

where the subscript infinity generally refers to the ground. A linear temperature stratification of the atmosphere may be specified by the user such that $T_0(z) = T_\infty + \Gamma z$ where T_∞ is the temperature at the ground and Γ is the lapse rate (e.g., $\Gamma = -0.0098$ K/m is the *adiabatic lapse rate*). In this case $\overline{p}_0$ and ρ_0 are derived from Eqs. (3.12) and (3.10), respectively. It can then be shown that for $\Gamma \neq 0$ the pressure stratification becomes

$$\overline{p}_0(z) = p_\infty \left(\frac{T_0(z)}{T_\infty}\right)^{\overline{W} g / \mathcal{R} \Gamma} \tag{3.13}$$

3.1.3 Combination of the Mass and Energy Equations via the Divergence

Because of the low Mach number assumption, the divergence of the flow, $\nabla \cdot \mathbf{u}$, plays a very important role in the overall solution scheme. The divergence is obtained by taking the material (substantial) derivative of the modified Equation of State (3.10), and then substituting terms from the mass and energy conservation equations. As shown in Appendix B, for the mth zone with background pressure $\overline{p}_m$, the divergence may be written as

$$\nabla \cdot \mathbf{u} = \mathcal{D} - \mathcal{P} \frac{\partial \overline{p}_m}{\partial t} \tag{3.14}$$

where

$$\mathcal{P} = \frac{1}{\overline{p}_m} \left(1 - \frac{\mathcal{R}}{\overline{W} c_p}\right) \tag{3.15}$$

and

$$\mathcal{D} = \frac{\dot{m}_b''' \overline{W}}{\rho \overline{W}_b} + \frac{\overline{W}}{\rho} \sum_\alpha \nabla \cdot (\rho D_\alpha \nabla [Y_\alpha / W_\alpha]) + \frac{1}{\rho} \sum_\alpha \left(\frac{\overline{W}}{W_\alpha} - \frac{h_{s,\alpha}}{c_p T}\right) \dot{m}_\alpha''' + \mathcal{P} w \rho g$$
$$+ \frac{\mathcal{R}}{\overline{W} c_p \overline{p}_m} \left[\dot{q}''' - \dot{q}_b''' - \nabla \cdot \dot{\mathbf{q}}'' - \sum_\alpha h_{s,\alpha} \nabla \cdot \rho D_\alpha \nabla Y_\alpha + \dot{m}_b''' \sum_\alpha Y_{b,\alpha} c_{p,\alpha} (T_b - T)\right] \tag{3.16}$$

Contributions to the divergence of the flow include the heat release rate of the fire, $\dot{q}'''$, heat losses to evaporating droplets, $\dot{q}_b'''$, the net heat flux from thermal conduction and radiation, $\nabla \cdot \dot{\mathbf{q}}''$, updrafts of air over

18

considerable heights of the atmosphere, the net mass flux from gas species diffusion and production, and global pressure changes. The change in the background pressure with time, $\partial \overline{p}_m / \partial t$, is non-zero only if it assumed that the compartment is tightly sealed, in which case the background pressure, $\overline{p}_m$, can no longer be assumed constant due to the increase (or decrease) in mass and thermal energy within the enclosure. The time derivative of the background pressure of the mth pressure zone, Ω_m, is found by integrating Eq. (3.14) over the zone volume:

$$\frac{\partial \overline{p}_m}{\partial t} = \left(\int_{\Omega_m} \mathcal{D} \, dV - \int_{\partial \Omega_m} \mathbf{u} \cdot d\mathbf{S} \right) \Big/ \int_{\Omega_m} \mathcal{P} \, dV \tag{3.17}$$

Equation (3.17) is essentially a consistency condition, ensuring that blowing air or starting a fire within a sealed compartment leads to an appropriate decrease in the divergence within the volume.

3.1.4 The Momentum Equation

The momentum equation is simplified to make it easier to solve numerically. First, we start with the non-conservative form of the momentum equation introduced above

$$\rho \left(\frac{\partial \mathbf{u}}{\partial t} + (\mathbf{u} \cdot \nabla) \mathbf{u} \right) + \nabla p = \rho \mathbf{g} + \mathbf{f}_b + \nabla \cdot \tau_{ij} \tag{3.18}$$

Next, we make the following substitutions:

1. Subtract the hydrostatic pressure gradient of the nth pressure zone, $\rho_n(z,t)\mathbf{g}$, from both sides. Note that $\nabla p = \rho_n \mathbf{g} + \nabla \tilde{p}$.

2. Apply the vector identity: $(\mathbf{u} \cdot \nabla) \mathbf{u} = \nabla |\mathbf{u}|^2 / 2 - \mathbf{u} \times \omega$

3. Divide all terms by the density, ρ

4. Decompose the pressure term, noting that ρ_∞ is the constant density at the ground:

$$\frac{\nabla \tilde{p}}{\rho} = \frac{\nabla \tilde{p}}{\rho_\infty} + \left(\frac{1}{\rho} - \frac{1}{\rho_\infty} \right) \nabla \tilde{p}$$

5. Define $\mathcal{H} \equiv |\mathbf{u}|^2 / 2 + \tilde{p} / \rho_\infty$

Now the momentum equation can be written

$$\frac{\partial \mathbf{u}}{\partial t} - \mathbf{u} \times \omega + \nabla \mathcal{H} + \left(\frac{1}{\rho} - \frac{1}{\rho_\infty} \right) \nabla \tilde{p} = \frac{1}{\rho} \left[(\rho - \rho_n) \mathbf{g} + \mathbf{f}_b + \nabla \cdot \tau_{ij} \right] \tag{3.19}$$

The numerical solution of the pressure equation obtained by taking the divergence of Eq. (3.19) is greatly simplified by either neglecting the last term on the left hand side, or in cases where it cannot be neglected, treating it with some care. The decision to either neglect the extra pressure term or to approximate it depends on its relative contribution to the creation of vorticity. An evolution equation for the circulation, $\Gamma = \oint \mathbf{u} \cdot d\mathbf{x}$, reveals the sources of vorticity in the absence of any external forces, $\mathbf{f}_b$:

$$\frac{d\Gamma}{dt} = \oint \left(\frac{1}{\rho_\infty} - \frac{1}{\rho} \right) \nabla \tilde{p} \cdot d\mathbf{x} + \oint \frac{\rho - \rho_n}{\rho} \mathbf{g} \cdot d\mathbf{x} + \oint \frac{\nabla \cdot \tau_{ij}}{\rho} \cdot d\mathbf{x} \tag{3.20}$$

The first term on the right hand side represents the baroclinic torque. The second term is buoyancy-induced vorticity. The third term represents the vorticity generated by molecular and subgrid-scale stresses, as in boundary and shear layers. In most practical large scale fire simulations, the fire itself occupies a small part

19

of the computational domain. Hence, the fire is often not well resolved by the numerical grid, in which case the vorticity generated in regions where there are large deviations in density is not captured directly. The mixing of air and combustion products occurs in the plume above the fire where buoyancy is the dominant source of vorticity. In these calculations, the baroclinic torque can be neglected to simplify the numerical solution. In simulations where detailed flame dynamics are resolvable, the pressure term responsible for the baroclinic torque cannot be neglected, but for reasons to be made clear below, must be treated differently than the other pressure term. In neither of these cases is the Boussinesq approximation invoked – the fluid is still considered thermally-expandable; the divergence is non-zero; and the mass and energy equations are not modified.

Velocity Boundary Conditions

When the momentum equation is integrated over a cell adjacent to the wall in an LES it turns out that the most difficult term to handle is the viscous stress at the wall, e.g. $\bar{\tau}_{xz}|_{z=0}$, because the wall-normal gradient of the streamwise velocity component cannot be resolved. Note that the sgs stress at the wall is identically zero. We have, therefore, an entirely different situation than exists in the bulk flow at high Reynolds number where the viscous terms are negligible and the sgs stress is of critical importance. The fidelity of the sgs model still influences the wall stress, however, since other components of the sgs tensor affect the value of the near-wall velocity and hence the resulting viscous stress determined by the wall model. The model used for $\tau_w = \bar{\tau}_{xz}|_{z=0}$ in FDS is the Werner and Wengle model [25] which we now describe.

An important scaling quantity in the near-wall region is the friction velocity, defined as $u^* \equiv \sqrt{\tau_w/\rho}$. From the friction velocity we define the nondimensional streamwise velocity $u^+ \equiv u/u^*$ and nondimensional wall-normal distance $z^+ \equiv z/\ell$, where $\ell = \mu/(\rho u^*)$. The law of the wall is then given by [26, 27]

$$\begin{aligned} u^+ &= z^+ & \text{for} \quad z^+ < 5 & \quad (3.21)\\ u^+ &= 2.4\ln z^+ + 5.2 & \text{for} \quad z^+ > 30, & \quad (3.22) \end{aligned}$$

The region $5 < z^+ < 30$, where both viscous and inertial stresses are important, is referred to as the buffer layer. The upper range of the log law depends on the Reynolds number [26, 28].

Werner and Wengle [25] propose a simplification to the law of the wall to eliminate the mathematical difficulties of handling the buffer and log layers. Furthermore, WW suppose that their simplified formula for the streamwise velocity holds *instantaneously* within the LES. The WW wall law is given by [29]

$$\begin{aligned} u^+ &= z^+ & \text{for} \quad z^+ \leq 11.81 & \quad (3.23)\\ u^+ &= A(z^+)^B & \text{for} \quad z^+ > 11.81, & \quad (3.24) \end{aligned}$$

where $A = 8.3$ and $B = 1/7$. Note that a power law has been substituted for the log law and the viscous sublayer and the power law region are matched within the buffer region. A comparison of the log law and the power law is shown in Figure 3.1. In the region $11.81 < z^+ < 10^3$ the power law is a good approximation to the log law and for $z^+ > 10^3$ the power law loosely exhibits wake region behavior for a flow with Re $\approx 5e5$ [26, 28]. As we see below, this functional behavior has consequences for high Re flows.

For the purposes of adapting the WW model to FDS we suppose that the first off-wall velocity component $\tilde{u}$ represents the WW profile averaged in the wall-normal direction (refer to Figure 3.2). The density is taken as the average of the neighboring cell values and uniform along the face. The WW model as implemented in FDS is then given by

$$|\tau_w| = \frac{2\bar{\mu}|\tilde{u}|}{\Delta z} \qquad\qquad \text{for} \quad z^+ \leq 11.81 \qquad (3.25)$$
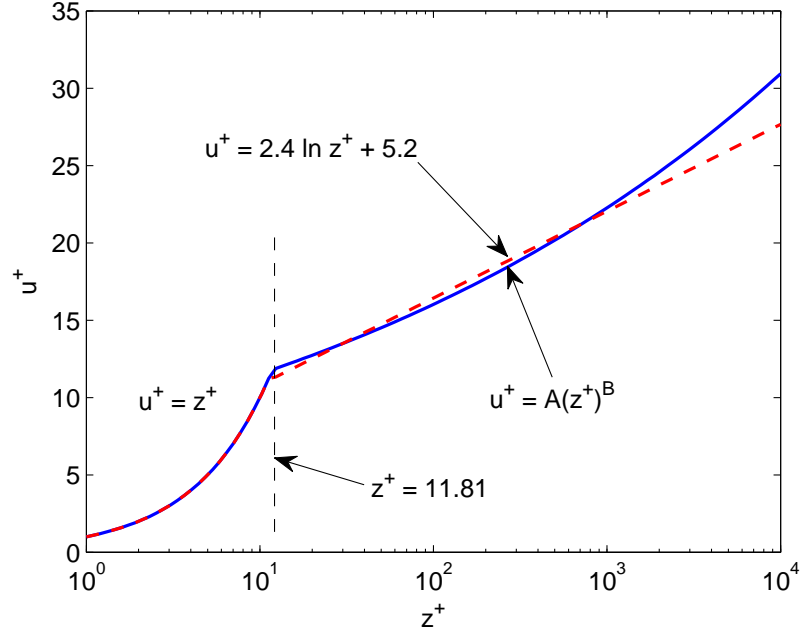
Figure 3.1: The law of the wall. We have omitted the buffer layer since it is not considered in the WW model. For $z^+ \leq 11.81$ we have the viscous sublayer. For $z^+ > 11.81$ we show a comparison of the log law (3.22) (red dashed line) and the WW power law (3.24) (blue solid line) with $A = 8.3$ and $B = 1/7$.

$$|\tau_w| = \bar{\rho} \left[\alpha \left(\frac{\bar{\mu}}{\bar{\rho} \Delta z} \right)^\beta + \eta \left(\frac{\bar{\mu}}{\bar{\rho} \Delta z} \right)^B |\tilde{u}| \right]^\gamma \quad \text{for} \quad z^+ > 11.81, \tag{3.26}$$

where

$$\alpha = \frac{1-B}{2} A^{\frac{1+B}{1-B}} \tag{3.27}$$

$$\beta = 1+B \tag{3.28}$$

$$\eta = \frac{1+B}{A} \tag{3.29}$$

$$\gamma = \frac{2}{1+B} \tag{3.30}$$

Note that $\bar{\mu}$ is the average of the *molecular* viscosity from the neighboring cells. A detailed derivation of (3.26) is given in Appendix E.

In order to decide which formula to use for the wall stress, (3.25) or (3.26), we must know z^+, which of course depends on τ_w. As a practical matter of implementation, given that most boundary layers in FDS are under-resolved, we first calculate τ_w from (3.26); we then obtain $z^+ = \sqrt{\tau_w/\bar{\rho}}$; if $z^+ > 11.81$, then the computed value of τ_w is retained, else τ_w is taken from (3.25), which actually involves no additional computation since the ghost cell value for the velocity is prescribed for a no-slip wall by default.
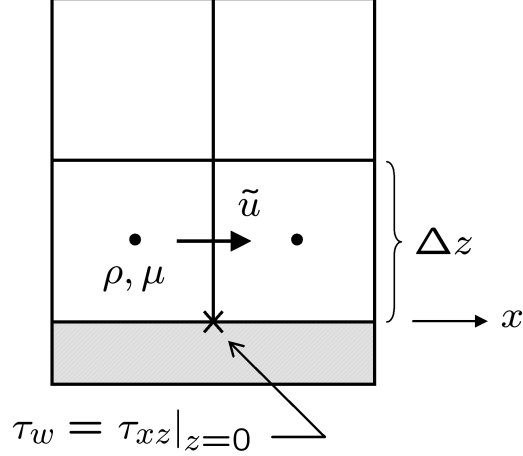
Figure 3.2: Near-wall grid.

3.1.5 The Equation for Pressure (Poisson's Equation)

The reason for either neglecting the baroclinic torque or decomposing the pressure term in the momentum equation is to simplify the elliptic partial differential equation obtained by taking the divergence of the momentum equation

$$\nabla^2 \mathcal{H} = -\frac{\partial(\nabla \cdot \mathbf{u})}{\partial t} - \nabla \cdot \mathbf{F} \quad ; \quad \mathbf{F} = -\mathbf{u} \times \omega + \left(\frac{1}{\rho} - \frac{1}{\rho_\infty}\right) \nabla \tilde{p} - \frac{1}{\rho}\left((\rho - \rho_0)\mathbf{g} + \mathbf{f}_b + \nabla \cdot \tau_{ij}\right) \qquad (3.31)$$

Note that the pressure $\tilde{p}$ appears on both sides of Eq. (3.31). The pressure on the right hand side is taken from the previous time step of the overall explicit time-marching scheme. It can be neglected if the baroclinic torque is not considered important in a given simulation. The pressure on the left hand side (incorporated in the variable $\mathcal{H}$) is solved for directly. The reason for the decomposition of the pressure term is so that the linear algebraic system arising from the discretization of Eq. (3.31) has constant coefficients (*i.e.* it is *separable*) and can be solved to machine accuracy by a fast, direct (*i.e.* non-iterative) method that utilizes Fast Fourier Transforms (FFT). No-flux or forced-flow boundary conditions are specified by asserting that

$$\frac{\partial \mathcal{H}}{\partial n} = -F_n - \frac{\partial u_n}{\partial t} \qquad (3.32)$$

where F_n is the normal component of $\mathbf{F}$ at the vent or solid wall, and $\partial u_n/\partial t$ is the specified rate of change in the normal component of velocity at a forced vent. Initially, the velocity is zero everywhere.

At open external boundaries the pressure term $\mathcal{H}$ is specified depending on whether the flow is outgoing or incoming

$$\begin{aligned} \mathcal{H} &= |\mathbf{u}|^2/2 \quad \text{outgoing} \\ \mathcal{H} &= 0 \qquad\quad \text{incoming} \end{aligned} \qquad (3.33)$$

The outgoing boundary condition assumes that the pressure perturbation $\tilde{p}$ is zero at an outgoing boundary and that $\mathcal{H}$ is constant along streamlines. The incoming boundary condition assumes that $\mathcal{H}$ is zero infinitely far away. At the boundary between two meshes, the pressure boundary condition is similar to that at an external open boundary, except that where the flow is incoming, $\mathcal{H}$ is taken from the adjacent mesh.

3.1.6 Large Eddy Simulation (LES)

The most distinguishing feature of any CFD model is its treatment of turbulence. Chapter 1 contains a brief history of turbulence modeling as it has been applied to the fire problem. Of the three main techniques of

simulating turbulence, FDS contains only Large Eddy Simulation (LES) and Direct Numerical Simulation (DNS). There is no Reynolds-Averaged Navier-Stokes (RANS) capability in FDS.

LES is a technique used to model the dissipative processes (viscosity, thermal conductivity, material diffusivity) that occur at length scales smaller than those that are explicitly resolved on the numerical grid. This means that the parameters μ, k and D in the equations above cannot be used directly in most practical simulations. They must be replaced by surrogate expressions that "model" their impact on the approximate form of the governing equations. This section contains a simple explanation of how these terms are modeled in FDS. Note that this discussion is quite different than what it typically found in the literature, thus the reader is encouraged to consider other explanations of the technique in the references that are listed in a review article by Pope [30].

Recall from Section 3.1.1 that there is a small term in the energy equation known as the dissipation rate ε, the rate at which kinetic energy is converted to thermal energy by viscosity. To understand where this term originates, form an evolution equation for the kinetic energy of the fluid by taking the dot product of the momentum equation (3.2) with the velocity vector[1]:

$$\rho \frac{\mathrm{D}\mathbf{u}}{\mathrm{D}t} \cdot \mathbf{u} = \rho \frac{\mathrm{D}\left(|\mathbf{u}|^2/2\right)}{\mathrm{D}t} = \rho \mathbf{f}_b \cdot \mathbf{u} - \nabla p \cdot \mathbf{u} + \nabla \cdot (\tau_{ij} \cdot \mathbf{u}) - \varepsilon \tag{3.34}$$

As mentioned above ε is a neglible quantity in the energy equation. However, its functional form is useful in representing the dissipation of kinetic energy from the resolved flow field. Following the analysis of Smagorinsky [31], the viscosity μ is modeled

$$\mu_{\mathrm{LES}} = \rho \left(C_s \Delta\right)^2 \left(2\,\overline{\mathbf{S}}_{ij} : \overline{\mathbf{S}}_{ij} - \frac{2}{3}(\nabla \cdot \overline{\mathbf{u}})^2\right)^{\frac{1}{2}} \tag{3.35}$$

where C_s is an empirical constant and Δ is a length on the order of the size of a grid cell. The bar above the various quantities denotes that these are the resolved values, meaning that they are computed from the numerical solution sampled on a coarse grid (relative to DNS). The other diffusive parameters, the thermal conductivity and material diffusivity, are related to the turbulent viscosity by

$$k_{\mathrm{LES}} = \frac{\mu_{\mathrm{LES}}\,c_p}{\mathrm{Pr}_t} \quad ; \quad (\rho D)_{l,\mathrm{LES}} = \frac{\mu_{\mathrm{LES}}}{\mathrm{Sc}_t} \tag{3.36}$$

The turbulent Prandtl number Pr_t and the turbulent Schmidt number Sc_t are assumed to be constant for a given scenario.

The model for the viscosity, μ_{LES}, serves two roles: first, it provides a stabilizing effect in the numerical algorithm, damping out numerical instabilities as they arise in the flow field, especially where vorticity is generated. Second, it has the appropriate mathematical form to describe the dissipation of kinetic energy from the flow. Note the similar mathematical form of μ_{LES} and the dissipation rate, ε, defined in Eq. (3.8). In the parlance of the turbulence community, the dissipation rate is related to the turbulent kinetic energy (most often denoted by k) by the relation $\varepsilon \approx k^{3/2}/L$, where L is a length scale.

There have been numerous refinements of the original Smagorinsky model [32, 33, 34], but it is difficult to assess the improvements offered by these newer schemes for fires. There are two reasons for this. First, the structure of the fire plume is so dominated by the large-scale resolvable eddies that even a constant eddy viscosity gives results comparable to those obtained using the Smagorinsky model [35]. Second, the lack of precision in most large-scale fire test data makes it difficult to assess the relative accuracy of each model. The Smagorinsky model with constant C_s produces satisfactory results for most large-scale applications where boundary layers are not well-resolved (see Volume 3, *Experimental Validation*). In fact, experience to date using the simple form of LES described above has shown that the best results are obtained when the

---

[1]In this section it is convenient to work with the Lagrangian form of the conservation equations.

Smagorinsky constant C_s is set as low as possible to maintain numerical stability. In other words, the most realistic flow simulations are obtained when resolvable eddies are not "damped" by excessive amounts of artificial viscosity.

3.1.7 Direct Numerical Simulation (DNS)

There are some flow scenarios where it is possible to use the molecular properties μ, k and D directly. Usually, this means that the numerical grid cells are on the order of 1 mm or less, and the simulation is regarded as a Direct Numerical Simulation (DNS). For a DNS, the viscosity, thermal conductivity and material diffusivity are approximated from kinetic theory because the temperature dependence of each is important in combustion scenarios. The viscosity of the species α is given by

$$\mu_\alpha = \frac{26.69 \times 10^{-7} (W_\alpha T)^{\frac{1}{2}}}{\sigma_\alpha^2 \Omega_v} \qquad \frac{\text{kg}}{\text{m s}} \tag{3.37}$$

where σ_α is the Lennard-Jones hard-sphere diameter () and Ω_v is the collision integral, an empirical function of the temperature T. The thermal conductivity of species α is given by

$$k_\alpha = \frac{\mu_\alpha c_{p,\alpha}}{\text{Pr}} \qquad \frac{\text{W}}{\text{m K}} \tag{3.38}$$

where the Prandtl number Pr is 0.7. The viscosity and thermal conductivity of a gas mixture are given by

$$\mu_{\text{DNS}} = \sum_\alpha Y_\alpha \mu_\alpha \quad ; \quad k_{\text{DNS}} = \sum_\alpha Y_\alpha k_\alpha \tag{3.39}$$

The binary diffusion coefficient of species α diffusing into species β is given by

$$D_{\alpha\beta} = \frac{2.66 \times 10^{-7} T^{3/2}}{W_{\alpha\beta}^{\frac{1}{2}} \sigma_{\alpha\beta}^2 \Omega_D} \qquad \frac{\text{m}^2}{\text{s}} \tag{3.40}$$

where $W_{\alpha\beta} = 2(1/W_\alpha + 1/W_\beta)^{-1}$, $\sigma_{\alpha\beta} = (\sigma_\alpha + \sigma_\beta)/2$, and Ω_D is the diffusion collision integral, an empirical function of the temperature, T [36]. It is assumed that nitrogen is the dominant species in any combustion scenario considered here, thus the diffusion coefficient in the species mass conservation equations is that of the given species diffusing into nitrogen

$$(\rho D)_{\alpha,\text{DNS}} = \rho D_{\alpha 0} \tag{3.41}$$

where species 0 is nitrogen.

3.2 Combustion Model

There are two types of combustion models used in FDS. The default model makes use of the mixture fraction, a quantity representing the fuel and the products of combustion. For the second model, individual gas species react according to specified Arrhenius reaction parameters. This latter model is most often used in a direct numerical simulation (DNS) where the diffusion of fuel and oxygen can be modeled directly. However, most often for large eddy simulations (LES), where the grid is not fine enough to resolve the diffusion of fuel and oxygen, the mixture fraction-based combustion model is assumed.

3.2.1 Mixture Fraction Combustion Model

Given a volume containing a mixture of gas species, a mixture fraction can be defined that is the ratio of the mass of a subset of the species to the total mass present in the volume. In combustion, the mixture fraction is a conserved quantity traditionally defined as the (mass) fraction of the gas mixture that originates in the fuel stream. Thus, at a burner surface the mixture fraction is 1 and in fresh air it is 0. In a region where combustion has occurred this fraction will be comprised of any unburned fuel and that portion of the combustion products that came from the fuel. The mixture fraction is a function of space and time, commonly denoted $Z(\mathbf{x},t)$. If it can be assumed that, upon mixing, the reaction of fuel and oxygen occurs rapidly and completely, the combustion process is referred to as "mixing-controlled." This implies that all species of interest can be described in terms of the mixture fraction alone. The correspondence between the mass fraction of an individual species and the mixture fraction is called its "state relation." FDS versions 2 through 4 assumed that the gas mixture could be uniquely determined by the mixture fraction alone, an assumption that implies that fuel and oxygen react instantaneously upon mixing.

For many applications, "mixed is burned" is a reasonable assumption. However, for fire scenarios where it cannot be assumed that fuel and oxygen react completely upon mixing, for example in under-ventilated compartments. The mixture fraction itself remains a valid quantity, but it can no longer be assumed that it completely defines the composition of the gas mixture. If fuel and oxygen are to mix and not burn, at least two scalar variables are needed to describe the extent to which the fuel and oxygen react. The strategy for moving beyond the "mixed is burned" model is as follows. Instead of solving a single transport equation for the mixture fraction Z, multiple transport equations are solved for components of the mixture fraction Z_α. Fuel mass is still conserved, since $\sum Z_\alpha = Z$. For example, if Z_1 represents the (unburned) fuel mass fraction, Y_F, and we define $Z_2 = Z - Z_1$, then Z_2 is the mass fraction of burned fuel and is the component of Z that originates from the combustion products. With this approach it is possible to account for the mixing of fuel and oxygen without burning. In the sections to follow, various multi-step reaction mechanisms are discussed using this system of accounting. First, however, the single-step mixture fraction model is described.

A Single-Step, Instantaneous Reaction

Consider a simple, one-step reaction of fuel and oxygen:

$$C_x H_y O_z N_a M_b + \nu_{O_2} O_2 \rightarrow \nu_{CO_2} CO_2 + \nu_{H_2O} H_2O + \nu_{CO} CO + \nu_S S + \nu_{N_2} N_2 + \nu_M M \tag{3.42}$$
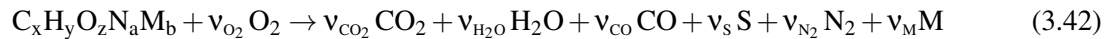
Note that the nitrogen in the fuel molecule is assumed to form N_2 only. Addition product species can be specified as some number of moles of an average molecular weight species M. These products are presumed to not consume oxygen during their formation. Soot is assumed to be a mixture of carbon and hydrogen with the hydrogen atomic fraction given by X_H. The stoichiometric coefficient, ν_S, represents the amount of fuel that is converted to soot. It is related to the *soot yield*, y_S, via the relation:

$$\nu_S = \frac{W_F}{W_S} y_S \quad ; \quad W_S = X_H W_H + (1 - X_H) W_C \tag{3.43}$$

Likewise, the stoichiometric coefficient of CO, ν_{CO}, is related to the CO *yield*, y_{CO}, via:

$$\nu_{CO} = \frac{W_F}{W_{CO}} \, y_{CO} \tag{3.44}$$

The yields of soot and CO are based on "well-ventilated" or "post-flame" measurements. The increased production of CO and soot in an under-ventilated compartment will be addressed in the following sections.

The traditional way of expressing the mixture fraction, Z, is as a linear combination of fuel and oxygen mass fractions:

$$Z = \frac{sY_F - (Y_{O_2} - Y_{O_2}^{\infty})}{sY_F^I + Y_{O_2}^{\infty}} \quad ; \quad s = \frac{\nu_{O_2}W_{O_2}}{\nu_F W_F} \quad ; \quad \nu_F = 1 \tag{3.45}$$

where Y_F^I is the fuel mass fraction in fuel stream.[2] However, the mixture fraction can also be defined in terms of the mass fraction of fuel and the carbon-carrying products of combustion:

$$Z = \frac{1}{Y_F^I} \left(Y_F + \frac{W_F}{xW_{CO_2}} Y_{CO_2} + \frac{W_F}{xW_{CO}} Y_{CO} + \frac{W_F}{xW_S} Y_S \right) \tag{3.46}$$

Note that x is the number of carbon atoms in the fuel molecule. The mixture fraction satisfies the conservation equation

$$\rho \frac{DZ}{Dt} = \nabla \cdot \rho D \nabla Z \tag{3.47}$$

obtained by taking a linear combination of the transport equations for the fuel and the carbon carrying products. If it is assumed that combustion occurs so rapidly that the fuel and oxygen cannot co-exist, then both simultaneously vanish at a flame surface:

$$Z(\mathbf{x},t) = Z_f \quad ; \quad Z_f = \frac{Y_{O_2}^{\infty}}{sY_F^I + Y_{O_2}^{\infty}} \tag{3.48}$$

and all species can be related to Z via the "state relations" shown in Fig. 3.3. In versions of FDS prior to 5, this one-step, instantaneous reaction of fuel and oxygen was assumed. However, starting in version 5, a more generalized formulation has been implemented and is described next. For this reason, it is more convenient to work with the definition of Z in Eq. (3.46). The traditional definition, Eq. (3.45), is more convenient when it is assumed that fuel and oxygen cannot co-exist and that the combustion occurs at an infinitely thin flame sheet.

A Single-Step Reaction, but with Local Extinction

The physical limitation of the single-step reaction model described in the previous section is that it assumes fuel and oxygen burn instantaneously when mixed. For large-scale, well-ventilated fires, this is a good assumption. However, if a fire is in an under-ventilated compartment, or if a suppression agent like water mist or CO_2 is introduced, or if the shear layer between fuel and oxidizing streams has a sufficiently large local strain rate, fuel and oxygen may mix but may not burn. The physical mechanisms underlying these phenomena are complex, and even simplified models still rely on an accurate prediction of the flame temperature and local strain rate. Subgrid-scale modeling of gas phase suppression and extinction is still an area of active research in the combustion community.

Simple empirical rules can be used to predict local extinction based on the oxygen concentration and temperature of the gases in the vicinity of the flame sheet. Figure 3.4 shows values of temperature and oxygen concentration for which burning can and cannot take place. A derivation of the model, based on the
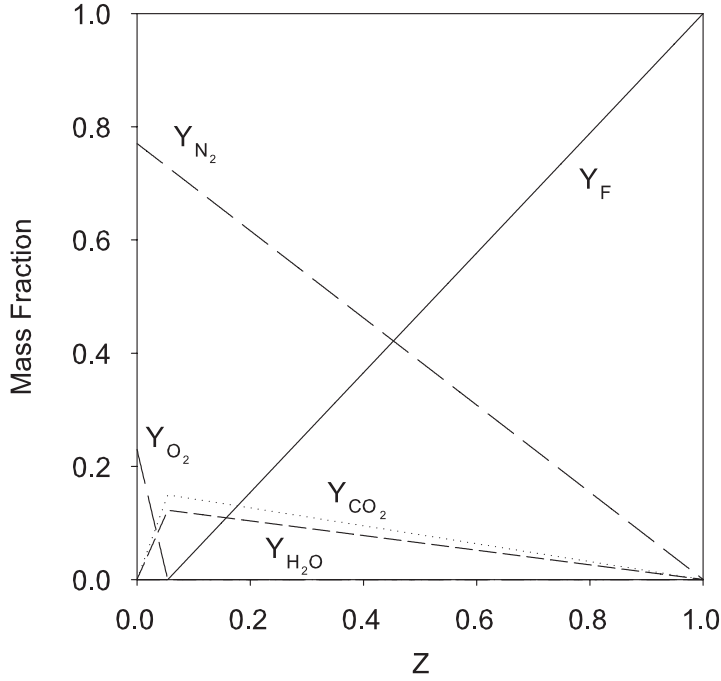
Figure 3.3: State relations for methane.

critical flame temperature concept, is given in Appendix D. Note that once the local state of the gases falls into the "No Burn" zone, the state relations (Fig. 3.3) are no longer valid for values of Z below stoichiometric, since now some fuel may be mixed with the other combustion products. Essentially, there are now two reactions to consider – the "null" reaction, where fuel and oxygen simply mix and do not burn; and the "complete" reaction, where fuel and oxygen react and form products according to Eq. (3.42). Note that the term "complete" does not imply that no soot or CO is formed, but rather that their respective production rates are proportional to the fuel consumption rate.

With the definition of the mixture fraction, Eq. (3.46), in mind, consider a partitioning of Z into the following components:

$$Z_1 = \frac{Y_\mathrm{F}}{Y_F^I} \tag{3.49}$$

$$Z_2 = \frac{1}{Y_F^I} \left(\frac{W_\mathrm{F}}{x\,W_{\mathrm{CO}_2}} Y_{\mathrm{CO}_2} + \frac{W_\mathrm{F}}{x\,W_{\mathrm{CO}}} Y_{\mathrm{CO}} + \frac{W_\mathrm{F}}{x\,W_\mathrm{S}} Y_\mathrm{S} \right) \tag{3.50}$$

such that $Z = Z_1 + Z_2$. Transport equations are required for both Z_1 and Z_2. At the burner surface, Z_1 is assigned the mass flux of fuel, while the mass flux for Z_2 is zero. In other words, no combustion products are generated at the fuel source. Where fuel and oxygen co-exist, a reaction occurs if conditions are favorable in the sense shown by Fig. 3.4. If a reaction occurs, Z_1 is converted to Z_2 representing the conversion of fuel to products. The heat release rate of the fire is obtained by multiplying the fuel consumption rate by the heat of combustion.

---

[2]It is assumed throughout that nitrogen is the only possible diluent in the fuel stream, and its mass fraction is denoted by $Y_{\mathrm{N}_2}^I$.
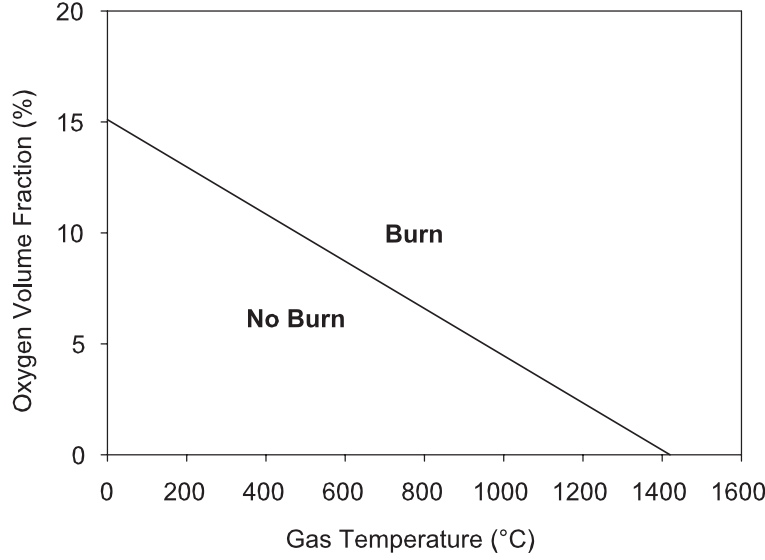
Figure 3.4: Oxygen-temperature phase space showing where combustion is allowed and not allowed to take place.

If it is assumed that the yields of CO and soot are fixed, Eq. (3.49) and Eq. (3.50) can be simplified further:

$$Z_1 = \frac{Y_F}{Y_F^I} \tag{3.51}$$

$$Z_2 = \frac{W_F}{\left[x - v_{CO} - (1 - X_H)v_S\right]W_{CO_2}} \frac{Y_{CO_2}}{Y_F^I} \tag{3.52}$$

In this way, CO_2 becomes the surrogate for all combustion products.

Since the mixture fraction variables result from linear combinations of the species transport equations, the converse is also true – that species mass fractions are linear combinations of the mixture fraction variables. The mass fractions of the species in the mixture, $Y_\alpha(Z_1, Z_2)$, are found via:

$$Y_F = Y_F^I Z_1 \qquad\qquad Y_{H_2O} = \frac{v_{H_2O}W_{H_2O}}{W_F} Y_F^I Z_2 \tag{3.53}$$

$$Y_{N_2} = (1-Z)Y_{N_2}^\infty + Y_{N_2}^I Z_1 + \frac{v_{N_2}W_{N_2}}{W_F} Y_F^I Z_2 \qquad\qquad Y_{CO} = \frac{v_{CO}W_{CO}}{W_F} Y_F^I Z_2 \tag{3.54}$$

$$Y_{O_2} = (1-Z)Y_{O_2}^\infty - \frac{v_{O_2}W_{O_2}}{W_F} Y_F^I Z_2 \qquad\qquad Y_S = \frac{v_S W_S}{W_F} Y_F^I Z_2 \tag{3.55}$$

$$Y_{CO_2} = \frac{v_{CO_2}W_{CO_2}}{W_F} Y_F^I Z_2 \qquad\qquad Y_M = \frac{v_M W_M}{W_F} Y_F^I Z_2 \tag{3.56}$$

The stoichiometric coefficients are defined:

28

$$\nu_{N_2} = \frac{a}{2} \qquad\qquad \nu_{H_2O} = \frac{y}{2} - X_H \nu_S \qquad (3.57)$$

$$\nu_{O_2} = \nu_{CO_2} + \frac{\nu_{CO} + \nu_{H_2O} - z}{2} \qquad\qquad \nu_{CO} = \frac{W_F}{W_{CO}} y_{CO} \qquad (3.58)$$

$$\nu_{CO_2} = x - \nu_{CO} - (1 - X_H)\nu_S \qquad\qquad \nu_S = \frac{W_F}{W_S} y_S \qquad (3.59)$$

$$\nu_M = b$$

Remember that x is the number of carbon atoms and z is the number of oxygen atoms in the fuel molecule. It is important to note that the definitions of Z_1 and Z_2, unlike in the single parameter model, do not imply anything regarding the rate of combustion, only that the combustion occurs in a single step.

CO Production (Two-Step Reaction with Extinction)

The previous section describes the "complete" reaction as the conversion of fuel to products such that the production rate of each product species is proportional to the fuel consumption rate. This means that for each fuel molecule, fixed amounts of CO_2, H_2O, CO, and soot are formed and these products persist in the plume indefinitely with no further reaction. This is not an unreasonable assumption if the purpose of the fire simulation is to assess the impact of the fire on the larger space. However, in under-ventilated fires, soot and CO are produced at higher rates, and exist within the fuel-rich flame envelope at higher concentrations, than would otherwise be predicted with a single set of fixed yields that are based on post-flame measurements. To account for the production of CO and its eventual oxidation at the flame envelope or within a hot upper layer, an additional reaction is now needed:

$$C_x H_y O_z N_a M_b + \nu'_{O_2} O_2 \;\rightarrow\; \nu_{H_2O} H_2O + (\nu'_{CO} + \nu_{CO})CO + \nu_S S + \nu_{N_2} N_2 + \nu_M M \qquad (3.60)$$

$$\nu'_{CO}\left[CO + \frac{1}{2} O_2 \;\rightarrow\; CO_2 \right] \qquad (3.61)$$
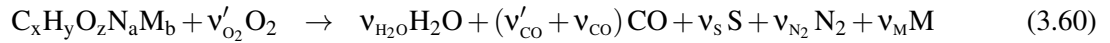
The brackets around the second reaction are there merely to emphasize that the sum of the two reactions equal Eq. (3.42). There are two stoichiometric coefficients for CO – the first, $\nu'_{CO} = x - (1 - X_H)\nu_S - \nu_{CO}$, represents CO that is produced in the first step of the reaction that can potentially be converted to CO_2 assuming the conditions are favorable. ν'_{CO} is equivalent to ν_{CO_2} in Eq. (3.42). The second coefficient, ν_{CO}, is the so-called "well-ventilated," or "post-flame," value that was introduced in the previous section. The proposed model of CO production still does not contain the necessary kinetic mechanism to predict the "post-flame" concentration of CO without the prescription of the measured value of the post-flame CO yield. Rather, the proposed model includes the production of large amounts of CO in the first step of a two-step reaction, followed by a partial conversion to CO_2 if there is a sufficient amount of oxygen present.

To describe the composition of the gas species, the mixture fraction, Z, must now be decomposed into three components:

$$Z_1 = \frac{Y_F}{Y_F^I} \qquad (3.62)$$

$$Z_2 = \frac{W_F}{[x - (1 - X_H)\nu_S] W_{CO}} \frac{Y_{CO}}{Y_F^I} \qquad (3.63)$$

$$Z_3 = \frac{W_F}{[x - (1 - X_H)\nu_S] W_{CO_2}} \frac{Y_{CO_2}}{Y_F^I} \qquad (3.64)$$

Here, $x - (1 - X_H)\nu_S$ represents the number of carbon atoms in the fuel molecule that are oxidized; that is, the carbon atoms that are not converted to soot. The decomposition of Z into three components is numerically convenient. However, the recovery of the individual species mass fractions requires some care. The mass fraction of any species in the mixture, $Y_\alpha(Z_1, Z_2, Z_3)$, is still found via linear combinations of the mixture fraction variables:

$$Y_F = Z_1 Y_F^I \qquad\qquad Y_{H_2O} = \frac{\nu_{H_2O} W_{H_2O}}{W_F} Y_F^I (Z_2 + Z_3) \qquad (3.65)$$

$$Y_{N_2} = (1 - Z) Y_{N_2}^\infty + Y_{N_2}^I Z_1 + \frac{\nu_{N_2} W_{N_2}}{W_F} Y_F^I (Z_2 + Z_3) \qquad Y_{CO} = \frac{(\nu_{CO} + \nu_{CO}')W_{CO_2}}{W_F} Y_F^I Z_2 \qquad (3.66)$$

$$Y_{O_2} = (1 - Z) Y_{O_2}^\infty - \frac{W_{O_2} Y_F^I}{W_F}(\nu_{O_2}' Z_2 + \nu_{O_2} Z_3) \qquad Y_S = \frac{\nu_S W_S}{W_F} Y_F^I (Z_2 + Z_3) \qquad (3.67)$$

$$Y_{CO_2} = \frac{\nu_{CO_2} W_{CO_2}}{W_F} Y_F^I Z_3 \qquad\qquad Y_M = \frac{\nu_M W_M}{W_F} Y_F^I (Z_2 + Z_3) \qquad (3.68)$$

The stoichiometric coefficients are defined:

$$\nu_{N_2} = \frac{a}{2}$$
$$\nu_{H_2O} = \frac{y}{2} - X_H \nu_S \qquad (3.69)$$

$$\nu_{O_2}' = \frac{\nu_{CO}' + \nu_{H_2O} - z}{2}$$
$$\nu_{CO}' = x - \nu_{CO} - (1 - X_H)\nu_S \qquad (3.70)$$

$$\nu_{O_2} = \nu_{CO_2} + \frac{\nu_{CO} + \nu_{H_2O} - z}{2}$$
$$\nu_{CO} = \frac{W_F}{W_{CO}} y_{CO} \qquad (3.71)$$

$$\nu_{CO_2} = x - (1 - X_H)\nu_S$$
$$\nu_S = \frac{W_F}{W_S} y_S \qquad (3.72)$$

$$\nu_M = b$$

Although these formulae appear complicated, most are determined directly from the composition of the fuel molecule. The only information expected of the modeler are the fuel composition, the soot and CO yields, and the atomic fraction of hydrogen in the soot.

Heat Release Rate

The discussion of the various multi-step reactions above is essentially book-keeping, the accounting of the gas molecules formed in the combustion process. But what of the heat released?

When tracking species with two mixture fraction parameters, there is a single step reaction, the conversion of fuel into a fixed, predefined set of combustion products. Fuel and oxygen react within a grid cell and release energy according to the rate of fuel consumption:

$$\dot{q}''' = \dot{m}_F''' \Delta H_F \qquad (3.73)$$

The amount of fuel in the grid cell is obtained directly from the definition of Z_1 whereas the amount of O_2 is obtained using the state relationships discussed in the prior section. Combustion is either allowed or disallowed[3] using the relation shown in Fig. 3.4. If combustion is allowed to occur in a grid cell, the single step combustion is assumed to be infinitely fast. Combustion will consume all of either the fuel or the oxygen in the grid cell.

---

[3]Note that the user has control over the parameters associated with local gas phase extinction.

In the case of the two-step, three parameter mixture fraction model, the first step converts the fuel to CO and other combustion products, and the second step oxidizes the CO into CO_2. The first step is determined as it is for the single step reaction. The second step, however, is assumed to be rate dependent. Determining if the second step can take place in a grid cell is done in one of two ways. For most LES simulations, flame temperatures will not be resolved on the grid because the heat released is smeared out over a grid cell much larger than the flame sheet thickness. Since a grid cell with heat released from the first step has a flame, CO conversion is always allowed in these grid cells. In all other grid cells, the local temperature is used to perform a finite-rate computation that determines the rate of CO conversion.

On-Going Research

One can envision extending the three parameter mixture fraction model to a fourth parameter for soot production:

$$Z_4 = \frac{W_F}{x W_S} Y_S \tag{3.74}$$

This extension would allow for combustion models that predict soot formation along with extinction and CO production.

Additional partitionings of the mixture fraction could be added as well; however, there is a point of diminishing returns. The present advantage of using a mixture fraction approach is to track the movement of a number of gas species using a smaller number of scalar variables at the expense of having to use state relationships to obtain species mass fractions. As more mixture fraction variables are added, the net savings in fewer species transport equations vs. the expense of state relationships will diminish.

3.2.2 Finite-Rate Reaction (DNS)

In a DNS calculation, the fine grid resolution enables the direct modeling of the diffusion of chemical species (fuel, oxygen, and combustion products). Since the flame is being resolved in a DNS calculation, the local gas temperatures can be used to determine the reaction kinetics. Thus, it is possible to implement a relatively simple set of one or more chemical reactions to model the combustion. Consider the reaction of oxygen and a hydrocarbon fuel

$$C_x H_y + \nu_{O_2} O_2 \longrightarrow \nu_{CO_2} CO_2 + \nu_{H_2O} H_2O \tag{3.75}$$
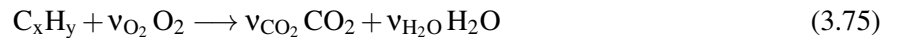
If this were modeled as a single-step reaction, the reaction rate would be given by the expression

$$\frac{d[C_x H_y]}{dt} = -B [C_x H_y]^a [O_2]^b e^{-E/RT} \tag{3.76}$$

Suggested values of B, E, a and b for various hydrocarbon fuels are given in Refs. [37, 38]. It should be understood that the implementation of any of these one-step reaction schemes is still very much a research exercise because it is not universally accepted that combustion phenomena can be represented by such a simple mechanism. Improved predictions of the heat release rate may be possible by considering a multi-step set of reactions. However, each additional gas species defined in the computation incurs a roughly 5 % increase in the CPU time.

3.3 Thermal Radiation

Energy transport consists of convection, conduction and radiation. Convection of heat is accomplished via the solution of the basic conservation equations. Gains and losses of heat via conduction and radiation are represented by the divergence of the heat flux vector in the energy equation, $\nabla \cdot \dot{\mathbf{q}}''$. This section describes the equations associated with the radiative part, $\dot{\mathbf{q}}''_r$.

The Radiative Transport Equation (RTE) for an absorbing/emitting and scattering medium is

$$\mathbf{s} \cdot \nabla I_\lambda(\mathbf{x}, \mathbf{s}) = -\left[\kappa(\mathbf{x}, \lambda) + \sigma_s(\mathbf{x}, \lambda) \right] I_\lambda(\mathbf{x}, \mathbf{s}) + B(\mathbf{x}, \lambda) + \frac{\sigma_s(\mathbf{x}, \lambda)}{4\pi} \int_{4\pi} \Phi(\mathbf{s}, \mathbf{s}') \, I_\lambda(\mathbf{x}, \mathbf{s}') \, d\mathbf{s}' \tag{3.77}$$

where $I_\lambda(\mathbf{x}, \mathbf{s})$ is the radiation intensity at wavelength λ, $\mathbf{s}$ is the direction vector of the intensity, $\kappa(\mathbf{x}, \lambda)$ and $\sigma_s(\mathbf{x}, \lambda)$ are the local absorption and scattering coefficients, respectively, and $B(\mathbf{x}, \lambda)$ is the emission source term. The integral on the right hand side describes the in-scattering from other directions. In the case of a non-scattering gas the RTE becomes

$$\mathbf{s} \cdot \nabla I_\lambda(\mathbf{x}, \mathbf{s}) = \kappa(\mathbf{x}, \lambda) \left[I_b(\mathbf{x}) - I_\lambda(\mathbf{x}, \mathbf{s}) \right] \tag{3.78}$$

where $I_b(\mathbf{x})$ is the source term given by the Planck function (see below).

In practical simulations the spectral (λ) dependence cannot be solved accurately. Instead, the radiation spectrum is divided into a relatively small number of bands and a separate RTE is derived for each band. The band specific RTE is

$$\mathbf{s} \cdot \nabla I_n(\mathbf{x}, \mathbf{s}) = \kappa_n(\mathbf{x}) \left[I_{b,n}(\mathbf{x}) - I_n(\mathbf{x}, \mathbf{s}) \right], \quad n = 1...N \tag{3.79}$$

where I_n is the intensity integrated over the band n, and κ_n is the appropriate mean absorption coefficient inside the band. The source term can be written as a fraction of the blackbody radiation

$$I_{b,n} = F_n(\lambda_{\min}, \lambda_{\max}) \, \sigma \, T^4 / \pi \tag{3.80}$$

where σ is the Stefan-Boltzmann constant. The calculation of factors F_n is explained in Ref. [19]. When the intensities corresponding to the bands are known, the total intensity is calculated by summing over all the bands

$$I(\mathbf{x}, \mathbf{s}) = \sum_{n=1}^{N} I_n(\mathbf{x}, \mathbf{s}) \tag{3.81}$$

Even with a reasonably small number of bands, solving multiple RTEs is very time consuming. Fortunately, in most large-scale fire scenarios soot is the most important combustion product controlling the thermal radiation from the fire and hot smoke. As the radiation spectrum of soot is continuous, it is possible to assume that the gas behaves as a gray medium. The spectral dependence is then lumped into one absorption coefficient ($N = 1$) and the source term is given by the blackbody radiation intensity

$$I_b(\mathbf{x}) = \sigma T(\mathbf{x})^4 / \pi \tag{3.82}$$

This is the default mode of FDS and appropriate for most problems of fire engineering. In optically thin flames, where the amount of soot is small compared to the amount of CO_2 and water, the gray gas assumption may produce significant overpredictions of the emitted radiation. From a series of numerical experiments it has been found that six bands ($N = 6$) are usually enough to improve the accuracy in these cases. The limits of the bands are selected to give an accurate representation of the most important radiation bands of CO_2 and water. If the absorption of the fuel is known to be important, separate bands can be reserved for fuel,

Table 3.1: Limits of the spectral bands.

9 Band Model	1	2	3	4	5	6	7	8	9
Major Species	Soot	CO_2 H_2O, Soot	CH_4 Soot	Soot	CO_2 Soot	H_2O Soot	H_2O CH_4, Soot	Soot	Soot
ν (1/cm)	10000	3800	3400	2800	2400	2174	1429	1160	1000	50
λ (µm)	1.00	2.63	2.94	3.57	4.17	4.70	7.00	8.62	10.0	200

6 Band Model	1	2	3	4	5	6
Major Species	Soot	CO_2 H_2O, Soot	CH_4 Soot	CO_2 Soot	H_2O, CH_4, Soot	Soot

and the total number of bands is increased to nine ($N = 9$). For simplicity, the fuel is assumed to be CH_4. The limits of the bands are shown in Table 3.1.

For the calculation of the gray or band-mean absorption coefficients, κ_n, a narrow-band model, Rad-Cal [39], has been implemented in FDS. At the start of a simulation the absorption coefficient(s) are tabulated as a function of mixture fraction and temperature. During the simulation the local absorption coefficient is found by table-lookup.

In calculations of limited spatial resolution, the source term, I_b, in the RTE requires special treatment in the neighborhood of the flame sheet because the temperatures are smeared out over a grid cell and are thus considerably lower than one would expect in a diffusion flame. Because of its fourth-power dependence on the temperature, the source term must be modeled in those grid cells cut by the flame sheet. Elsewhere, there is greater confidence in the computed temperature, and the source term can be computed directly

$$\kappa I_b = \begin{cases} \kappa \sigma T^4 / \pi & \text{Outside flame zone} \\ \max(\chi_r \dot{q}''' / 4\pi,\ \kappa \sigma T^4 / \pi) & \text{Inside flame zone} \end{cases} \tag{3.83}$$

Here, $\dot{q}'''$ is the chemical heat release rate per unit volume and χ_r is an empirical estimate of the *local* fraction of that energy emitted as thermal radiation.[4] Near the flame in large scale calculations, neither κ nor T can be computed reliably, hence the inclusion of the empirical radiation loss term which is designed to partition the fire's heat release rate in accordance with measured values.

The boundary condition for the radiation intensity leaving a gray diffuse wall is given as

$$I_w(\mathbf{s}) = \frac{\varepsilon \sigma T_w^4}{\pi} + \frac{1 - \varepsilon}{\pi} \int_{\mathbf{s}' \cdot \mathbf{n}_w < 0} I_w(\mathbf{s}') |\mathbf{s}' \cdot \mathbf{n}_w| \, d\mathbf{s}' \tag{3.84}$$

where $I_w(\mathbf{s})$ is the intensity at the wall, ε is the emissivity, and T_w is the wall surface temperature. The radiant heat flux vector $\dot{\mathbf{q}}_r''$ is defined

$$\dot{\mathbf{q}}_r''(\mathbf{x}) = \int_{4\pi} \mathbf{s}' I(\mathbf{x}, \mathbf{s}') \, d\mathbf{s}' \tag{3.85}$$

The gas phase contribution to the radiative loss term in the energy equation is

$$-\nabla \cdot \dot{\mathbf{q}}_r''(\mathbf{x})(\text{gas}) = \kappa(\mathbf{x}) \left[U(\mathbf{x}) - 4\pi I_b(\mathbf{x}) \right] \quad ; \quad U(\mathbf{x}) = \int_{4\pi} I(\mathbf{x}, \mathbf{s}') \, d\mathbf{s}' \tag{3.86}$$

In words, the net radiant energy gained by a grid cell is the difference between that which is absorbed and that which is emitted.

---

[4]The radiative fraction, χ_r, is a useful quantity in fire science. Usually, it is understood to be the fraction of the total heat release rate that takes the form of thermal radiation. For most combustibles, χ_r is between 0.3 and 0.4. However, in Eq. (3.83), χ_r is interpreted as the fraction of energy radiated from the combustion region. For a small fire ($D < 1$ m), the local χ_r is approximately equal to its global counterpart. However, as the fire increases in size, the global value will typically decrease due to a net re-absorption of the thermal radiation by the increasing smoke mantle.

3.4 Solid Phase Model

FDS assumes that solid obstructions consist of multiple layers, with each layer composed of multiple material components that can undergo multiple thermal degradation reactions. Each reaction forms a combination of solid residue (*i.e.* another material component), water vapor, and/or fuel vapor. Heat conduction is assumed only in the direction normal to the surface. This section describes the single mass and energy conservation equation for solid materials, plus the various coefficients, source terms, and boundary conditions.

3.4.1 The Heat Conduction Equation for a Solid

A one-dimensional heat conduction equation for the solid phase temperature $T_s(x,t)$ is applied in the direction x pointing into the solid (the point $x = 0$ represents the surface)[5]

$$\rho_s c_s \frac{\partial T_s}{\partial t} = \frac{\partial}{\partial x} k_s \frac{\partial T_s}{\partial x} + \dot{q}_s''' \tag{3.88}$$

Section 3.4.2 describes the component-averaged material properties, k_s and $\rho_s c_s$. The source term, $\dot{q}_s'''$, consists of chemical reactions and radiative absorption:

$$\dot{q}_s''' = \dot{q}_{s,c}''' + \dot{q}_{s,r}''' \tag{3.89}$$

Section 3.4.3 describes the term $\dot{q}_{s,c}'''$, which is essentially the heat production (loss) rate given by the pyrolysis models for different types of solid and liquid fuels. Section 3.4.4 describes the term $\dot{q}_{s,r}'''$, the radiative absorption and emission in depth. Section 3.4.5 describes the convective heat transfer to the solid surface. Finally, Section 3.4.6 describes how the radiative and convective heat fluxes are applied as boundary conditions for Eq. (3.88).

3.4.2 Component-Averaged Thermal Properties

The conductivity and volumetric heat capacity of the solid are defined

$$k_s = \sum_{\alpha=1}^{N_m} X_\alpha \, k_{s,\alpha} \quad ; \quad \rho_s c_s = \sum_{\alpha=1}^{N_m} \rho_{s,\alpha} \, c_{s,\alpha} \tag{3.90}$$

N_m is the number of material components forming the solid. $\rho_{s,\alpha}$ is the *component density*

$$\rho_{s,\alpha} = \rho_s Y_\alpha \tag{3.91}$$

where ρ_s is the density of the composite material and Y_α is the mass fraction of material component α. The solid density is the sum of the component densities

$$\rho_s = \sum_{\alpha=1}^{N_m} \rho_{s,\alpha} \tag{3.92}$$

---

[5]In cylindrical and spherical coordinates, the heat conduction equation is written

$$\rho_s c_s \frac{\partial T_s}{\partial t} = \frac{1}{r} \frac{\partial}{\partial r} \left(r k_s \frac{\partial T_s}{\partial r} \right) + \dot{q}_s''' \quad ; \quad \rho_s c_s \frac{\partial T_s}{\partial t} = \frac{1}{r^2} \frac{\partial}{\partial r} \left(r^2 k_s \frac{\partial T_s}{\partial r} \right) + \dot{q}_s''' \tag{3.87}$$

FDS offers the user these options, with the assumption that the obstruction is not actually recti-linear, but rather cylindrical or spherical in shape. This option is useful in describing the behavior of small, complicated "targets" like cables or heat detection devices.

X_α is the volume fraction of component α

$$X_\alpha = \frac{\rho_{s,\alpha}}{\rho_\alpha} \bigg/ \sum_{\alpha'=1}^{N_m} \frac{\rho_{s,\alpha'}}{\rho_{\alpha'}} \tag{3.93}$$

where ρ_α is the density of material α in its pure form. Multi-component solids are defined by specifying the mass fractions, Y_α, and densities, ρ_α, of the individual components of the composite.

3.4.3 Pyrolysis Models

This section describes how solid phase reactions and the chemical source term in the solid phase heat conduction equation, $\dot{q}_{s,c}'''$, are modeled. This is what is commonly referred to as the "pyrolysis model," but it actually can represent any number of reactive processes, including evaporation, charring, and internal heating.

Specified Heat Release Rate

Often the intent of a fire simulation is merely to predict the transport of smoke and heat from a *specified* fire. In other words, the heat release rate is a user input, not something the model predicts. In these instances, the desired HRR is translated into a mass flux for fuel at a given solid surface, which can be thought of as the surface of a burner:

$$\dot{m}_f'' = \frac{f(t)\, \dot{q}_{user}''}{\Delta H} \tag{3.94}$$

Usually, the user specifies a desired heat release rate per unit area, $\dot{q}_{user}''$, plus a time ramp, $f(t)$, and the mass loss rate is computed accordingly.

Solid Fuels

Solids can undergo simultaneous reactions under the following assumptions:

- instantaneous release of volatiles from solid to the gas phase,
- local thermal equilibrium between the solid and the volatiles,
- no condensation of gaseous products, and
- no porosity effects[6]

Each material component may undergo several competing reactions, and each of these reactions may produce some other solid component (residue) and gaseous volatiles according to the yield coefficients ν_s and $\nu_{g,\gamma}$, respectively. These coefficients should usually satisfy $\nu_s + \sum_\gamma \nu_{g,\gamma} = 1$, but smaller yields may also be used to take into account the gaseous products that are not explicitly included in the simulation.

Consider material component α that undergoes $N_{r,\alpha}$ separate reactions. We will use the index β to represent one of these reactions:

$$\text{Material}_\alpha \rightarrow \nu_{s,\alpha\beta}\, \text{Residue}_{\alpha\beta} + \nu_{g,\alpha\beta,w}\, H_2O + \nu_{g,\alpha\beta,f}\, HC \tag{3.95}$$
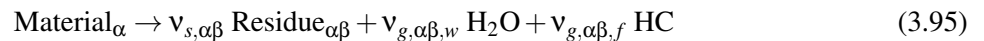
In this his particular reaction, condenced phase residue, water vapor and hydrocarbon fuel are produced.

---

[6]Although porosity effects are not explicitly included in the model, it is possible to account for it because the volume fractions defined by Eq. (3.93) need not sum to unity, in which case the thermal conductivity and absorption coefficient are effectively reduced.

The local density of material component α evolves in time according to the solid phase species conservation equation

$$\frac{\partial}{\partial t}\left(\frac{\rho_{s,\alpha}}{\rho_{s0}}\right) = -\sum_{\beta=1}^{N_{r,\alpha}} r_{\alpha\beta} + S_\alpha \tag{3.96}$$

which says that the mass of conponent α is consumed by the solid phase reactions $r_{\alpha\beta}$ and produced by other reactions. $r_{\alpha\beta}$ is the rate of reaction β in units (1/s) and ρ_{s0} is the initial density of the material layer. S_α is the production rate of material component α as a result of the reactions of the other components. The reaction rates are functions of local mass concentration and temperature, and calculated as a combination of Arrhenius and power functions:

$$r_{\alpha\beta} = \left(\frac{\rho_{s,\alpha}}{\rho_{s0}}\right)^{n_{s,\alpha\beta}} A_{\alpha\beta} \exp\left(-\frac{E_{\alpha\beta}}{RT_s}\right) \max\left[0, T_s - T_{thr,\alpha\beta}\right]^{n_{t,\alpha\beta}} \tag{3.97}$$

where $T_{thr,\alpha\beta}$ is a threshold temperature that can be used to dictate that the reaction must not occur below a user-specified temperature. By default, the term is deactivated ($T_{thr,\alpha\beta} = 0$ K).

The production term S_α is the sum over all the reactions where the solid residue is material α

$$S_\alpha = \sum_{\alpha'=1}^{N_m} \sum_{\beta=1}^{N_{r,\alpha'}} \nu_{s,\alpha'\beta}\, r_{\alpha'\beta} \qquad (\text{where Residue}_{\alpha'\beta} = \text{Material}_\alpha) \tag{3.98}$$

The volumetric production rate of each gaseous volatile is

$$\dot{m}_\gamma''' = \rho_{s0} \sum_{\alpha=1}^{N_m} \sum_{\beta=1}^{N_{r,\alpha}} \nu_{g,\alpha\beta,\gamma}\, r_{\alpha\beta} \tag{3.99}$$

It is assumed that the gases are transported instantaneously to the surface, where the mass fluxes are given by: [7]

$$\dot{m}_\gamma'' = \int_0^L \dot{m}_\gamma'''(x)\, dx \tag{3.101}$$

where L is the thickness of the surface. The chemical source term of the heat conduction equation consists of the heats of reaction

$$\dot{q}_{s,c}'''(x) = -\rho_{s0} \sum_{\alpha=1}^{N_m} \sum_{\beta=1}^{N_{r,\alpha}} r_{\alpha\beta}(x) H_{r,\alpha\beta} \tag{3.102}$$

Liquid Fuels

The rate at which liquid fuel evaporates when burning is a function of the liquid temperature and the concentration of fuel vapor above the pool surface. According to the Clausius-Clapeyron relation, the volume fraction of the fuel vapor above the surface is a function of the liquid boiling temperature

$$X_f = \exp\left[-\frac{h_v W_f}{\mathcal{R}}\left(\frac{1}{T_s} - \frac{1}{T_b}\right)\right] \tag{3.103}$$

---

[7]In cylindrical and spherical coordinates, the mass fluxes are

$$\dot{m}_\gamma'' = \frac{1}{R}\int_0^R \dot{m}_\gamma'''(x)\, r\, dr \;\; ; \;\; \dot{m}_\gamma'' = \frac{1}{R^2}\int_0^R \dot{m}_\gamma'''(x)\, r^2\, dr \tag{3.100}$$

where h_v is the heat of vaporization, W_f is the molecular weight, T_s is the surface temperature, and T_b is the boiling temperature of the fuel [40].

In the beginning of the simulation, an initial guess is made for the fuel vapor mass flux

$$\dot{m}_i'' = \frac{\dot{V}_i'' W_f}{\mathcal{R} T_a / p_0} \tag{3.104}$$

where $\dot{V}_i''$ is the initial vapor volume flux, defined by the user (default $\dot{V}_i'' = 5 \cdot 10^{-4}$ m^3/(sm^2)). During the simulation, the evaporation mass flux is updated based on the difference between current close-to-the-surface volume fraction of fuel vapor and the equilibrium value given by Eq. 3.103.

For simplicity, the liquid fuel itself is treated like a thermally-thick solid for the purpose of computing the heat conduction. There is no computation of the convection of the liquid within the pool.

3.4.4 Radiation Heat Transfer to Solids

If it is assumed that the thermal radiation from the surrounding gases is absorbed within an infinitely thin layer at the surface of the solid obstruction, then the net radiative heat flux is the sum of incoming and outgoing components, $\dot{q}_r'' = \dot{q}_{r,in}'' - \dot{q}_{r,out}''$, where:

$$\dot{q}_{r,in}'' = \varepsilon \int_{\mathbf{s}' \cdot \mathbf{n}_w < 0} I_w(\mathbf{s}') \left| \mathbf{s}' \cdot \mathbf{n}_w \right| d\Omega \tag{3.105}$$

$$\dot{q}_{r,out}'' = \varepsilon \sigma T_w^4 \tag{3.106}$$

However, many common materials do not have infinite optical thickness. Rather, the radiation penetrates the material to some finite depth. The radiative transport within the solid (or liquid) can be described as a source term in Eq. (3.88). A "two-flux" model based on the Schuster-Schwarzschild approximation [19] assumes the radiative intensity is constant inside the "forward" and "backward" hemispheres. The transport equation for the intensity in the "forward" direction is

$$\frac{1}{2} \frac{dI^+(x)}{dx} = \kappa_s \left(I_b - I^+(x) \right) \tag{3.107}$$

where x is the distance from the material surface and κ_s is the absorption coefficient

$$\kappa_s = \sum_{\alpha=1}^{N_m} X_\alpha \, \kappa_{s,\alpha} \tag{3.108}$$

A corresponding formula can be given for the "backward" direction. Multiplying Eq. 3.107 by π gives us the "forward" radiative heat flux into the solid

$$\frac{1}{2} \frac{d\dot{q}_r^+(x)}{dx} = \kappa_s \left(\sigma T_s^4 - \dot{q}_r^+(x) \right) \tag{3.109}$$

The radiative source term in the heat conduction equation is a sum of the "forward" and "backward" flux gradients

$$\dot{q}_{s,r}'''(x) = \frac{d\dot{q}_r^+(x)}{dx} + \frac{d\dot{q}_r^-(x)}{dx} \tag{3.110}$$

The boundary condition for Eq. 3.109 at the solid (or liquid) surface is given by

$$\dot{q}_r^+(0) = \dot{q}_{r,in}'' + (1 - \varepsilon) \dot{q}_r^-(0) \tag{3.111}$$

where $\dot{q}_r^-(0)$ is the "backward" radiative heat flux at the surface. In this formulation, the surface emissivity and the internal absorption are assumed to be independent properties of the material.

3.4.5 Convective Heat Transfer to Solids

The calculation of the convective heat flux depends on whether one is performing a Direct Numerical Simulation (DNS) or a Large Eddy Simulation (LES). In a DNS calculation, the convective heat flux to a solid surface $\dot{q}_c''$ is obtained directly from the gas temperature gradient at the boundary

$$\dot{q}_c'' = -k\,\frac{\partial T}{\partial n} \tag{3.112}$$

where n is the spatial coordinate pointing into the solid. In an LES calculation, the convective heat flux to the surface is obtained from a combination of natural and forced convection correlations

$$\dot{q}_c'' = h\,\Delta T \quad \text{W/m}^2 \quad ; \quad h = \max\left[C\,|\Delta T|^{\frac{1}{3}} \,,\, \frac{k}{L}\,0.037\,\text{Re}^{\frac{4}{5}}\,\text{Pr}^{\frac{1}{3}} \right] \quad \text{W/m}^2\text{/K} \tag{3.113}$$

where ΔT is the difference between the wall and the gas temperature (taken at the center of the grid cell abutting the wall), C is the coefficient for natural convection (1.52 for a horizontal surface and 1.31 for a vertical surface) [17], L is a characteristic length related to the size of the physical obstruction, k is the thermal conductivity of the gas, and the Reynolds Re and Prandtl Pr numbers are based on the gas flowing past the obstruction. Since the Reynolds number is proportional to the characteristic length, L, the heat transfer coefficient is weakly related to L. For this reason, L is taken to be 1 m for most calculations.

3.4.6 Boundary Conditions

The boundary condition on the front surface is

$$-k_s\,\frac{\partial T_s}{\partial x}(0,t) = \dot{q}_c'' + \dot{q}_r'' \tag{3.114}$$

If the internal radiation is solved for a solid, the radiation boundary condition $\dot{q}_r''$ is not used.

On the back surface, two possible boundary condition types may be specified by the user. (1) If the back surface is assumed to be open either to an ambient void or to another part of the computational domain, the back side boundary condition is similar to that of the front side. (2) If the back side is assumed to be perfectly insulated, an adiabatic boundary condition is used

$$k_s\,\frac{\partial T_s}{\partial x} = 0 \tag{3.115}$$

3.5 Fire Detection Devices

FDS predicts the thermal environment resulting from a fire, but it relies on various empirical models that describe the activation of various fire detection devices. These models are described in this section.

3.5.1 Sprinkler Activation

The temperature of the sensing element (or "link") of an automatic fire sprinkler is estimated from the differential equation put forth by Heskestad and Bill [41], with the addition of a term to account for the cooling of the link by water droplets in the gas stream from previously activated sprinklers

$$\frac{dT_l}{dt} = \frac{\sqrt{|\mathbf{u}|}}{\text{RTI}}(T_g - T_l) - \frac{C}{\text{RTI}}(T_l - T_m) - \frac{C_2}{\text{RTI}}\beta|\mathbf{u}| \tag{3.116}$$

Here T_l is the link temperature, T_g is the gas temperature in the neighborhood of the link, T_m is the temperature of the sprinkler mount (assumed ambient), and β is the volume fraction of (liquid) water in the gas stream. The sensitivity of the detector is characterized by the value of RTI. The amount of heat conducted away from the link by the mount is indicated by the "C-Factor", C. The RTI and C-Factor are determined experimentally. The constant C_2 has been empirically determined by DiMarzo and co-workers [42, 43, 44] to be 6×10^6 K/(m/s)$^{\frac{1}{2}}$, and its value is relatively constant for different types of sprinklers.

The algorithm for heat detector activation is exactly the same as for sprinkler activation, except there is no accounting for conductive losses or droplet cooling. Note that neither the sprinkler nor heat detector models account for thermal radiation.

3.5.2 Heat Detectors

As far as FDS is concerned, a heat detector is just a sprinkler with no water spray. In other words, the activation of a heat detector is governed by Eq. (3.116), but with just the first term on the right hand side:

$$\frac{dT_l}{dt} = \frac{\sqrt{|\mathbf{u}|}}{\text{RTI}}(T_g - T_l) \tag{3.117}$$

Both the RTI and activation temperature are determined empirically.

3.5.3 Smoke Detectors

An informative discussion of the issues associated with smoke detection can be found in the SFPE Handbook chapter "Design of Detection Systems," by Schifiliti, Meacham and Custer [20]. The authors point out that the difficulty in modeling smoke detector activation stems from a number of issues: (1) the production and transport of smoke in the early stage of a fire are not well-understood, (2) detectors often use complex response algorithms rather than simple threshold or rate-of-change criteria, (3) detectors can be sensitive to smoke particle number density, size distribution, refractive index, composition, *etc.*, and (4) most computer models, including FDS, do not provide detailed descriptions of the smoke besides its bulk transport. This last point is the most important. At best, in its present form, FDS can only provide to an activation algorithm the velocity and smoke concentration of the ceiling jet flowing past the detector. Regardless of the detailed mechanism within the device, any activation model included within FDS can only account for the entry resistance of the smoke due to the geometry of the detector. Issues related to the effectiveness of ionization or photoelectric detectors cannot be addressed by FDS.

Consider the simple idealization of a "spot-type" smoke detector. A disk-shaped cover lined with a fine mesh screen forms the external housing of the device, which is usually mounted to the ceiling. Somewhere

within the device is a relatively small sensing chamber where the smoke is actually detected in some way. A simple model of this device has been proposed by Heskestad [20]. He suggested that the mass fraction of smoke in the sensing chamber of the detector Y_c lags behind the mass fraction in the external free stream Y_e by a time period $\delta t = L/u$, where u is the free stream velocity and L is a length characteristic of the detector geometry. The change in the mass fraction of smoke in the sensing chamber can be found by solving the following equation:

$$\frac{dY_c}{dt} = \frac{Y_e(t) - Y_c(t)}{L/\mathbf{u}} \tag{3.118}$$

The detector activates when Y_c rises above a detector-specific threshold.

A more detailed model of smoke detection involving two filling times rather than one has also been proposed. Smoke passing into the sensing chamber must first pass through the exterior housing, then it must pass through a series of baffles before arriving at the sensing chamber. There is a time lag associated with the passing of the smoke through the housing and also the entry of the smoke into the sensing chamber. Let δt_e be the characteristic filling time of the entire volume enclosed by the external housing. Let δt_c be the characteristic filling time of the sensing chamber. Cleary *et al.* [45] suggested that each characteristic filling time is a function of the free-stream velocity u outside the detector

$$\delta t_e = \alpha_e u^{\beta_e} \quad ; \quad \delta t_c = \alpha_c u^{\beta_c} \tag{3.119}$$

The α's and β's are empirical constants related to the specific detector geometry The change in the mass fraction of smoke in the sensing chamber Y_c can be found by solving the following equation:

$$\frac{dY_c}{dt} = \frac{Y_e(t - \delta t_e) - Y_c(t)}{\delta t_c} \tag{3.120}$$

where Y_e is the mass fraction of smoke outside of the detector in the free-stream. A simple interpretation of the equation is that the concentration of the smoke that enters the sensing chamber at time t is that of the free-stream at time $t - \delta t_e$.

An analytical solution for Eq. (3.120) can be found, but it is more convenient to simply integrate it numerically as is done for sprinklers and heat detectors. Then, the predicted mass fraction of smoke in the sensing chamber, $Y_c(t)$, can be converted into an expression for the percent obscuration per unit length by computing:

$$\left(1 - e^{-\kappa \rho Y_c l}\right) \times 100 \tag{3.121}$$

where κ is the specific extinction coefficient, ρ is the density of the external gases in the ceiling jet, and l is the preferred unit of length (typically 1 m or 1 ft). For most flaming fuels, a suggested value for κ is 8700 m^2/kg $\pm$ 1100 m^2/kg at a wavelength of 633 nm [46].

The SFPE Handbook has references to various works on smoke detection and suggested values for the characteristic length L. FDS includes the one parameter Heskestad model as a special case of the four parameter Cleary model. For the Cleary model, one must set α_e, β_e, α_c, and β_c, whereas for the Heskestad model only $L = \alpha_c$ needs to be specified. Eq. (3.120) is still used, with $\alpha_e = 0$ and $\beta_e = \beta_c = -1$. Proponents of the four-parameter model claim that the two filling times are needed to better capture the behavior of detectors in a very slow free-stream ($u < 0.5$ m/s). Rather than declaring one model better than another, the algorithm included in FDS allows the user to pick these various parameters, and in so doing, pick whichever model the user feels is appropriate [47].

Additionally, FDS can model the behavior of beam and aspiration smoke detectors. For a beam detector the user specifies the emitter and receiver positions and the total obscuration at which the detector will alarm. FDS will then integrate the obscuration over the path length using the predicted soot concentration in each grid cell along the path. For an aspiration detector the user specifies the sampling locations, the flow rate at

each location, the transport time from each sampling point to the detector, the flow rate of any bypass flow, and the total obscuration at which the detector will alarm. FDS will compute that soot concentration at the detector by weighting the predicted soot concentrations at the sampling locations with their flow rates after applying the appropriate time delay.

3.6 Liquid Sprays

There are several uses for liquid sprays within FDS, most notably for sprinklers, but also for liquid fuel sprays. The basic physics is the same in each case, but the liquid properties are different. Also, simulating the effects of a sprinkler spray involves a number of elements beyond just activation: computing the droplet trajectories and tracking the water as it drips onto the burning surface.

3.6.1 Droplet Size Distribution

A spray consists of a sampled set of spherical droplets. The size distribution is expressed in terms of its Cumulative Volume Fraction (CVF), a function that relates the fraction of the liquid volume (mass) transported by droplets less than a given diameter. Researchers at Factory Mutual have suggested that the CVF for a sprinkler may be represented by a combination of log-normal and Rosin-Rammler distributions [48]

$$
F(d) = \begin{cases} \frac{1}{\sqrt{2\pi}} \int_0^d \frac{1}{\sigma d'} e^{-\frac{[\ln(d'/d_m)]^2}{2\sigma^2}} \, \mathrm{d}d' & (d \le d_m) \\ 1 - e^{-0.693\left(\frac{d}{d_m}\right)^\gamma} & (d_m < d) \end{cases}
\tag{3.122}
$$

where d_m is the median droplet diameter (*i.e.* half the mass is carried by droplets with diameters of d_m or less), and γ and σ are empirical constants equal to about 2.4 and 0.6, respectively.[8] The median droplet diameter is a function of the sprinkler orifice diameter, operating pressure, and geometry. Research at Factory Mutual has yielded a correlation for the median droplet diameter [49]

$$
\frac{d_m}{D} \propto \mathrm{We}^{-\frac{1}{3}}
\tag{3.123}
$$

where D is the orifice diameter of the sprinkler. The Weber number, the ratio of inertial forces to surface tension forces, is given by

$$
\mathrm{We} = \frac{\rho_d u_d^2 D}{\sigma_d}
\tag{3.124}
$$

where ρ_d is the density of liquid, u_d is the discharge velocity, and σ_d is the liquid surface tension (72.8×10^{-3} N/m at 20 °C for water). The discharge velocity can be computed from the mass flow rate, a function of the sprinkler's operating pressure and orifice coefficient known as the "K-Factor." FM reports that the constant of proportionality in Eq. (3.123) appears to be independent of flow rate and operating pressure. Three different sprinklers were tested in their study with orifice diameters of 16.3 mm, 13.5 mm, 12.7 mm and the constants were approximately 4.3, 2.9, 2.3, respectively. The strike plates of the two smaller sprinklers were notched, while that of the largest sprinkler was not [49].

In real sprinkler systems, the operating pressure is affected by the number of open nozzles. Typically, the pressure in the piping is high when the first sprinkler activates, and decreases when more and more sprinkler heads are activated. The pipe pressure has an effect on flow rate, droplet velocity and droplet size distribution. FDS tries not to predict the variation of pipe pressure; it should be specified by the user; but the following dependencies are used to update the droplet boundary conditions for mass flow $\dot{m}$, droplet speed u_d and median diameter d_m

$$
\begin{align}
\dot{m} &\propto \sqrt{p} \tag{3.125} \\
u_d &\propto \sqrt{p} \tag{3.126} \\
d_m &\propto p^{-1/3} \tag{3.127}
\end{align}
$$

---

[8]The Rosin-Rammler and log-normal distributions are smoothly joined if $\sigma = 2/(\sqrt{2\pi}(\ln 2)\gamma) = 1.15/\gamma$.
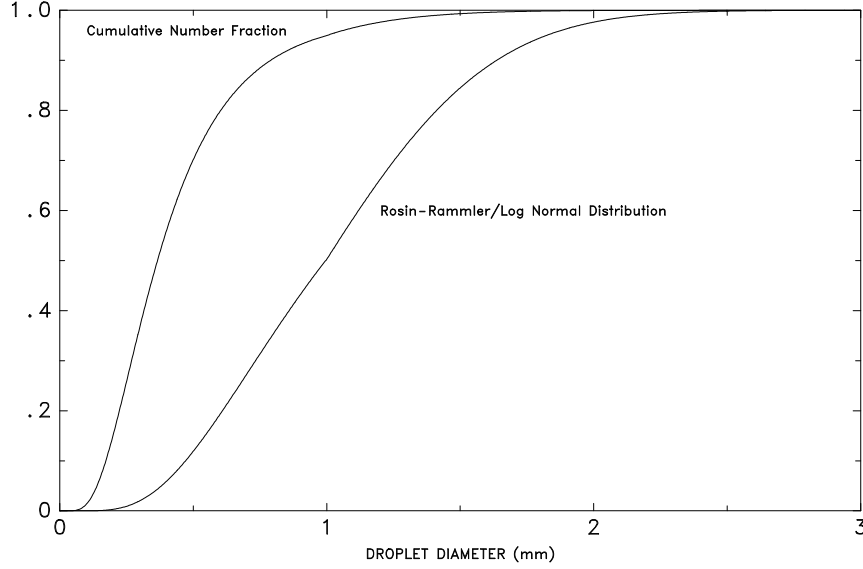
Figure 3.5: Cumulative Volume Fraction and Cumulative Number Fraction functions of the droplet size distribution from a typical industrial-scale sprinkler. The median diameter d_m is 1 mm, $\sigma = 0.6$ and $\gamma = 2.4$.

In the numerical algorithm, the size of the droplets are chosen to mimic the Rosin-Rammler/log-normal distribution. A Probability Density Function (PDF) for the droplet diameter is defined

$$f(d) = \frac{F'(d)}{d^3} \bigg/ \int_0^\infty \frac{F'(d')}{d'^3}\, \mathrm{d}d' \quad ; \quad F' \equiv \frac{\mathrm{d}F}{\mathrm{d}d} \tag{3.128}$$

Droplet diameters are randomly selected by equating the Cumulative Number Fraction of the droplet distribution with a uniformly distributed random variable U

$$U(d) = \int_0^d f(d')\, \mathrm{d}d' \tag{3.129}$$

Figure 3.5 displays typical Cumulative Volume Fraction and Cumulative Number Fraction functions.

3.6.2 Droplet Transport in the Gas Phase

Every droplet from a given sprinkler or nozzle is not tracked. Instead, a sampled set of the droplets is tracked. The procedure for selecting droplet sizes is as follows: Suppose the mass flow rate of the liquid is $\dot{m}$. Suppose also that the time interval for droplet insertion into the numerical simulation is δt, and the number of droplets inserted each time interval is N. Choose N uniformly distributed random numbers between 0 and 1, call them U_i, obtain N droplet diameters d_i based on the given droplet size distribution, Eq. (3.129), and then compute a weighting constant C from the mass balance

$$\dot{m}\, \delta t = C \sum_{i=1}^{N} \frac{4}{3}\pi\rho_w \left(\frac{d_i}{2}\right)^3 \tag{3.130}$$

The mass and heat transferred from each droplet will be multiplied by the weighting factor C.

For a spray, the force term $\mathbf{f}_b$ in Eq. (3.2) represents the momentum transferred from the droplets to the gas. It is obtained by summing the force transferred from each droplet in a grid cell and dividing by the cell

43

volume

$$\mathbf{f}_b = \frac{1}{2} \frac{\sum \rho C_D \pi r_d^2 (\mathbf{u}_d - \mathbf{u}) |\mathbf{u}_d - \mathbf{u}|}{\delta x \, \delta y \, \delta z} \tag{3.131}$$

where C_D is the drag coefficient, r_d is the droplet radius, $\mathbf{u}_d$ is the velocity of the droplet, $\mathbf{u}$ is the velocity of the gas, ρ is the density of the gas, and $\delta x \, \delta y \, \delta z$ is the volume of the grid cell. The acceleration of an individual droplet is governed by the equation

$$\frac{d}{dt} (m_d \mathbf{u}_d) = m_d \mathbf{g} - \frac{1}{2} \rho \, C_D \pi r_d^2 (\mathbf{u}_d - \mathbf{u}) |\mathbf{u}_d - \mathbf{u}| \tag{3.132}$$

where m_d is the mass of the droplet. The trajectory of the droplet is governed by the equation

$$\frac{d\mathbf{x}_d}{dt} = \mathbf{u}_d \tag{3.133}$$

The drag coefficient (default based on a sphere) is a function of the local Reynolds number (based on droplet diameter)

$$C_D = \begin{cases} 24/\mathrm{Re}_d & \mathrm{Re}_d < 1 \\ 24 \left(0.85 + 0.15 \, \mathrm{Re}_d^{0.687} \right) / \mathrm{Re}_d & 1 < \mathrm{Re}_d < 1000 \\ 0.44 & 1000 < \mathrm{Re}_d \end{cases} \tag{3.134}$$

$$\mathrm{Re}_d = \frac{\rho \, |\mathbf{u}_d - \mathbf{u}| \, 2r_d}{\mu(T)} \tag{3.135}$$

where $\mu(T)$ is the dynamic viscosity of air at temperature T.

3.6.3 Droplet Transport on a Surface

When a liquid droplet hits a solid horizontal surface, it is assigned a random horizontal direction and moves at a fixed velocity until it reaches the edge, at which point it drops straight down at the same fixed velocity. This "dripping" velocity has been measured for water to be on the order of 0.5 m/s [50, 51]. While attached to a surface, the "droplet" is assumed to form a thin film of liquid that transfers heat to the solid, and heat and mass to the gas. Details are included in the next section.

3.6.4 Absorption and Scattering of Thermal Radiation by Droplets

The attenuation of thermal radiation by liquid droplets is an important consideration, especially for water mist systems [52]. Liquid droplets attenuate thermal radiation through a combination of scattering and absorption [53]. The radiation-droplet interaction must therefore be solved for both the accurate prediction of the radiation field and for the droplet energy balance.

If the gas phase absorption and emission in Eq. (3.77) are temporarily neglected for simplicity, the radiative transport equation becomes

$$\mathbf{s} \cdot \nabla I_\lambda(\mathbf{x}, \mathbf{s}) = - \left[\kappa_d(\mathbf{x}, \lambda) + \sigma_d(\mathbf{x}, \lambda) \right] I_\lambda(\mathbf{x}, \mathbf{s}) + \kappa_d(\mathbf{x}, \lambda) \, I_{b,d}(\mathbf{x}, \lambda) + \frac{\sigma_d(\mathbf{x}, \lambda)}{4\pi} \int_{4\pi} \Phi(\mathbf{s}, \mathbf{s}') \, I_\lambda(\mathbf{x}, \mathbf{s}') \, d\mathbf{s}' \tag{3.136}$$

where κ_d is the droplet absorption coefficient, σ_d is the droplet scattering coefficient and $I_{b,d}$ is the emission term of the droplets. $\Phi(\mathbf{s}, \mathbf{s}')$ is a scattering phase function that gives the scattered intensity from direction $\mathbf{s}'$ to $\mathbf{s}$. The local absorption and scattering coefficients are calculated from the local droplet number density $N(\mathbf{x})$ and mean diameter $d_m(\mathbf{x})$ as

$$\kappa_d(\mathbf{x}, \lambda) = N(\mathbf{x}) \int_0^\infty f(r, d_m(\mathbf{x})) \, C_a(r, \lambda) \, dr \tag{3.137}$$

$$\sigma_d(\mathbf{x}, \lambda) = N(\mathbf{x}) \int_0^\infty f(r, d_m(\mathbf{x})) \, C_s(r, \lambda) \, dr \tag{3.138}$$

where r is the droplet radius and C_a and C_s are absorption and scattering cross sections, respectively, given by Mie theory. The droplet number density function $f(r, d_m)$ is assumed to have the same form as the initial droplet size distribution, but a mean diameter depending on the location $\mathbf{x}$. For the numerical implementation, the above equations are written in the form

$$\kappa_d(\mathbf{x}, \lambda) = A_d(\mathbf{x}) \int_0^\infty \frac{f(r, d_m(\mathbf{x})) \, C_a(r, \lambda)}{\pi (d_m(\mathbf{x})/2)^2} \, dr \tag{3.139}$$

$$\sigma_d(\mathbf{x}, \lambda) = A_d(\mathbf{x}) \int_0^\infty \frac{f(r, d_m(\mathbf{x})) \, C_s(r, \lambda)}{\pi (d_m(\mathbf{x})/2)^2} \, dr \tag{3.140}$$

where A_d is the total cross sectional area per unit volume of the droplets. A_d is approximated as

$$A_d \approx \frac{\rho_d(\mathbf{x})}{2\rho_w d_m(\mathbf{x})/3} \tag{3.141}$$

An accurate computation of the in-scattering integral on the right hand side of Eq. (3.136) would be extremely time consuming. It is here approximated by dividing the total 4π solid angle to a "forward angle" $\delta\Omega^l$ and "ambient angle" $\delta\Omega^* = 4\pi - \delta\Omega^l$. For compatibility with the FVM solver, $\delta\Omega^l$ is set equal to the control angle given by the angular discretization. However, it is assumed to be symmetric around the center of the control angle. Within $\delta\Omega^l$ the intensity is $I_\lambda(\mathbf{x}, \mathbf{s})$ and elsewhere it is approximated as

$$U^*(\mathbf{x}, \lambda) = \frac{U(\mathbf{x}, \lambda) - \delta\Omega^l I_\lambda(\mathbf{x}, \mathbf{s})}{\delta\Omega^*} \tag{3.142}$$

where $U(\mathbf{x})$ is the total integrated intensity. The in-scattering integral can now be written as

$$\frac{\sigma_d(\mathbf{x}, \lambda)}{4\pi} \int_{4\pi} \Phi(\mathbf{s}, \mathbf{s}') \, I_\lambda(\mathbf{x}, \mathbf{s}') \, d\Omega' = \sigma_d(\mathbf{x}, \lambda) \left[\chi_f \, I_\lambda(\mathbf{x}, \mathbf{s}) + (1 - \chi_f) U^*(\mathbf{x}, \lambda) \right] \tag{3.143}$$

where $\chi_f = \chi_f(r, \lambda)$ is a fraction of the total intensity originally within the solid angle $\delta\Omega^l$ that is scattered into the same angle $\delta\Omega^l$. Defining an effective scattering coefficient section

$$\overline{\sigma_d}(\mathbf{x}, \lambda) = \frac{4\pi N(\mathbf{x})}{4\pi - \delta\Omega^l} \int_0^\infty (1 - \chi_f) \, C_s(r, \lambda) \, dr \tag{3.144}$$

the spray RTE becomes

$$\mathbf{s} \cdot \nabla I_\lambda(\mathbf{x}, \mathbf{s}) = - \left[\kappa_d(\mathbf{x}, \lambda) + \overline{\sigma_d}(\mathbf{x}, \lambda) \right] I_\lambda(\mathbf{x}, \mathbf{s}) + \kappa_d(\mathbf{x}, \lambda) \, I_{b,d}(\mathbf{x}, \lambda) + \frac{\overline{\sigma_d}(\mathbf{x}, \lambda)}{4\pi} U(\mathbf{x}, \lambda) \tag{3.145}$$

This equation can be integrated over the spectrum to get the band specific RTE's. The procedure is exactly the same as that used for the gas phase RTE. After the band integrations, the spray RTE for band n becomes

$$\mathbf{s} \cdot \nabla I_n(\mathbf{x}, \mathbf{s}) = - \left[\kappa_{d,n}(\mathbf{x}) + \overline{\sigma_{d,n}}(\mathbf{x}) \right] I_n(\mathbf{x}, \mathbf{s}) + \kappa_{d,n}(\mathbf{x}) \, I_{b,d,n}(\mathbf{x}) + \frac{\overline{\sigma_d}(\mathbf{x}, \lambda)}{4\pi} U_n(\mathbf{x}) \tag{3.146}$$

where the source function is based on the average droplet temperature within a cell. The droplet contribution to the radiative loss term is

$$-\nabla \cdot \dot{\mathbf{q}}_r''(\mathbf{x}) (\text{droplets}) = \kappa_d(\mathbf{x}) \left[U(\mathbf{x}) - 4\pi I_{b,d}(\mathbf{x}) \right] \tag{3.147}$$

For each individual droplet, the radiative heating/cooling power is computed as

$$\dot{q}_r = \frac{m_d}{\rho_d(\mathbf{x})} \kappa_d(\mathbf{x}) \left[U(\mathbf{x}) - 4\pi I_{b,d}(\mathbf{x}) \right] \tag{3.148}$$

45

where m_d is the mass of the droplet and $\rho_d(\mathbf{x})$ is the total density of droplets in the cell.

The absorption and scattering cross sections and the scattering phase function are calculated using the MieV code developed by Wiscombe [54]. Currently, the spectral data is only included for water. The values of the imaginary part of the complex refractive index (related to absorption coefficient) are taken from Ref. [55]. Value 1.33 is used for the real part (index of refraction).

Before the actual simulation, both κ_d and $\overline{\sigma}_d$ are averaged over the possible droplet radii and wavelength. A constant "radiation" temperature, T_{rad}, is used in the wavelength averaging. T_{rad} should be selected to represent a typical radiating flame temperature. A value of 1173 K is used by default. The averaged quantities, now functions of the droplet mean diameter only, are stored in one-dimensional arrays. During the simulation, the local properties are found by table look-up using the local mean droplet diameter. More details of the computation are given in Section 4.5.2.

3.6.5 Heating and Evaporation of Liquid Droplets

Liquid "droplets" are represented either as discrete airborne spheres propelled through the gas, or as rectangular blocks that collectively form a thin liquid film on solid objects. These "droplets" are still individually tracked as lagrangian particles, but the heat and mass transfer coefficients are different. In the discussion to follow, the term "droplets" will be used to describe either form.

Over the course of a time step of the gas phase solver, the droplets in a given grid cell evaporate as a function of the liquid equilibrium vapor mass fraction, Y_l, the local gas phase vapor mass fraction, Y_g, the (assumed uniform) liquid temperature, T_l, and the local gas temperature, T_g. If the droplet is attached to a surface, T_s is the solid temperature. The mass and energy transfer between the gas and the liquid can be described by the following set of equations [56]

$$\frac{dm_l}{dt} = -A\,h_m\,\rho\,(Y_l - Y_g) \tag{3.149}$$

$$m_l\,c_l\,\frac{dT_l}{dt} = A\,h\,(T_g - T_l) + A\,h_s\,(T_s - T_l) + \dot{q}_r + \frac{dm_l}{dt}\,h_v \tag{3.150}$$

Here, m_l is the mass of the liquid droplet (or that fraction of the surface film associated with the formerly airborne droplet), A is the surface area of the liquid droplet (or that fraction of the film exposed to the gas and to the wall), h_m is the mass transfer coefficient to be discussed below, ρ is the gas density, c_l is the liquid specific heat, h is the heat transfer coefficient between the liquid and the gas, h_s is the heat transfer coefficient between the liquid and the solid surface, $\dot{q}_r$ is the rate of radiative heating of the droplet, and h_v is the latent heat of vaporization of the liquid. The vapor mass fraction of the gas, Y_g, is obtained from the gas phase mass conservation equations, and the liquid equilibrium vapor mass fraction is obtained from the Clausius-Clapeyron equation

$$X_l = \exp\left[\frac{h_v\,W_l}{\mathcal{R}}\left(\frac{1}{T_b} - \frac{1}{T_l}\right)\right] \quad ; \quad Y_l = \frac{X_l}{X_l\,(1 - W_a/W_l) + W_a/W_l} \tag{3.151}$$

where X_d is the equilibrium vapor *volume* fraction, W_l is the molecular weight of the evaporated liquid, W_a is the molecular weight of air, $\mathcal{R}$ is the universal gas constant, and T_b is the boiling temperature of the liquid.

Mass and heat transfer between liquid and gas are described with analogous empirical correlations. The mass transfer coefficient, h_m, is described by the empirical relationships [18]:

$$h_m = \frac{\mathrm{Sh}\,D_{lg}}{L} \quad ; \quad \mathrm{Sh} = \begin{cases} 2 + 0.6\,\mathrm{Re}_D^{\frac{1}{2}}\,\mathrm{Sc}^{\frac{1}{3}} & \text{droplet} \\[2ex] 0.037\,\mathrm{Re}_L^{\frac{4}{5}}\,\mathrm{Sc}^{\frac{1}{3}} & \text{film} \end{cases} \tag{3.152}$$

Sh is the Sherwood number, D_{lg} is the binary diffusion coefficient between the liquid vapor and the surrounding gas (usually assumed air), L is a length scale equal to either the droplet diameter or 1 m for a surface film, Re_D is the Reynolds number of the droplet (based on the diameter, D, and the relative air-droplet velocity), Re_L is the Reynolds number based on the length scale L, and Sc is the Schmidt number (ν/D_{lg}, assumed 0.6 for all cases).

An analogous relationship exists for the heat transfer coefficient:

$$h = \frac{Nu\, k}{L} \quad ; \quad Nu = \begin{cases} 2 + 0.6\, Re_D^{\frac{1}{2}}\, Pr^{\frac{1}{3}} & \text{droplet} \\[2ex] 0.037\, Re_L^{\frac{4}{5}}\, Pr^{\frac{1}{3}} & \text{film} \end{cases} \tag{3.153}$$

Nu is the Nusselt number, k is the thermal conductivity of the gas, and Pr is the Prandtl number (assumed 0.7 for all cases).

3.6.6 Fire Suppression by Water

The previous two sections describe heat transfer from a droplet of water to a hot gas, a hot solid, or both. Although there is some uncertainty in the values of the respective heat transfer coefficients, the fundamental physics are fairly well understood. However, when the water droplets encounter burning surfaces, simple heat transfer correlations become more difficult to apply. The reason for this is that the water is not only cooling the surface and the surrounding gas, but it is also changing the pyrolysis rate of the fuel. If the surface of the fuel is planar, it is possible to characterize the decrease in the pyrolysis rate as a function of the decrease in the total heat feedback to the surface. Unfortunately, most fuels of interest in fire applications are multi-component solids with complex geometry at scales unresolvable by the computational grid.

To date, most of the work in this area has been performed at Factory Mutual. An important paper on the subject is by Yu *et al.* [57]. The authors consider dozens of rack storage commodity fires of different geometries and water application rates, and characterize the suppression rates in terms of a few global parameters. Their analysis yields an expression for the total heat release rate from a rack storage fire after sprinkler activation

$$\dot{Q} = \dot{Q}_0\, e^{-k(t-t_0)} \tag{3.154}$$

where $\dot{Q}_0$ is the total heat release rate at the time of application t_0, and k is a fuel-dependent constant. For the FMRC Standard Plastic commodity k is given as

$$k = 0.716\, \dot{m}_w'' - 0.0131 \quad s^{-1} \tag{3.155}$$

where $\dot{m}_w''$ is the flow rate of water impinging on the box tops, divided by the area of exposed surface (top and sides). It is expressed in units of $kg/m^2/s$. For the Class II commodity, k is given as

$$k = 0.536\, \dot{m}_w'' - 0.0040 \quad s^{-1} \tag{3.156}$$

Unfortunately, this analysis is based on global water flow and burning rates. Equation (3.154) accounts for both the cooling of non-burning surfaces as well as the decrease in heat release rate of burning surfaces. In the FDS model, the cooling of unburned surfaces and the reduction in the heat release rate are computed locally. Thus, it is awkward to apply a global suppression rule. However, the exponential nature of suppression by water is observed both locally and globally, thus it is assumed that the local burning rate of the fuel can be expressed in the form [50, 51]

$$\dot{m}_f''(t) = \dot{m}_{f,0}''(t)\, e^{-\int k(t)\, dt} \tag{3.157}$$

47

Here $\dot{m}''_{f,0}(t)$ is the burning rate per unit area of the fuel when no water is applied and $k(t)$ is a linear function of the local water mass per unit area, m''_w, expressed in units of kg/m²,

$$k(t) = a \, m''_w(t) \quad \mathrm{s}^{-1} \tag{3.158}$$

Note that a is an empirical constant.

Chapter 4

Numerical Method

This chapter presents a description of the numerical methods used to solve the equations of the previous chapter, with sections in roughly the same order.

4.1 Hydrodynamic Model

Each of the conservation equations emphasizes the importance of the velocity divergence and vorticity fields, as well as the close relationship between the thermally expandable fluid equations [9] and the Boussinesq equations for which the authors have developed highly efficient solution procedures [58, 59]. All spatial derivatives are approximated by second-order finite differences and the flow variables are updated in time using an explicit second-order predictor-corrector scheme.

4.1.1 Simplified Equations

Conservation of Mass

$$\frac{\partial \rho}{\partial t} + \mathbf{u} \cdot \nabla \rho = -\rho \nabla \cdot \mathbf{u} \tag{4.1}$$

Conservation of Species

$$\frac{\partial \rho Y_\alpha}{\partial t} + \mathbf{u} \cdot \nabla \rho Y_\alpha = -\rho Y_\alpha \nabla \cdot \mathbf{u} + \nabla \cdot \rho D_\alpha \nabla Y_\alpha + \dot{m}_\alpha''' \tag{4.2}$$

Conservation of Momentum

$$\frac{\partial \mathbf{u}}{\partial t} + \mathbf{u} \times \omega + \nabla \mathcal{H} = \frac{1}{\rho} \left((\rho - \rho_0)\mathbf{g} + \mathbf{f}_b + \nabla \cdot \tau_{ij} \right) \tag{4.3}$$

Pressure Equation

$$\nabla^2 \mathcal{H} = -\frac{\partial (\nabla \cdot \mathbf{u})}{\partial t} - \nabla \cdot \mathbf{F} \quad ; \quad \mathbf{F} = \mathbf{u} \times \omega - \frac{1}{\rho} \left((\rho - \rho_m)\mathbf{g} - \mathbf{f}_b - \nabla \cdot \tau_{ij} \right) \tag{4.4}$$

Equation of State

$$\overline{p}_m(z,t) = \rho T \mathcal{R} \sum_\alpha Y_\alpha / W_\alpha \tag{4.5}$$

Notice that the source terms from the energy conservation equation have been incorporated into the divergence and ultimately are involved in the mass conservation equation. The temperature is found from the density and background pressure via the equation of state.

Temporal Discretization (Single Mesh Case)

All calculations start with ambient initial conditions. At the beginning of each time step, the density, ρ^n, species mass fractions, Y_α^n, velocity, $\mathbf{u}^n$, modified pressure, $\mathcal{H}^n$, and background pressure in zone m, $\bar{p}_m^n$ are known. All other quantities can be derived from them. Note that the superscript $(n+1)_e$ refers to an estimate of the value of the quantities at the $(n+1)$st time step.

1. The thermodynamic quantities ρ, Y_α, and $\bar{p}_m$ are estimated at the next time step with an explicit Euler step. For example, the density is estimated by

$$\rho^{(n+1)_e} = \rho^n - \delta t (\mathbf{u}^n \cdot \nabla \rho^n + \rho^n \nabla \cdot \mathbf{u}^n) \tag{4.6}$$

2. The divergence $(\nabla \cdot \mathbf{u})^{(n+1)_e}$ is formed from these estimated thermodynamic quantities. The normal velocity components at boundaries that are needed to form the divergence are assumed known.

3. A Poisson equation for the pressure is solved with a direct solver

$$\nabla^2 \mathcal{H}^{(n+1)_e} = - \left[\frac{(\nabla \cdot \mathbf{u})^{(n+1)_e} - (\nabla \cdot \mathbf{u})^n}{\delta t} \right] - \nabla \cdot \mathbf{F}^n \tag{4.7}$$

   Note that the vector $\mathbf{F}$ contains the convective, diffusive and force terms of the momentum equation. These will be described in detail below.

4. The velocity is estimated at the next time step

$$\mathbf{u}^{(n+1)_e} = \mathbf{u}^n - \delta t \left(\mathbf{F}^n + \nabla \mathcal{H}^{(n+1)_e} \right) \tag{4.8}$$

   Note that the divergence of the estimated velocity field is identically equal to the estimated divergence $(\nabla \cdot \mathbf{u})^{(n+1)_e}$ that was derived from the estimated thermodynamic quantities. The time step is checked at this point to ensure that

$$\delta t \max \left(\frac{|u|}{\delta x}, \frac{|v|}{\delta y}, \frac{|w|}{\delta z} \right) < 1 \quad ; \quad 2 \, \delta t \, \nu \left(\frac{1}{\delta x^2} + \frac{1}{\delta y^2} + \frac{1}{\delta z^2} \right) < 1 \tag{4.9}$$

   If the time step is too large, it is reduced so that it satisfies both constraints and the procedure returns to the beginning of the time step. If the time step satisfies the stability criteria, the procedure continues to the corrector step. See Section 4.1.3 for more details on stability.

   This concludes the "Predictor" stage of the time step.

5. The thermodynamic quantities ρ, Y_α, and $\bar{p}_m$ are "corrected" at the next time step. For example, the density is corrected

$$\rho^{n+1} = \frac{1}{2} \left(\rho^n + \rho^{(n+1)_e} - \delta t (\mathbf{u}^{(n+1)_e} \cdot \nabla \rho^{(n+1)_e} + \rho^{(n+1)_e} \nabla \cdot \mathbf{u}^{(n+1)_e}) \right) \tag{4.10}$$

6. The corrected divergence $(\nabla \cdot \mathbf{u})^{n+1}$ is computed from the corrected thermodynamic quantities.

7. The pressure is recomputed using estimated quantities

$$\nabla^2 \mathcal{H}^{n+1} = - \left[\frac{2(\nabla \cdot \mathbf{u})^{n+1} - (\nabla \cdot \mathbf{u})^{(n+1)_e} - (\nabla \cdot \mathbf{u})^n}{\delta t} \right] - \nabla \cdot \mathbf{F}^{(n+1)_e} \tag{4.11}$$

8. The velocity is corrected

$$\mathbf{u}^{n+1} = \frac{1}{2}\left[\mathbf{u}^n + \mathbf{u}^{(n+1)e} - \delta t\left(\mathbf{F}^{(n+1)e} + \nabla\mathcal{H}^{n+1}\right)\right]$$ (4.12)

Note again that the divergence of the corrected velocity field is identically equal to the corrected divergence.

Spatial Discretization

Spatial derivatives in the governing equations are written as second-order accurate finite differences on a rectilinear grid. The overall domain is a rectangular box that is divided into rectangular grid cells. Each cell is assigned indices i, j and k representing the position of the cell in the x, y and z directions, respectively. Scalar quantities are assigned in the center of each grid cell; thus, ρ^n_{ijk} is the density at the nth time step in the center of the cell whose indices are i, j and k. Vector quantities like velocity are assigned at their appropriate cell faces. For example, u^n_{ijk} is the x-component of velocity at the positive-oriented face of the ijkth cell; $u^n_{i-1,jk}$ is defined at the negative-oriented face of the same cell.

4.1.2 The Mass Transport Equations and the Divergence

Due to the use of the low Mach number approximation, the mass and energy equations are combined through the divergence. The divergence of the flow field contains many of the fire-specific source terms described above.

Discretizing the Convective and Diffusive Transport Terms

The density at the center of the ijkth cell is updated in time with the following predictor-corrector scheme. In the predictor step, the density at the $(n+1)$st time level is estimated based on information at the nth level

$$\frac{\rho_{ijk}^{(n+1)e} - \rho_{ijk}^n}{\delta t} + (\mathbf{u} \cdot \nabla \rho)_{ijk}^n = -\rho_{ijk}^n (\nabla \cdot \mathbf{u})_{ijk}^n \tag{4.13}$$

Following the prediction of the velocity and background pressure at the $(n+1)$st time level, the density is corrected

$$\frac{\rho_{ijk}^{(n+1)} - \frac{1}{2}\left(\rho_{ijk}^n + \rho_{ijk}^{(n+1)e}\right)}{\frac{1}{2}\delta t} + (\mathbf{u} \cdot \nabla \rho)_{ijk}^{(n+1)e} = -\rho_{ijk}^{(n+1)e} (\nabla \cdot \mathbf{u})_{ijk}^{(n+1)e} \tag{4.14}$$

The species conservation equations are differenced the same way, with the addition of diffusion and source terms:

$$\frac{(\rho Y_\alpha)_{ijk}^{(n+1)e} - (\rho Y_\alpha)_{ijk}^n}{\delta t} + \cdots = \cdots + (\nabla \cdot \rho D_\alpha \nabla Y_\alpha)_{ijk}^n + \dot{m}_{\alpha,ijk}''' \tag{4.15}$$

at the predictor step, and

$$\frac{(\rho Y_\alpha)_{ijk}^{(n+1)} - \frac{1}{2}\left((\rho Y_\alpha)_{ijk}^n + (\rho Y_\alpha)_{ijk}^{(n+1)e}\right)}{\frac{1}{2}\delta t} + \cdots = \cdots + (\nabla \cdot \rho D_\alpha \nabla Y_\alpha)_{ijk}^{(n+1)e} + \dot{m}_{\alpha,ijk}''' \tag{4.16}$$

at the corrector step.

The convective terms are written as upwind-biased differences in the predictor step and downwind-biased differences in the corrector step [60]. In the definition to follow, the symbol $\pm$ means $+$ in the predictor step and $-$ in the corrector step. The opposite is true for $\mp$.

$$
\begin{aligned}
(\mathbf{u} \cdot \nabla \rho)_{ijk} \equiv{}& \frac{1 \mp \varepsilon_u}{2} u_{ijk} \frac{\rho_{i+1,jk} - \rho_{ijk}}{\delta x} + \frac{1 \pm \varepsilon_u}{2} u_{i-1,jk} \frac{\rho_{ijk} - \rho_{i-1,jk}}{\delta x} + \\
& \frac{1 \mp \varepsilon_v}{2} v_{ijk} \frac{\rho_{i,j+1,k} - \rho_{ijk}}{\delta y} + \frac{1 \pm \varepsilon_v}{2} v_{i,j-1,k} \frac{\rho_{ijk} - \rho_{i,j-1,k}}{\delta y} + \\
& \frac{1 \mp \varepsilon_w}{2} w_{ijk} \frac{\rho_{ij,k+1} - \rho_{ijk}}{\delta z} + \frac{1 \pm \varepsilon_w}{2} w_{ij,k-1} \frac{\rho_{ijk} - \rho_{ij,k-1}}{\delta z}
\end{aligned} \tag{4.17}
$$

The convective term in the species transport equation, $(\mathbf{u} \cdot \nabla \rho Y_\alpha)_{ijk}$ is differenced the exact same way. Note that without the inclusion of the ε's, these are simple central difference approximations. The ε's are local Courant numbers, $\varepsilon_u = u\delta t/\delta x$, $\varepsilon_v = v\delta t/\delta y$, and $\varepsilon_w = w\delta t/\delta z$, where the velocity components are those that immediately follow. Their role is to bias the differencing upwind at the predictor step. Where the local Courant number is near unity, the difference becomes nearly fully upwinded. Where the local Courant number is much less than unity, the differencing is more centralized.

Flux Correction

The second-order finite-differencing scheme used in FDS cannot fully resolve sharp gradients on a relatively coarse grid. Instead, steep gradients cause local *over-shoots* and *under-shoots* of quantities like temperature, density and species mass fraction. For mass fraction in particular, this can result in a solution where the mass fraction exceeds its permissible limits (*i.e.* the numerical method transports into or out of a grid cell more mass than is physically possible). The overall numerical scheme is still mass conserving, but non-physical in regions of high gradients. This problem can be reduced, but not eliminated, by using higher order numerical methods. These methods are, however, more expensive. Another solution is to perform a flux transport correction. This involves examining the solution and locating regions where a non-physical solution exists and then redistributing mass to correct it. Typically this results in some increased numerical diffusion; however, this is partially mitigated since at any one time step, the correction is applied to a small number of cells.

The flux correction scheme is performed in both the predictor and corrector steps after updating the species mass fractions, Y_α. For each species, two loops are performed over each computational mesh. The first loop searches for and corrects under-shoots, and the second loop searches for and corrects over-shoots. An under-shoot occurs if the mass fraction of a species is less than its permissible minimum, typically 0, or if there was an outflux of that species in the prior time step, $\nabla \rho Y_{\alpha,ijk} < 0$, and the new species mass fraction is less than all of its surrounding cells. An over-shoot occurs if the mass fraction of a species is greater than its permissible maximum, or if there was an influx of that species in the prior time step, $\nabla \rho Y_{\alpha,ijk} > 0$, and the new species mass fraction is greater than all of its surrounding cells. In each loop a temporary array is used to store the corrected values which are then applied globally at the end of each loop. Using a temporary array rather than a cell by cell immediate correction ensures that cells requiring correction are not bypassed due to the sweep direction of the loop. Under-shoots are corrected first because in a typical mixture fraction computation it is more likely to have an under-shoot with a value less than the absolute minimum for the species than it is for an over-shoot to exceed the absolute maximum for the species.

Discretizing the Divergence

The divergence (see Eq. (3.14)) in the *m*th pressure zone in both the predictor and corrector step is discretized

$$(\nabla \cdot \mathbf{u})_{ijk} = \frac{\mathcal{R}}{\overline{W} c_p \overline{p}_m} \left(\dot{q}'''_{ijk} + (\nabla \cdot k \nabla T)_{ijk} + \ldots \right) + \frac{1}{p_n} \left(\frac{\mathcal{R}}{\overline{W} c_p} - 1 \right) \left(\frac{\partial \overline{p}_m}{\partial t} - w_{ijk} \rho_{0,k} g \right) \tag{4.18}$$

The thermal and material diffusion terms are pure central differences, with no upwind or downwind bias, thus they are differenced the same way in both the predictor and corrector steps. For example, the thermal conduction term is differenced as follows:

$$
\begin{aligned}
(\nabla \cdot k \nabla T)_{ijk} = {} & \frac{1}{\delta x} \left[k_{i+\frac{1}{2},jk} \frac{T_{i+1,jk} - T_{ijk}}{\delta x} - k_{i-\frac{1}{2},jk} \frac{T_{ijk} - T_{i-1,jk}}{\delta x} \right] + \\
& \frac{1}{\delta y} \left[k_{i,j+\frac{1}{2},k} \frac{T_{i,j+1,k} - T_{ijk}}{\delta y} - k_{i,j-\frac{1}{2},k} \frac{T_{ijk} - T_{i,j-1,k}}{\delta y} \right] + \\
& \frac{1}{\delta z} \left[k_{ij,k+\frac{1}{2}} \frac{T_{ij,k+1} - T_{ijk}}{\delta z} - k_{ij,k-\frac{1}{2}} \frac{T_{ijk} - T_{ij,k-1}}{\delta z} \right]
\end{aligned}
\tag{4.19}
$$

The temperature is extracted from the density via the equation of state

$$T_{ijk} = \frac{\overline{p}_m}{\rho_{ijk} \mathcal{R} \sum_{l=0}^{N_s} (Y_{\alpha,ijk}/W_\alpha)} \tag{4.20}$$

53

Because only species 1 through N_s are explicitly computed, the summation is rewritten

$$\overline{W} \equiv \sum_{\alpha=0}^{N_s} \frac{Y_{\alpha,ijk}}{W_\alpha} = \frac{1}{W_0} + \sum_{\alpha=1}^{N_s} \left(\frac{1}{W_\alpha} - \frac{1}{W_0} \right) Y_\alpha \tag{4.21}$$

In isothermal calculations involving multiple species, the density can be extracted from the average molecular weight

$$\rho_{ijk} = \frac{p_m}{T_\infty \mathcal{R} \overline{W}} = \frac{W_0 \, p_m}{T_\infty \mathcal{R}} + \sum_{\alpha=1}^{N_s} \left(1 - \frac{W_0}{W_\alpha} \right) (\rho Y_\alpha)_{ijk} \tag{4.22}$$

Enthalpy and Specific Heat

Enthalpy, h, and specific heat, c_p are computed by doing a mass weighted average of the values for h or c_p for the individual species present. The species values are obtained by table lookup using the nearest integer to the local temperature. Values for h and c_p were obtained from the NIST-JANAF tables [61].

Background Pressure Changes

The divergence of the flow, as defined by the equation of state, is written in compact notation as follows:

$$\nabla \cdot \mathbf{u} = \mathcal{D} - \mathcal{P} \frac{\partial \overline{p}_m}{\partial t} \tag{4.23}$$

The terms $\mathcal{D}$ and $\mathcal{P}$ are defined by Eqs. (3.16) and (3.15), respectively. The subscript m refers to the number of the *pressure zone*; that is, a volume within the computational domain that is allowed to have its own background pressure rise. A closed room within a building, for example, is a pressure zone. The time derivative of the background pressure of the mth pressure zone is found by integrating Eq. (4.23) over the zone volume (denoted by Ω_m):

$$\frac{\partial \overline{p}_m}{\partial t} = \left(\int_{\Omega_m} \mathcal{D} \, dV - \int_{\partial \Omega_m} \mathbf{u} \cdot d\mathbf{S} \right) \Big/ \int_{\Omega_m} \mathcal{P} \, dV \tag{4.24}$$

Equation (4.24) is essentially a consistency condition, ensuring that blowing air or starting a fire within a sealed compartment leads to an appropriate decrease in the divergence within the volume.

In the event that the barrier separating two pressure zones should rupture, Eq. (4.24) is modified so that the pressure in the newly connected zones is driven towards an equilibrium pressure:

$$\overline{p}_{eq} = \frac{\sum_m V_m}{\sum_m V_m / \overline{p}_m} \tag{4.25}$$

Note that

$$\int_{\Omega_m} \mathcal{P} \, dV \approx \frac{V_m}{\gamma \overline{p}_m} \tag{4.26}$$

which allows us to write an expression for the equilibrium pressure using quantities that have already been calculated:

$$\overline{p}_{eq} = \sum_m \overline{p}_m \int_{\Omega_m} \mathcal{P} \, dV \Big/ \sum_m \int_{\Omega_m} \mathcal{P} \, dV \tag{4.27}$$

The pressure in connected zones is driven towards the equilibrium at each time step according to

$$\frac{\partial \overline{p}_m}{\partial t} = r \frac{\overline{p}_{eq} - \overline{p}_m}{\delta t} \tag{4.28}$$

where r is a relaxation factor of 0.2, a somewhat arbitrary value designed to slow down the fairly rapid pressure equilibration.

4.1.3 The Momentum Equation

The three components of the momentum equation are

$$\frac{\partial u}{\partial t} + F_x + \frac{\partial \mathcal{H}}{\partial x} = 0 \quad ; \quad F_x = w\omega_y - v\omega_z - \frac{1}{\rho}\left(f_x + \frac{\partial \tau_{xx}}{\partial x} + \frac{\partial \tau_{xy}}{\partial y} + \frac{\partial \tau_{xz}}{\partial z} \right) \tag{4.29}$$

$$\frac{\partial v}{\partial t} + F_y + \frac{\partial \mathcal{H}}{\partial y} = 0 \quad ; \quad F_y = u\omega_z - w\omega_x - \frac{1}{\rho}\left(f_y + \frac{\partial \tau_{yx}}{\partial x} + \frac{\partial \tau_{yy}}{\partial y} + \frac{\partial \tau_{yz}}{\partial z} \right) \tag{4.30}$$

$$\frac{\partial w}{\partial t} + F_z + \frac{\partial \mathcal{H}}{\partial z} = 0 \quad ; \quad F_z = v\omega_x - u\omega_y - \frac{1}{\rho}\left(f_z + \frac{\partial \tau_{zx}}{\partial x} + \frac{\partial \tau_{zy}}{\partial y} + \frac{\partial \tau_{zz}}{\partial z} \right) \tag{4.31}$$

The spatial discretization of the momentum equations takes the form

$$\frac{\partial u}{\partial t} + F_{x,ijk} + \frac{\mathcal{H}_{i+1,jk} - \mathcal{H}_{ijk}}{\delta x} = 0 \tag{4.32}$$

$$\frac{\partial v}{\partial t} + F_{y,ijk} + \frac{\mathcal{H}_{i,j+1,k} - \mathcal{H}_{ijk}}{\delta y} = 0 \tag{4.33}$$

$$\frac{\partial w}{\partial t} + F_{z,ijk} + \frac{\mathcal{H}_{ij,k+1} - \mathcal{H}_{ijk}}{\delta z} = 0 \tag{4.34}$$

where $\mathcal{H}_{ijk}$ is taken at center of cell ijk, u_{ijk} and $F_{x,ijk}$ are taken at the side of the cell facing in the forward x direction, v_{ijk} and $F_{y,ijk}$ at the side facing in the forward y direction, and w_{ijk} and $F_{z,ijk}$ at the side facing in the forward z (vertical) direction. In the definitions to follow, the components of the vorticity $(\omega_x, \omega_y, \omega_z)$ are located at cell edges pointing in the x, y and z directions, respectively. The same is true for the off-diagonal terms of the viscous stress tensor: $\tau_{zy} = \tau_{yz}$, $\tau_{xz} = \tau_{zx}$, and $\tau_{xy} = \tau_{yx}$. The diagonal components of the stress tensor τ_{xx}, τ_{yy}, and τ_{zz}; the external force components (f_x, f_y, f_z); and the Courant numbers ε_u, ε_v, and ε_w are located at their respective cell faces.

$$F_{x,ijk} = \left(\frac{1 \mp \varepsilon_w}{2} w_{i+\frac{1}{2},jk}\, \omega_{y,ijk} + \frac{1 \pm \varepsilon_w}{2} w_{i+\frac{1}{2},j,k-1}\, \omega_{y,ij,k-1} \right)$$
$$- \left(\frac{1 \mp \varepsilon_v}{2} v_{i+\frac{1}{2},jk}\, \omega_{z,ijk} + \frac{1 \pm \varepsilon_v}{2} v_{i+\frac{1}{2},j-1,k}\, \omega_{z,i,j-1,k} \right)$$
$$- \frac{1}{\rho_{i+\frac{1}{2},jk}} \left(f_{x,ijk} + \frac{\tau_{xx,i+1,jk} - \tau_{xx,ijk}}{\delta x} + \frac{\tau_{xy,ijk} - \tau_{xy,i,j-1,k}}{\delta y} + \frac{\tau_{xz,ijk} - \tau_{xz,i,j,k-1}}{\delta z} \right) \tag{4.35}$$

$$F_{y,ijk} = \left(\frac{1 \mp \varepsilon_u}{2} u_{i,j+\frac{1}{2},k}\, \omega_{z,ijk} + \frac{1 \pm \varepsilon_u}{2} u_{i-1,j+\frac{1}{2},k}\, \omega_{z,i-1,jk} \right)$$
$$- \left(\frac{1 \mp \varepsilon_w}{2} w_{i,j+\frac{1}{2},k}\, \omega_{x,ijk} + \frac{1 \pm \varepsilon_w}{2} w_{i,j+\frac{1}{2},k-1}\, \omega_{x,ij,k-1} \right)$$
$$- \frac{1}{\rho_{i,j+\frac{1}{2},k}} \left(f_{y,ijk} + \frac{\tau_{yx,ijk} - \tau_{yx,i-1,jk}}{\delta x} + \frac{\tau_{yy,i,j+1,k} - \tau_{yy,ijk}}{\delta y} + \frac{\tau_{yz,ijk} - \tau_{yz,i,j,k-1}}{\delta z} \right) \tag{4.36}$$

$$F_{z,ijk} = \left(\frac{1 \mp \varepsilon_v}{2} v_{ij,k+\frac{1}{2}}\, \omega_{x,ijk} + \frac{1 \pm \varepsilon_v}{2} v_{i,j-1,k+\frac{1}{2}}\, \omega_{x,i,j-1,k} \right)$$
$$- \left(\frac{1 \mp \varepsilon_u}{2} u_{ij,k+\frac{1}{2}}\, \omega_{y,ijk} + \frac{1 \pm \varepsilon_u}{2} u_{i-1,j,k+\frac{1}{2}}\, \omega_{y,i-1,jk} \right)$$
$$- \frac{1}{\rho_{ij,k+\frac{1}{2}}} \left(f_{z,ijk} + \frac{\tau_{zx,ijk} - \tau_{zx,i-1,jk}}{\delta x} + \frac{\tau_{zy,ijk} - \tau_{zy,i,j-1,k}}{\delta y} + \frac{\tau_{zz,ij,k+1} - \tau_{zz,ijk}}{\delta z} \right) \tag{4.37}$$

The components of the vorticity vector are:

$$\omega_{x,ijk} = \frac{w_{i,j+1,k} - w_{ijk}}{\delta y} - \frac{v_{ij,k+1} - v_{ijk}}{\delta z} \tag{4.38}$$

$$\omega_{y,ijk} = \frac{u_{ij,k+1} - u_{ijk}}{\delta z} - \frac{w_{i+1,jk} - w_{ijk}}{\delta x} \tag{4.39}$$

$$\omega_{z,ijk} = \frac{v_{i+1,jk} - v_{ijk}}{\delta x} - \frac{u_{i,j+1,k} - u_{ijk}}{\delta y} \tag{4.40}$$

The components of the viscous stress tensor are:

$$\tau_{xx,ijk} = \mu_{ijk} \left(\frac{4}{3} (\nabla \cdot \mathbf{u})_{ijk} - 2\frac{v_{ijk} - v_{i,j-1,k}}{\delta y} - 2\frac{w_{ijk} - w_{ij,k-1}}{\delta z} \right) \tag{4.41}$$

$$\tau_{yy,ijk} = \mu_{ijk} \left(\frac{4}{3} (\nabla \cdot \mathbf{u})_{ijk} - 2\frac{u_{ijk} - u_{i-1,jk}}{\delta x} - 2\frac{w_{ijk} - w_{ij,k-1}}{\delta z} \right) \tag{4.42}$$

$$\tau_{zz,ijk} = \mu_{ijk} \left(\frac{4}{3} (\nabla \cdot \mathbf{u})_{ijk} - 2\frac{u_{ijk} - u_{i-1,jk}}{\delta x} - 2\frac{v_{ijk} - v_{i,j-1,k}}{\delta y} \right) \tag{4.43}$$

$$\tau_{xy,ijk} = \tau_{yx,ijk} = \mu_{i+\frac{1}{2},j+\frac{1}{2},k} \left(\frac{u_{i,j+1,k} - u_{ijk}}{\delta y} + \frac{v_{i+1,jk} - v_{ijk}}{\delta x} \right) \tag{4.44}$$

$$\tau_{xz,ijk} = \tau_{zx,ijk} = \mu_{i+\frac{1}{2},j,k+\frac{1}{2}} \left(\frac{u_{ij,k+1} - u_{ijk}}{\delta z} + \frac{w_{i+1,jk} - w_{ijk}}{\delta x} \right) \tag{4.45}$$

$$\tau_{yz,ijk} = \tau_{zy,ijk} = \mu_{i,j+\frac{1}{2},k+\frac{1}{2}} \left(\frac{v_{ij,k+1} - v_{ijk}}{\delta z} + \frac{w_{i,j+1,k} - w_{ijk}}{\delta y} \right) \tag{4.46}$$

The variables ε_u, ε_v and ε_w are local Courant numbers evaluated at the same locations as the velocity component immediately following them, and serve to bias the differencing of the convective terms in the upwind direction.

$$\varepsilon_u = \frac{u\,\delta t}{\delta x} \quad ; \quad \varepsilon_v = \frac{v\,\delta t}{\delta y} \quad ; \quad \varepsilon_w = \frac{w\,\delta t}{\delta z} \tag{4.47}$$

The subscript $i+\frac{1}{2}$ indicates that a variable is an average of its values at the ith and the $(i+1)$th cell. By construction, the divergence defined in Eq. (4.18) is identically equal to the divergence defined by

$$(\nabla \cdot \mathbf{u})_{ijk} = \frac{u_{ijk} - u_{i-1,jk}}{\delta x} + \frac{v_{ijk} - v_{i,j-1,k}}{\delta y} + \frac{w_{ijk} - w_{ij,k-1}}{\delta z} \tag{4.48}$$

The equivalence of the two definitions of the divergence is a result of the form of the discretized equations, the time-stepping scheme, and the direct solution of the Poisson equation for the pressure.

Viscous Terms (LES)

The major difference between an LES and a DNS calculation is the form of the viscosity, and the thermal and material diffusivities. For a Large Eddy Simulation, the dynamic viscosity is defined at cell centers

$$\mu_{ijk} = \rho_{ijk} (C_s \Delta)^2 |S| \tag{4.49}$$

where C_s is an empirical constant, $\Delta = (\delta x \delta y \delta z)^{\frac{1}{3}}$, and

$$|S|^2 = 2\left(\frac{\partial u}{\partial x}\right)^2 + 2\left(\frac{\partial v}{\partial y}\right)^2 + 2\left(\frac{\partial w}{\partial z}\right)^2 + \left(\frac{\partial u}{\partial y} + \frac{\partial v}{\partial x}\right)^2 + \left(\frac{\partial u}{\partial z} + \frac{\partial w}{\partial x}\right)^2 + \left(\frac{\partial v}{\partial z} + \frac{\partial w}{\partial y}\right)^2 - \frac{2}{3}(\nabla \cdot \mathbf{u})^2 \tag{4.50}$$

The quantity $|S|$ consists of second order spatial differences averaged at cell centers. For example

$$\frac{\partial u}{\partial x} \approx \frac{u_{ijk} - u_{i-1,jk}}{\delta x_i} \tag{4.51}$$

$$\frac{\partial u}{\partial y} \approx \frac{1}{2}\left(\frac{u_{i,j+1,k} - u_{ijk}}{\delta y_{j+\frac{1}{2}}} + \frac{u_{ijk} - u_{i,j-1,k}}{\delta y_{j-\frac{1}{2}}}\right) \tag{4.52}$$

The divergence is described in Section 4.1.2.

The thermal conductivity and material diffusivity of the fluid are related to the viscosity by

$$k_{ijk} = \frac{c_{p,0}\mu_{ijk}}{\mathrm{Pr}_t} \quad ; \quad (\rho D)_{ijk} = \frac{\mu_{ijk}}{\mathrm{Sc}_t} \tag{4.53}$$

where Pr_t is the turbulent Prandtl number and Sc_t is the turbulent Schmidt number, both assumed constant. Note that the specific heat $c_{p,0}$ is that of the dominant species of the mixture. Based on simulations of smoke plumes, C_s is 0.20, Pr_t and Sc_t are 0.5. There are no rigorous justifications for these choices other than through comparison with experimental data [62].

Viscous Terms (DNS)

The dynamic viscosity, thermal conductivity and diffusion coefficients for a DNS calculation are defined at cell centers

$$\mu_{ijk} = \sum_l Y_{l,ijk}\,\mu_l(T_{ijk}) \tag{4.54}$$

$$k_{ijk} = \sum_l Y_{l,ijk}\,k_l(T_{ijk}) \tag{4.55}$$

$$D_{l,ijk} = D_{l0}(T_{ijk}) \tag{4.56}$$

where the values for each individual species are approximated from kinetic theory [36]. The term D_{l0} is the binary diffusion coefficient for species l diffusing into the predominant species 0, usually nitrogen. It is often the case that the numerical grid is too coarse to resolve steep gradients in flow quantities when the temperature is near ambient. However, as the temperature increases and the diffusion coefficients increase in value, the situation improves. As a consequence, there is a provision in the numerical algorithm to place a lower bound on the viscous coefficients to avoid numerical instabilities at temperatures close to ambient.

Velocity Boundary Conditions at a Solid Surface

At solid boundaries, the tangential components of velocity need to be set inside the solid in order to establish a velocity gradient for the numerical velocity field. As an example, consider a solid surface forming the lower boundary of the computational domain ($z = 0$). The horizontal velocity components $u_{ij,1}$ and $v_{ij,1}$ are computed at the vertical faces of the first layer of gas phase grid cells above the solid surface. What should the values of $u_{ij,0}$ and $v_{ij,0}$ be set to such that the flow near the wall is impeded by the same amount as a real turbulent flow? Assuming that the numerical grid is too coarse to resolve the boundary layer (of nominal thickness d), and assuming a turbulent velocity profile

$$U(z) = \begin{cases} U_0(z/d)^{1/7} & z < d \\ U_0 & z > d \end{cases} \tag{4.57}$$

a simple slip boundary condition can be worked out such that

$$u_{ij,0} = u_{ij,1}\left(1 - \frac{d}{\delta z}\right) \quad ; \quad v_{ij,0} = v_{ij,1}\left(1 - \frac{d}{\delta z}\right) \tag{4.58}$$

where δz is the height of the grid cell. For coarse grids, the boundary condition is very similar to a "free-slip" condition because $d << \delta z$.

Past and present versions of FDS have employed a default boundary condition for LES calculations where $u_{ij,0}$ and $v_{ij,0}$ are set to one-half the values of $u_{ij,1}$ and $v_{ij,1}$, respectively. Although from the discussion above this implies that the thickness of the boundary layer d is assumed to be half that of the grid cell δz, in practice, it really implies that real walls are covered with small obstructions that are half a cell thick or less in size, in which case they do not appear explicitly in the simulation. The "half-slip" condition is an attempt to account for this wall clutter.

In a DNS calculation, this discussion is moot. The inner-wall "ghost" cell velocities are set so that the velocity at the wall surface is zero.

Force Terms

The external force term components are defined at cell faces, just like the velocity components. For example, the drag force components from sprinkler droplets are:

$$f_{x,ijk} = \frac{1}{2} \frac{\sum \rho C_D \pi r_d^2 (u_d - u_{ijk})|\mathbf{u}_d - \mathbf{u}|}{\delta x \, \delta y \, \delta z} \tag{4.59}$$

$$f_{y,ijk} = \frac{1}{2} \frac{\sum \rho C_D \pi r_d^2 (v_d - v_{ijk})|\mathbf{u}_d - \mathbf{u}|}{\delta x \, \delta y \, \delta z} \tag{4.60}$$

$$f_{z,ijk} = \frac{1}{2} \frac{\sum \rho C_D \pi r_d^2 (w_d - w_{ijk})|\mathbf{u}_d - \mathbf{u}|}{\delta x \, \delta y \, \delta z} \tag{4.61}$$

where r_d is the radius of a droplet, $\mathbf{u} = (u_d, v_d, w_d)$ the velocity of a droplet, C_D the drag coefficient, and $\delta x \, \delta y \, \delta z$ the volume of the ijkth cell. The summations represent all droplets within a grid cell centered about the x, y and z faces of a grid cell respectively.

Time Step

The time step is constrained by the convective and diffusive transport speeds via two conditions. The first is known as the Courant-Friedrichs-Lewy (CFL) condition:

$$\delta t \, \max \left(\frac{|u_{ijk}|}{\delta x}, \frac{|v_{ijk}|}{\delta y}, \frac{|w_{ijk}|}{\delta z} \right) < 1 \tag{4.62}$$

The estimated velocities $u^{(n+1)_e}$, $v^{(n+1)_e}$ and $w^{(n+1)_e}$ are tested at each time step to ensure that the CFL condition is satisfied. If it is not, then the time step is set to 0.8 of its allowed maximum value and the estimated velocities are recomputed (and checked again). The CFL condition asserts that the solution of the equations cannot be updated with a time step larger than that allowing a parcel of fluid to cross a grid cell. For most large-scale calculations where convective transport dominates diffusive, the CFL condition restricts the time step.

However, in small, finely-gridded domains, a second condition often dominates:

$$2 \max \left(\nu, D, \frac{k}{\rho c_p} \right) \delta t \left(\frac{1}{\delta x^2} + \frac{1}{dy^2} + \frac{1}{\delta z^2} \right) < 1 \tag{4.63}$$

Note that this constraint is applied to the momentum, mass and energy equations via the relevant diffusion parameter – viscosity, material diffusivity or thermal conductivity. This constraint on the time step, often referred to as the Von Neumann criterion, is typical of any explicit, second-order numerical scheme for solving a parabolic partial differential equation. To save CPU time, the Von Neumann criterion is only invoked for DNS calculations or for LES calculations with grid cells smaller than 5 mm.

4.1.4 The Pressure Equation

The momentum equation is

$$\frac{\partial \mathbf{u}}{\partial t} + \mathbf{F} + \nabla \mathcal{H} = 0 \tag{4.64}$$

The divergence operator applied to the three components of the discretized momentum equation (4.32–4.34) yields the following discrete Poisson equation for the modified pressure, $\mathcal{H}$:

$$\frac{\mathcal{H}_{i+1,jk} - 2\mathcal{H}_{ijk} + \mathcal{H}_{i-1,jk}}{\delta x^2} + \frac{\mathcal{H}_{i,j+1,k} - 2\mathcal{H}_{ijk} + \mathcal{H}_{i,j-1,k}}{\delta y^2} + \frac{\mathcal{H}_{ij,k+1} - 2\mathcal{H}_{ijk} + \mathcal{H}_{ij,k-1}}{\delta z^2}$$
$$= -\frac{F_{x,ijk} - F_{x,i-1,jk}}{\delta x} - \frac{F_{y,ijk} - F_{y,i,j-1,k}}{\delta y} - \frac{F_{z,ijk} - F_{z,ij,k-1}}{\delta z} - \frac{\partial}{\partial t}(\nabla \cdot \mathbf{u})_{ijk} \tag{4.65}$$

The lack of a superscript implies that all quantities are to be evaluated at the same time level. This elliptic partial differential equation is solved using a direct (non-iterative) FFT-based solver [63] that is part of a library of routines for solving elliptic PDEs called CRAYFISHPAK[1]. To ensure that the divergence of the fluid is consistent with the definition given in Eq. (3.14), the time derivative of the divergence is defined

$$\frac{\partial}{\partial t}(\nabla \cdot \mathbf{u})_{ijk} = \frac{(\nabla \cdot \mathbf{u})_{ijk}^{(n+1)e} - (\nabla \cdot \mathbf{u})_{ijk}^{n}}{\delta t} \tag{4.66}$$

at the predictor step, and then

$$\frac{\partial}{\partial t}(\nabla \cdot \mathbf{u})_{ijk} = \frac{2(\nabla \cdot \mathbf{u})_{ijk}^{n+1} - (\nabla \cdot \mathbf{u})_{ijk}^{(n+1)e} - (\nabla \cdot \mathbf{u})_{ijk}^{n}}{\delta t} \tag{4.67}$$

at the corrector step. The discretization of the divergence was given in Eq. (4.18).

Direct Poisson solvers are most efficient if the domain is a rectangular region, although other geometries such as cylinders and spheres can be handled almost as easily. For these solvers, a no-flux condition is simple to prescribe at external boundaries. For example, at the floor, $z = 0$, the Poisson solver is supplied with the Neumann boundary condition

$$\frac{\mathcal{H}_{ij,1} - \mathcal{H}_{ij,0}}{\delta z} = -F_{z,ij,0} \tag{4.68}$$

However, many practical problems involve more complicated geometries. For building fires, doors and windows within multi-room enclosures are very important features of the simulations. These elements may be included in the overall domain as masked grid cells, but the no-flux condition (4.68) cannot be directly prescribed at the boundaries of these blocked cells. Fortunately, it is possible to exploit the relatively small changes in the pressure from one time step to the next to enforce the no-flux condition. At the start of a time step, the components of the convection/diffusion term $\mathbf{F}$ are computed at all cell faces that do not correspond to walls. At those cell faces that do correspond to solid walls, we prescribe

$$F_n = -\frac{\partial \mathcal{H}^*}{\partial n} + \frac{u_n}{\delta t} \tag{4.69}$$

where F_n is the normal component of $\mathbf{F}$ at the wall.

The asterisk indicates the most recent value of the pressure. The pressure at this particular time step is not known until the Poisson equation is solved. Equation (4.69) asserts that following the solution of the Poisson equation for the pressure, the normal component of velocity u_n will be driven nearly (but not

---

[1]CRAYFISHPAK, a vectorized form of the elliptic equation solver FISHPAK, was originally developed at the National Center for Atmospheric Research (NCAR) in Boulder, Colorado.

exactly) to zero. This is approximate because the true value of the velocity time derivative depends on the solution of the pressure equation, but since the most recent estimate of pressure is used, the approximation is very good. Also, even though there are small errors in normal velocity at solid surfaces, the divergence of each blocked cell remains exactly zero for the duration of the calculation. In other words, the total flux into a given obstruction is always identically zero, and the error in normal velocity is usually at least several orders of magnitude smaller than the characteristic flow velocity. When implemented as part of a predictor-corrector updating scheme, the no-flux condition at solid surfaces is maintained remarkably well.

At open boundaries (say $i = nx$), $\mathcal{H}$ is prescribed depending on whether the flow is incoming or outgoing. Define $q \equiv u_{nx,jk}^2 + \bar{v}_{nx,jk}^2 + \bar{w}_{nx,jk}^2$ where nx is the index of the last gas phase cell in the x direction and $u_{nx,jk}$ is the x component of velocity at the boundary. The density at the boundary is denoted ρ_w (for "wall"). The background density used in defining $\mathcal{H}$ is ρ_∞ (see Sec. 3.1.4). The overbars on v and w indicate an interpolation of these components to the boundary location. The boundary condition on $\mathcal{H}$ is

$$
\begin{aligned}
\mathcal{H}_{nx+\frac{1}{2},jk} &= \mathcal{H}_{ext} + \tfrac{1}{2}q && \text{for} \quad u_{nx,jk} > 0 \\
\mathcal{H}_{nx+\frac{1}{2},jk} &= \mathcal{H}_{ext} + \mathcal{H}_0 + \tfrac{1}{2}q\left(1 - \tfrac{\rho_w}{\rho_\infty}\right) && \text{for} \quad u_{nx,jk} \leq 0
\end{aligned}
\tag{4.70}
$$

The external dynamic pressure, $\mathcal{H}_{ext} = \tilde{p}_{ext}/\rho_\infty$, as well as the initial dynamic pressure, $\mathcal{H}_0 = \tfrac{1}{2}(u_0^2 + v_0^2 + w_0^2)\rho_0/\rho_\infty$, are specified by the user ($\tilde{p}_{ext}$ is set with DYNAMIC_PRESSURE for a specific VENT). The condition (4.70) follows from prescribing the fluctuating hydrodynamic pressure $\tilde{p}_{ext}$ at an outflow vent (zero by default) and assuming the Bernoulli equation applies for an inflow vent where the fluid accelerates from the state $\{\tilde{p}_{ext}, \rho_0, u_0, v_0, w_0\}$ along a streamline. Note that the background density ρ_∞ is usually equal to the initial ambient density ρ_0 at the start of a calculation, but may change in time if the baroclinic correction term is included (again, see Sec. 3.1.4).

The value of $\mathcal{H}$ in the ghost cell is

$$
\mathcal{H}_{nx+1,jk} = 2\mathcal{H}_{nx+\frac{1}{2},jk} - \mathcal{H}_{nx,jk}
\tag{4.71}
$$

4.1.5 Multiple Mesh Considerations

In this section we provide an overview of the "pressure correction" scheme used in FDS to enforce global volume conservation in multiple mesh (i.e. parallel) computations (a "mesh" refers to the computational domain which is mapped to an individual processor). There are three critical components of the scheme which we discuss in further detail below and in Appendix C: (1) the averaging of the normal velocity component at a mesh interface, (2) the Dirichlet boundary value for the hydrodynamic pressure, and (3) the Neumann boundary condition for the pressure correction. The term "pressure correction" actually best identifies only the third component of the scheme which is ultimately responsible for enforcing volume conservation from mesh to mesh (and thus globally). However, the first two components of the scheme are perhaps even more important for maintaining stability of the solution.

The basic idea behind the scheme is the following. First, we break up the hydrodynamic pressure $\mathcal{H}$ into a fluctuating component $\mathcal{H}'$ and a small correction $\mathcal{H}''$. We may then write the momentum equation as

$$
\frac{\partial \mathbf{u}}{\partial t} = -\left[\mathbf{F} + \nabla \mathcal{H}' + \nabla \mathcal{H}''\right].
\tag{4.72}
$$

Equation (4.72) is integrated in time under the constraints that the pressure fluctuation satisfies the Poisson equation,

$$
\nabla^2 \mathcal{H}' = -\left[\frac{\partial}{\partial t}(\nabla \cdot \mathbf{u}) + \nabla \cdot \mathbf{F}\right],
\tag{4.73}
$$

and the pressure correction satisfies Laplace's equation,

$$
\nabla^2 \mathcal{H}'' = 0.
\tag{4.74}
$$

Now, as opposed to conventional domain decomposition techniques where boundary conditions are prescribed only along the global boundary of the problem domain and the PDEs (4.73) and (4.74) are supposed to apply across mesh interfaces (a.k.a. patch or interpolated boundaries), in the FDS multiple mesh algorithm we impose a Dirichlet condition on $\mathcal{H}'$ and a Neumann condition on $\mathcal{H}''$ at patch boundaries. The Dirichlet condition for the pressure fluctuation is designed to provide stability and accuracy and the Neumann condition for the (ideally small) pressure correction field is designed to enforce volume conservation from mesh to mesh. Once these boundary conditions are prescribed, calculations on each mesh may proceed independently, resulting in an algorithm which is embarrassingly parallel. Note that this scheme may be viewed as a single iteration in an additive Schwarz method.

Below we provide a summary of the multiple mesh algorithm, similar to the single mesh algorithm described above. The key differences between the single and multiple mesh procedures are the averaging of the velocity field at mesh boundaries and the additional step of solving the Laplace equation in the multiple mesh case if the pressure correction scheme is invoked.

Temporal Discretization (Multiple Mesh Case)

1. Compute the "patch-average" velocity field $\bar{\mathbf{u}}^n$ (see Appendix C).

2. The thermodynamic quantities ρ, Y_α, and $\overline{p}_m$ are estimated at the next time step with an explicit Euler step. For example, the density is estimated by

$$\rho^{(n+1)_e} = \rho^n - \delta t(\bar{\mathbf{u}}^n \cdot \nabla \rho^n + \rho^n \nabla \cdot \bar{\mathbf{u}}^n) \tag{4.75}$$

   Before boundary conditions for ρ and Y_α are applied, values of these quantities at interpolated mesh boundaries are exchanged via MPI calls.

3. The divergence $(\nabla \cdot \mathbf{u})^{(n+1)_e}$ is formed from these estimated thermodynamic quantities. The normal velocity components at boundaries that are needed to form the divergence are assumed known.

4. A Poisson equation for the pressure fluctuation is solved with a direct solver

$$\nabla^2 \mathcal{H}'^{(n+1)_e} = -\left[\frac{(\nabla \cdot \mathbf{u})^{(n+1)_e} - (\nabla \cdot \bar{\mathbf{u}})^n}{\delta t}\right] - \nabla \cdot \bar{\mathbf{F}}^n \tag{4.76}$$

   Note that the vector $\bar{\mathbf{F}}^n = \mathbf{F}(\rho^n, \bar{\mathbf{u}}^n)$ is computed using patch-averaged velocities and that the divergence of the patch-averaged field is computed explicitly.

5. If the 'pressure correction' scheme is invoked then we solve the Laplace equation for $\mathcal{H}''^{(n+1)_e}$ on each mesh with Neumann boundary conditions designed to enforce volume conservation from mesh to mesh (details are provided in Appendix C). This procedure involves a mesh exchange via MPI.

6. The velocity is estimated at the next time step

$$\mathbf{u}^{(n+1)_e} = \bar{\mathbf{u}}^n - \delta t\left(\bar{\mathbf{F}}^n + \nabla \mathcal{H}'^{(n+1)_e} + \nabla \mathcal{H}''^{(n+1)_e}\right) \tag{4.77}$$

   Note that the divergence of the estimated velocity field is identically equal to the estimated divergence $(\nabla \cdot \mathbf{u})^{(n+1)_e}$ that was derived from the estimated thermodynamic quantities. The time step is checked for stability and the preceding steps are rerun with a smaller time step if necessary.

   This concludes the "Predictor" stage of the time step. At this point, values of $\mathcal{H}'$ and the components of $\mathbf{u}$ are exchanged at mesh boundaries via MPI calls.

7. We compute the "patch-average" velocity field $\bar{\mathbf{u}}^{(n+1)_e}$ (see Appendix C).

8. The thermodynamic quantities ρ, Y_α, and $\overline{p}_m$ are "corrected" at the next time step. For example, the density is corrected

$$\rho^{n+1} = \frac{1}{2}\left[\rho^n + \rho^{(n+1)_e} - \delta t \left(\bar{\mathbf{u}}^{(n+1)_e} \cdot \nabla \rho^{(n+1)_e} + \rho^{(n+1)_e} \nabla \cdot \bar{\mathbf{u}}^{(n+1)_e}\right)\right] \qquad (4.78)$$

Before boundary conditions for ρ and Y_α are applied, values of these quantities at interpolated mesh boundaries are exchanged via MPI calls.

9. The corrected divergence $(\nabla \cdot \mathbf{u})^{n+1}$ is computed from the corrected thermodynamic quantities.

10. The pressure fluctuation is recomputed using estimated quantities

$$\nabla^2 \mathcal{H}'^{n+1} = -\left[\frac{2(\nabla \cdot \mathbf{u})^{n+1} - (\nabla \cdot \bar{\mathbf{u}})^{(n+1)_e} - (\nabla \cdot \bar{\mathbf{u}})^n}{\delta t}\right] - \nabla \cdot \bar{\mathbf{F}}^{(n+1)_e} \qquad (4.79)$$

Again, note that only $(\nabla \cdot \mathbf{u})^{n+1}$ is taken from the equation of state. The divergences of the patch-averaged fields are computed explicitly.

11. If the 'pressure correction' scheme is invoked then we solve the Laplace equation for $\mathcal{H}'''^{n+1}$ on each mesh with Neumann boundary conditions designed to enforce volume conservation from mesh to mesh (details are provided in Appendix C). This procedure involves a mesh exchange via MPI.

12. The velocity is corrected

$$\mathbf{u}^{n+1} = \frac{1}{2}\left[\bar{\mathbf{u}}^n + \bar{\mathbf{u}}^{(n+1)_e} - \delta t \left(\bar{\mathbf{F}}^{(n+1)_e} + \nabla \mathcal{H}'^{n+1} + \nabla \mathcal{H}'''^{n+1}\right)\right] \qquad (4.80)$$

Note again that the divergence of the corrected velocity field is identically equal to the corrected divergence.

At the conclusion of the time step, values of $\mathcal{H}'$ and the components of $\mathbf{u}$ are exchanged at mesh boundaries via MPI calls.

4.2 Combustion

4.2.1 Heat Release Rate (Mixture Fraction)

When using the mixture fraction-based combustion model, we must extract the local heat release rate per unit volume from the computed mixture fraction field. The mixture fraction, Z, is partitioned into at least 2 components, Z_α, such that the sum of the components equals the mixture fraction. Each component is tracked via a transport equation, and the conversion of mass from one component to another represents a reaction step and an associated release of energy.

Two-Parameter Mixture Fraction

When the mixture fraction is divided into two components, Z_1 and Z_2, there is one chemical reaction that converts Z_1 to Z_2. Recall from Section 3.2.1 that this represents single-step combustion with the possibility of local extinction. From the mixture fraction variables one can determine the amount of fuel and oxygen present in a grid cell. Ideally, we could use these values in a finite-rate computation to determine the heat release rate; however, for most computations, the grid resolution is too coarse to resolve the flame. Thus, flame temperatures will not be realized and a finite-rate computation will not succeed. Instead, if any grid cell surrounding one containing both fuel and oxygen satisfies the "Burn" criteria depicted in Fig. 3.4, combustion is assumed to occur. The heat release rate is computed as

$$\dot{q}''' = \frac{\min\left(\rho Y_F, s\rho Y_{O_2}\right)}{\tau} \Delta H \quad ; \quad s = \frac{W_F}{\nu_{O_2} W_{O_2}} \tag{4.81}$$

Here, τ is a mixing time scale [64] given by

$$\tau = \frac{C\left(\delta x \delta y \delta z\right)^{\frac{2}{3}}}{D_{LES}} \tag{4.82}$$

The coefficient, C, is taken as 0.1 in FDS by default, based on comparisons to various flame height correlations.

There are two additional bounds on the local heat release rate per unit volume. One is based on an empirically determined maximum heat release rate per unit area of flame sheet:

$$\dot{q}'''_{max,1} = \frac{\dot{q}''_{max}}{\left(\delta x \delta y \delta z\right)^{\frac{1}{3}}} \quad ; \quad \dot{q}''_{max} = 200 \ \text{kW/m}^2 \tag{4.83}$$

The second bound is based on an empirical estimate of the average volumetric heat release rate of a fire. Orloff and De Ris [65] suggest a value of 1200 kW/m³, and FDS uses by default a value of 3000 kW/m³ as an upper bound.

$$\dot{q}'''_{max,2} = \frac{\overline{\dot{q}'''_{max}} - \left(1 - \delta t/\tau'\right)\overline{\dot{q}'''}}{\delta t/\tau'} \quad ; \quad \overline{\dot{q}'''_{max}} = 3000 \ \text{kW/m}^3 \tag{4.84}$$

Here, τ' is an averaging time that should be larger than the pulsation period of the fire.[2]

Once the heat release rate is computed, the mixture fraction variables are updated:

$$Z_1^{n+1} = Z_1^n - \frac{\dot{q}'''\Delta t}{\rho \Delta H} \quad ; \quad Z_2^{n+1} = Z_2^n + \frac{\dot{q}'''\Delta t}{\rho \Delta H} \tag{4.85}$$

Note that the total fuel mass is conserved in this process; $Z = Z_1 + Z_2$ is still a conserved quantity.

---

[2] All of these parameters are accessible to the model user. See the FDS User's Guide [3] for more details.

Three-Parameter Mixture Fraction

When the mixture fraction is divided into three components, Z_1, Z_2, and Z_3, there are two chemical reactions that convert Z_1 to Z_2 and Z_2 to Z_3. Recall from Section 3.2.1 that this represents two-step combustion (fuel to CO and CO to CO_2). The first step occurs as it does for the two-parameter mixture fraction with a modified heat of combustion that accounts for the conversion of fuel to CO rather than CO_2. The second step is performed for all grid cells that contain CO and O_2. If $\dot{q}''' \neq 0$ in a grid cell after the first step, then additional heat is released according to

$$\dot{q}'''_{CO} = \min \left[\frac{\max \left(\rho Z_2, s\rho Y_{O_2} \right)}{\delta t} \Delta H_{CO} \, , \, \dot{q}'''_{max} - \dot{q}''' \right] \tag{4.86}$$

If $\dot{q}''' = 0$ after the first step, then it is presumed that the cell is out of the combustion region (say in the upper layer of smoke-filled compartment), and a finite-rate reaction computation is performed to convert CO to CO_2 (see the next section for a discussion of the algorithm for computing a finite-rate reaction). The $\dot{q}'''_{CO}$ computed using the finite-rate reaction is still limited by $\dot{q}'''_{max}$. Once $\dot{q}'''_{CO}$ is computed the mixture fraction variables are updated:

$$Z_2{}^{n+1} = Z_2{}^n - \frac{\dot{q}'''_{CO}\Delta t}{\rho \, \Delta H_{CO}} \quad ; \quad Z_3{}^{n+1} = Z_3{}^n + \frac{\dot{q}'''_{CO}\Delta t}{\rho \, \Delta H_{CO}} \tag{4.87}$$

4.2.2 Heat Release Rate (Finite-Rate Reaction)

For simulations that do not employ a mixture fraction-based combustion model, multi-step, finite-rate reactions are assumed, taking the form:

$$\nu_{C_xH_y} C_xH_y + \nu_{O_2} O_2 \longrightarrow \nu_{CO_2} CO_2 + \nu_{H_2O} H_2O \tag{4.88}$$

It is assumed that the chemical reaction time scale is much shorter than any convective or diffusive transport time scale. Thus, it makes sense to calculate the consequences of the reaction assuming all other processes are frozen in a state corresponding to the beginning of the time step. For each grid cell, at the start of a time step where $t = t^n$ and $Y^n_{C_xH_y,ijk}\rho_{ijk}/W_F \equiv X_F(t^n)$ and $Y^n_{O_2,ijk}\rho_{ijk}/W_{O_2} \equiv X_{O_2}(t^n)$, the following set of ODEs is solved numerically with a second-order Runge-Kutta scheme

$$\frac{dX_F}{dt} = -B \, X_F(t)^a \, X_{O_2}(t)^b \, e^{-E/RT_{ijk}} \tag{4.89}$$

$$\frac{dX_{O_2}}{dt} = -\frac{\nu_{O_2}}{\nu_F} \frac{dX_F}{dt} \tag{4.90}$$

The temperature T_{ijk} and density ρ_{ijk} are fixed at their values at time t^n and the ODEs are iterated from t^n to t^{n+1} in about 20 time steps. The pre-exponential factor B, the activation energy E, and the exponents a and b are input parameters which are in typically assigned the values of ν_F and ν_{O_2}. At the end of each sub-time step the values of X_F and X_{O_2} are updated.

The average heat release rate over the entire time step is given by

$$\dot{q}'''^n_{ijk} = \Delta H \, \rho^n_{ijk} \frac{Y_F(t^n) - Y_F(t^{n+1})}{\delta t} \tag{4.91}$$

where $\delta t = t^{n+1} - t^n$. The species mass fractions are adjusted at this point in the calculation (before the convection and diffusion update)

$$Y^n_{\alpha,ijk} = Y_\alpha(t^n) - \frac{\nu_\alpha W_\alpha}{\nu_F W_F} \left(Y_F(t^n) - Y_F(t^{n+1}) \right) \tag{4.92}$$

If multiple chemical reactions have been specified, equations 4.89 and 4.90 are evaluated for each reaction during each of the 100 time steps. The reactions are evaluated in the order that they are entered in the input file.

4.3 Thermal Radiation

This section describes how $\nabla \cdot \dot{\mathbf{q}}_r''$ (the radiative loss term) is computed at all gas-phase cells. Plus, it describes how the radiative and convective heat fluxes, $\dot{q}_r''$ and $\dot{q}_c''$, are computed at solid boundaries.

4.3.1 Discretization of the Radiative Heat Transfer Equation

The radiative transport equation (3.79) is solved using techniques similar to those for convective transport in finite volume methods for fluid flow [66], thus the name given to it is the Finite Volume Method (FVM). More details of the model implementation can be found from [67]. To obtain the discretized form of the RTE, the unit sphere is divided into a finite number of solid angles. In each grid cell a discretized equation is derived by integrating Eq. (3.79) over the volume of cell ijk and the control angle $\delta\Omega^l$, to obtain

$$\int_{\delta\Omega^l} \int_{V_{ijk}} \mathbf{s}' \cdot \nabla I(\mathbf{x}',\mathbf{s}') d\mathbf{x}' d\mathbf{s}' = \int_{\delta\Omega^l} \int_{V_{ijk}} \kappa(\mathbf{x}') \left[I_b(\mathbf{x}') - I(\mathbf{x}',\mathbf{s}') \right] d\mathbf{x}' d\mathbf{s}' \tag{4.93}$$

The volume integral on the left hand side is replaced by a surface integral over the cell faces using the divergence theorem. Note that the procedure outlined below is appropriate for each band of a wide band model, thus the subscript n has been removed for clarity.

Assuming that the radiation intensity $I(\mathbf{x},\mathbf{s})$ is constant on each of the cell faces, the surface integral can be approximated by a sum over the cell faces. Assuming further that $I(\mathbf{x},\mathbf{s})$ is constant within the volume V_{ijk} and over the angle $\delta\Omega^l$ we obtain

$$\sum_{m=1}^{6} A_m I_m^l \int_{\Omega^l} (\mathbf{s}' \cdot \mathbf{n}_m) d\mathbf{s}' = \kappa_{ijk} \left[I_{b,ijk} - I_{ijk}^l \right] V_{ijk} \delta\Omega^l \tag{4.94}$$

where

I_{ijk}^l	radiant intensity in direction l
I_m^l	radiant intensity at cell face m
$I_{b,ijk}$	radiant blackbody Intensity in cell
$\delta\Omega^l$	solid angle corresponding to direction l
V_{ijk}	volume of cell ijk
A_m	area of cell face m
$\mathbf{n}_m$	unit normal vector of the cell face m

Note that while the intensity is assumed constant within the angle $\delta\Omega^l$, its direction covers the angle $\delta\Omega^l$ exactly.

In Cartesian coordinates[3], the normal vectors $\mathbf{n}_m$ are the base vectors of the coordinate system and the integrals over the solid angle do not depend on the physical coordinate, but the direction only. The intensities on the cell boundaries, I_m^l, are calculated using a first-order upwind scheme. If the physical space is swept in the direction $\mathbf{s}^l$, the intensity I_{ijk}^l can be directly obtained from an algebraic equation. This makes the numerical solution of the FVM very fast. Iterations are needed only to account for the reflective boundaries. However, this is seldom necessary in practice, because the time step set by the flow solver is small.

The grid used for the RTE solver is the same as for the fluid solver. The coordinate system used to discretize the solid angle is shown in Figure 4.1. The discretization of the solid angle is done by dividing first the polar angle, θ, into N_θ bands, where N_θ is an even integer. Each θ-band is then divided into $N_\phi(\theta)$

---

[3]In the axisymmetric case equation (4.94) becomes a little bit more complicated, as the cell face normal vectors $\mathbf{n}_m$ are not always constant. However, the computational efficiency can still be retained.
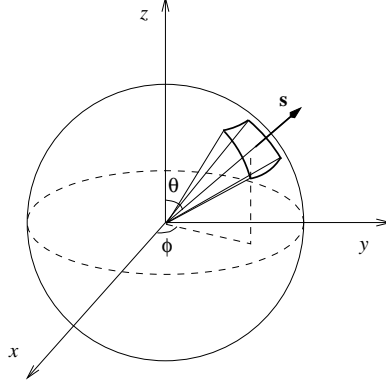
Figure 4.1: Coordinate system of the angular discretization.

parts in the azimuthal (ϕ) direction. $N_\phi(\theta)$ must be divisible by 4. The numbers N_θ and $N_\phi(\theta)$ are chosen to give the total number of angles N_Ω as close to the value defined by the user as possible. N_Ω is calculated as

$$N_\Omega = \sum_{i=1}^{N_\theta} N_\phi(\theta_i) \tag{4.95}$$

The distribution of the angles is based on empirical rules that try to produce equal solid angles $\delta\Omega^l = 4\pi/N_\Omega$. The number of θ-bands is

$$N_\theta = 1.17\, N_\Omega^{1/2.26} \tag{4.96}$$

rounded to the nearest even integer. The number of ϕ-angles on each band is

$$N_\phi(\theta) = \max\left\{4, 0.5 N_\Omega \left[\cos(\theta^-) - \cos(\theta^+)\right]\right\} \tag{4.97}$$

rounded to the nearest integer that is divisible by 4. θ^- and θ^+ are the lower and upper bounds of the θ-band, respectively. The discretization is symmetric with respect to the planes $x = 0$, $y = 0$, and $z = 0$. This symmetry has three important benefits: First, it avoids the problems caused by the fact that the first-order upwind scheme, used to calculate intensities on the cell boundaries, is more diffusive in non-axial directions than axial. Second, the treatment of the mirror boundaries becomes very simple, as will be shown later. Third, it avoids so called "overhang" situations, where $\mathbf{s} \cdot \mathbf{i}$, $\mathbf{s} \cdot \mathbf{j}$ or $\mathbf{s} \cdot \mathbf{k}$ changes sign inside the control angle. These "overhangs" would make the resulting system of linear equations more complicated.

In the axially symmetric case these "overhangs" can not be avoided, and a special treatment, developed by Murthy and Mathur [68], is applied. In these cases $N_\phi(\theta_i)$ is kept constant, and the total number of angles is $N_\Omega = N_\theta \times N_\phi$. In addition, the angle of the vertical slice of the cylinder is chosen to be same as $\delta\phi$.

The cell face intensities, I_m^l appearing on the left hand side of (4.94) are calculated using a first order upwind scheme. Consider, for example, a control angle having a direction vector $\mathbf{s}$. If the radiation is traveling in the positive x-direction, *i.e.* $\mathbf{s} \cdot \mathbf{i} \geq 0$, the intensity on the upwind side, I_{xu}^l is assumed to be the intensity in the neighboring cell, $I_{i-1\,jk}^l$, and the intensity on the downwind side is the intensity in the cell itself I_{ijk}^l.

On a rectilinear grid, the normal vectors $\mathbf{n}_m$ are the base vectors of the coordinate system and the integrals over the solid angle can be calculated analytically. Equation (4.94) can be simplified

$$a_{ijk}^l I_{ijk}^l = a_x^l I_{xu}^l + a_y^l I_{yu}^l + a_z^l I_{zu}^l + b_{ijk}^l \tag{4.98}$$

where

$$a_{ijk}^l = A_x|D_x^l| + A_y|D_y^l| + A_z|D_z^l| + \kappa_{ijk} V_{ijk}\delta\Omega^l \tag{4.99}$$

$$a_x^l = A_x|D_x^l| \tag{4.100}$$
$$a_y^l = A_y|D_y^l| \tag{4.101}$$
$$a_z^l = A_z|D_z^l| \tag{4.102}$$

$$b_{ijk}^l = \kappa_{ijk} I_{b,ijk} V_{ijk} \,\delta\Omega^l \tag{4.103}$$

$$\delta\Omega^l = \int_{\Omega^l} d\Omega = \int_{\delta\phi}\int_{\delta\theta} \sin\theta\, d\theta\, d\phi \tag{4.104}$$

$$D_x^l = \int_{\Omega^l}(\mathbf{s}^l\cdot\mathbf{i})d\Omega \tag{4.105}$$
$$= \int_{\delta\phi}\int_{\delta\theta}(\mathbf{s}^l\cdot\mathbf{i})\sin\theta\, d\theta d\phi$$
$$= \int_{\delta\phi}\int_{\delta\theta}\cos\phi\sin\theta\sin\theta\, d\theta d\phi$$
$$= \frac{1}{2}\left(\sin\phi^+ - \sin\phi^-\right)\left[\Delta\theta - \left(\cos\theta^+\sin\theta^+ - \cos\theta^-\sin\theta^-\right)\right]$$
$$D_y^l = \int_{\Omega^l}(\mathbf{s}^l\cdot\mathbf{j})d\Omega \tag{4.106}$$
$$= \int_{\delta\phi}\int_{\delta\theta}\sin\phi\sin\theta\sin\theta\, d\theta d\phi$$
$$= \frac{1}{2}\left(\cos\phi^- - \cos\phi^+\right)\left[\Delta\theta - \left(\cos\theta^+\sin\theta^+ - \cos\theta^-\sin\theta^-\right)\right]$$
$$D_z^l = \int_{\Omega^l}(\mathbf{s}^l\cdot\mathbf{k})d\Omega \tag{4.107}$$
$$= \int_{\delta\phi}\int_{\delta\theta}\cos\theta\sin\theta\, d\theta d\phi$$
$$= \frac{1}{2}\Delta\phi\left[\left(\sin\theta^+\right)^2 - \left(\sin\theta^-\right)^2\right]$$

Here $\mathbf{i}$, $\mathbf{j}$ and $\mathbf{k}$ are the base vectors of the Cartesian coordinate system. θ^+, θ^-, ϕ^+ and ϕ^- are the upper and lower boundaries of the control angle in the polar and azimuthal directions, respectively, and $\Delta\theta = \theta^+ - \theta^-$ and $\Delta\phi = \phi^+ - \phi^-$. In the cells next to a wall, the areas A_m of the faces, that are perpendicular to the wall, are multiplied by 0.5.

The solution method of (4.98) is based on an explicit marching sequence [69]. The marching direction depends on the propagation direction of the radiation intensity. As the marching is done in the "downwind" direction, the "upwind" intensities in all three spatial directions are known, and the intensity I_{ijk}^l can be solved directly. Iterations may be needed only with the reflective walls and optically thick situations. Currently, no iterations are made.

4.3.2 Radiation Heat Transfer to Solid Objects

The boundary condition on a solid wall is given as

$$I_w^l = \varepsilon \frac{\sigma T_w^4}{\pi} + \frac{1-\varepsilon}{\pi} \sum_{D_w^{l'}<0} I_w^{l'} |D_w^{l'}| \tag{4.108}$$

where $D_w^{l'} = \int_{\Omega^{l'}} (\mathbf{s} \cdot \mathbf{n}_w) d\Omega$. The constraint $D_w^{l'} < 0$ means that only the "incoming" directions are taken into account when calculating the reflection. The *net* radiative heat flux on the wall is

$$\dot{q}_r'' = \sum_{l=1}^{N_\Omega} I_w^l \int_{\delta\Omega^l} (\mathbf{s}' \cdot \mathbf{n}_w) \, d\mathbf{s}' = \sum_{l=1}^{N_\Omega} I_w^l D_n^l \tag{4.109}$$

where the coefficients D_n^l are equal to $\pm D_x^l$, $\pm D_y^l$ or $\pm D_z^l$, and can be calculated for each wall element at the start of the calculation.

The open boundaries are treated as black walls, where the incoming intensity is the black body intensity of the ambient temperature. On mirror boundaries the intensities leaving the wall are calculated from the incoming intensities using a predefined connection matrix:

$$I_{w,ijk}^l = I^{l'} \tag{4.110}$$

Computationally intensive integration over all the incoming directions is avoided by keeping the solid angle discretization symmetric on the *x*, *y* and *z* planes. The connection matrix associates one incoming direction l' to each mirrored direction on each wall cell.

The local incident radiation intensity is

$$U_{ijk} = \sum_{l=1}^{N_\Omega} I_{ijk}^l \delta\Omega^l \tag{4.111}$$

4.4 Solid Phase Model

4.4.1 Solid Surface and Interior Temperatures

A one dimensional heat transfer calculation is performed at each solid boundary cell for which the user has prescribed thermal properties. The solid can consist of multiple layers of materials. Each layer is partitioned into non-uniform cells, clustered near the front and back faces. The smallest cells are chosen based on the criteria

$$\delta x < S_s \sqrt{\frac{k_s}{\rho_s c_s}} \tag{4.112}$$

where S_s is a cell size factor defined by the user. By default, S_s is 1.0. Interior cells increase in size by a user-defined stretch factor when moving inwards from the surfaces. By default, the stretch factor is 2.0. The cell boundaries are located at points x_i. The temperature at the center of the ith cell is denoted $T_{s,i}$. The (temperature-dependent) thermal conductivity of the solid at the center of the ith cell is denoted $k_{s,i}$. The temperatures are updated in time using an implicit Crank-Nicolson scheme

$$\frac{T_{s,i}^{n+1} - T_{s,i}^n}{\delta t} = \frac{1}{2(\rho_s c_s)_i \delta x_i} \left(k_{s,i+\frac{1}{2}} \frac{T_{s,i+1}^n - T_{s,i}^n}{\delta x_{s,i+\frac{1}{2}}} - k_{s,i-\frac{1}{2}} \frac{T_{s,i}^n - T_{s,i-1}^n}{\delta x_{s,i-\frac{1}{2}}} + \right.$$
$$\left. k_{s,i+\frac{1}{2}} \frac{T_{s,i+1}^{n+1} - T_{s,i}^{n+1}}{\delta x_{i+\frac{1}{2}}} - k_{s,i-\frac{1}{2}} \frac{T_{s,i}^{n+1} - T_{s,i-1}^{n+1}}{\delta x_{i-\frac{1}{2}}} \right) + \frac{\dot{q}_s'''}{\rho_s c_s} \tag{4.113}$$

for $1 \leq i \leq N$. The width of each cell is δx_i. The distance from the center of cell i to the center of cell $i+1$ is $\delta x_{i+\frac{1}{2}}$. However, the material properties k_s, c_s, ρ_s and source terms $\dot{q}_s'''$ are updated in an explicit manner, using the temperature information from time step n.

The boundary condition is discretized

$$-k_{s,1} \frac{T_{s,1}^{n+1} - T_{s,0}^{n+1}}{\delta x_{\frac{1}{2}}} = \dot{q}_c''^{(n+1)} + \dot{q}_r''^{(n+1)} \tag{4.114}$$

The convective and radiative fluxes at the next time step are approximated

$$\dot{q}_c''^{(n+1)} \approx \dot{q}_c''^n - h \left(T_{s,\frac{1}{2}}^{n+1} - T_{s,\frac{1}{2}}^n \right) \tag{4.115}$$

$$\dot{q}_r''^{(n+1)} \approx \dot{q}_r''^n - 4\,\varepsilon\,\sigma\,T_{s,\frac{1}{2}}^{n3} \left(T_{s,\frac{1}{2}}^{n+1} - T_{s,\frac{1}{2}}^n \right) \tag{4.116}$$

The wall temperature is defined $T_w \equiv T_{s,\frac{1}{2}} = (T_{s,0} + T_{s,1})/2$.

The size and number of solid phase cells can change during the course of a calculation as solid material is converted to gas. The size of each cell is reduced such that the cell density remains equal to the density of the virgin material. If the cell size gets below a pre-defined threshold (1 μm), the cell is completely removed. Following cell shrinking or cell removal, the solid phase mesh is re-gridded and the mass and enthalpy values are interpolated from the old mesh to the new mesh.

4.4.2 Convective Heat Transfer to Solid Objects

In a DNS calculation where the boundary layer is resolved, the convective flux to the wall is given by

$$\dot{q}_c'' = -k \frac{T_{gas} - T_w}{\delta n/2} \tag{4.117}$$

where T_{gas} is the gas temperature in the center of the first gas-phase grid cell, T_w is the surface or "wall" temperature, δn is the size of a grid cell in the normal direction to the wall, and k is the temperature-dependent thermal conductivity of the gas mixture.

In an LES calculation, where the boundary layer is not resolved, an empirical heat transfer coefficient, h, is used:

$$\dot{q}''_c = h\left(T_{gas} - T_w\right) \quad \text{W/m}^2 \tag{4.118}$$

The heat transfer coefficient, h, is the maximum of its natural and forced empirical values:

$$h = \max\left(C|T_{gas} - T_w|^{\frac{1}{3}}, \frac{k_{air}}{L}0.037\,\text{Re}_L^{4/5}\text{Pr}^{1/3}\right) \quad \text{W/m}^2\text{/K} \tag{4.119}$$

C is an empirical coefficient (1.31 for vertical surface; 1.52 for horizontal), k_{air} is the thermal conductivity of air (not the "turbulent" value used in the LES solver), L is a length scale (assumed to be 1 m), the Reynolds number is based on the density and velocity of the gases in the middle of the first grid cell and the length scale L, and the Prandtl number is assumed to be 0.7.

4.4.3   Coupling the Gas and Solid Phase

Gas phase temperatures are defined at cell centers; solid surfaces lie at the interface of the bordering gas phase cell and a "ghost" cell inside the solid. As far as the gas phase calculation is concerned, the normal temperature gradient at the surface is expressed in terms of the temperature difference between the "gas" cell and the "ghost" cell. The solid surface temperature is not used directly in the gas phase calculation. Rather, the ghost cell temperature is used to couple the gas and solid phases. The ghost cell temperature has no physical meaning on its own. It is purely a numerical construct. It does not represent the temperature within the wall, but rather establishes a temperature gradient at the solid surface consistent with the empirical correlation. Only the difference between ghost and gas cell temperatures matters, for this defines the heat transfer to the wall.

In a DNS calculation, the solid surface temperature is assumed to be an average of the ghost cell temperature and the temperature of the first cell in the gas, thus the ghost cell temperature is defined

$$T_{ghost} = 2T_s - T_{gas} \tag{4.120}$$

For an LES calculation, the numerical expression for the heat lost to the boundary is equated with the empirical convective heat transfer

$$k_{\text{LES}}\frac{T_{gas} - T_{ghost}}{\delta n} - \bar{\rho}\,u_n\bar{c}_p(\bar{T})\,\bar{T} = h\left(T_{gas} - T_s\right) - \bar{\rho}\,u_n\,\bar{c}_p(T_s)\,T_s \tag{4.121}$$

where δn is the distance between the center of the ghost cell and the center of the gas cell, and the bar over the T and ρ indicate the average of the gas and ghost values:

$$\bar{T} = \frac{T_{gas} + T_{ghost}}{2} \quad ; \quad \bar{\rho} = \frac{\rho_{gas} + \rho^*_{ghost}}{2} \tag{4.122}$$

The specific heat is defined:

$$\bar{c}_p(T) = \frac{1}{T}\int_0^T c_p(T')\,dT' \tag{4.123}$$

Equation (4.121) is solved for T_{ghost}, so that when the conservation equations are updated, the amount of heat lost to the wall is equivalent to the empirical expression on the right hand side. Note that the asterisk in the equations above denotes that the value is taken from the previous time step.

At solid walls there is no transfer of mass, thus the boundary condition for the lth species at a wall is simply

$$Y_{l,ghost} = Y_{l,gas} \tag{4.124}$$

where the subscripts "ghost" and "gas" are the same as above since the mass fraction, like temperature, is defined at cell centers. At forced flow boundaries either the mass fraction $Y_{l,w}$ or the mass flux $\dot{m}_l''$ of species l may be prescribed. Then the ghost cell mass fraction can be derived because, as with temperature, the normal gradient of mass fraction is needed in the gas phase calculation. For cases where the mass fraction is prescribed

$$Y_{l,ghost} = 2Y_{l,w} - Y_{l,gas} \tag{4.125}$$

For cases where the mass flux is prescribed, the following equation must be solved iteratively

$$\dot{m}_l'' = u_n \frac{\rho_{ghost}Y_{l,ghost} + \rho_{gas}Y_{l,gas}}{2} - \rho D \frac{Y_{l,gas} - Y_{l,ghost}}{\delta n} \mp \frac{\delta t\, u_n^2}{2} \frac{\rho_{gas}Y_{l,gas} - \rho_{ghost}Y_{l,ghost}}{\delta n} \tag{4.126}$$

where $\dot{m}_l''$ is the mass flux of species l per unit area, u_n is the normal component of velocity at the wall pointing into the flow domain, and δn is the distance between the center of the ghost cell and the center of the gas cell. Notice that the last term on the right hand side is subtracted at the predictor step and added at the corrector step, consistent with the biased upwinding introduced earlier.

Once the temperature and species mass fractions have been defined in the ghost cell, the density in the ghost cell is computed from the equation of state

$$\rho_{ghost} = \frac{p_0}{\mathcal{R}\, T_{ghost}\, \sum_l (Y_{l,ghost}/W_l)} \tag{4.127}$$

4.4.4   Mass and Energy Transfer at Interpolated Mesh Boundaries

In simulations involving more than one numerical mesh, information has to be passed between meshes, even when the meshes are being processed by separate computers. If two meshes abut each other, and the mesh cells are aligned and the same size, then one mesh simply uses the density and species mass fractions of the adjacent mesh as the "ghost" cell values. However, in cases where the mesh cells are not the same size, the exchange of information must be done more carefully. Consider a case where two meshes meet:

Mesh 1   Mesh 2
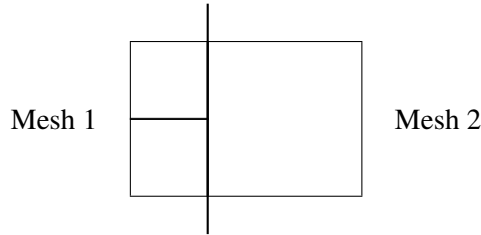
We want the total and species mass fluxes between meshes to be the same, or as close as possible. Let the density in cell $(1,j',k')$ of Mesh 2 be denoted $\rho_{1,j'k'}^{(2)}$. Assume that this cell abuts four cells in Mesh 1. The densities in the four abutting cells of Mesh 1 are denoted $\rho_{I,jk}^{(1)}$. Note that j and k are not the same as j' and k'. I is the number of cells in the x direction of Mesh 1. The ghost cell quantities in Mesh 1 have an i index of $I+1$. The ghost cell quantities in Mesh 2 have an i index of 0. We want to assert mass conservation at the mesh interface:

$$\sum_{j,k} u_{I,jk}^{(1)} \frac{\rho_{I+1,jk}^{(1)} + \rho_{I,jk}^{(1)}}{2} \delta y^{(1)} \delta z^{(1)} = u_{0,j'k'}^{(2)} \frac{\rho_{1,j'k'}^{(2)} + \rho_{0,j'k'}^{(2)}}{2} \delta y^{(2)} \delta z^{(2)} \tag{4.128}$$

When solving for $\rho^{(2)}_{0,j'k'}$, the ghost cell value for Mesh 2, we have to assume that the ghost cells values for Mesh 1 are simply linearly interpolated from the gas phase values of Mesh 1 and Mesh 2:

$$\rho^{(1)}_{I+1,jk} = \rho^{(1)}_{I,jk} + \frac{2\,\delta x^{(1)}}{\delta x^{(1)} + \delta x^{(2)}} \left(\rho^{(2)}_{1,j'k'} - \rho^{(1)}_{I,jk} \right) \tag{4.129}$$

Rearranging terms in Eq. (4.128) and using the expression for the ghost cells from Eq. (4.129), we get:

$$\rho^{(2)}_{0,j'k'} = -\rho^{(2)}_{1,j'k'} + \frac{1}{u^{(2)}_{0,j'k'}\,\delta y^{(2)}\,\delta z^{(2)}} \sum_{j,k} u^{(1)}_{1,jk}\,\delta y^{(1)}\,\delta z^{(1)} \left[2\rho^{(1)}_{I,jk} + \frac{2\,\delta x^{(1)}}{\delta x^{(1)} + \delta x^{(2)}} \left(\rho^{(2)}_{1,j'k'} - \rho^{(1)}_{I,jk} \right) \right] \tag{4.130}$$

4.5 Liquid Sprays

4.5.1 Particle movement

Lagrangian particles are can be introduced into the flow field as a means of visualization or simulation of droplets, aerosols, *etc.*. The position $\mathbf{x}_p$ of each particle is governed by the equations

$$\frac{d\mathbf{x}_p}{dt} = \mathbf{u} \tag{4.131}$$

The particle positions are updated according to the same predictor-corrector scheme that is applied to the other flow quantities. Briefly, the position $\mathbf{x}_p$ of a given particle is updated according to the two step scheme

$$\mathbf{x}_p^{(n+1)e} = \mathbf{x}_p^n + \delta t\, \overline{\mathbf{u}}^n \tag{4.132}$$

$$\mathbf{x}_p^{n+1} = \frac{1}{2}\left(\mathbf{x}_p^n + \mathbf{x}_p^{(n+1)e} + \delta t\, \overline{\mathbf{u}}^{(n+1)e}\right) \tag{4.133}$$

where the bar over the velocity vector indicates that the velocity of the fluid is linearly interpolated at the particle's position.

4.5.2 Interaction of Droplets and Radiation

The computation of χ_f for a similar but simpler situation has been derived in Ref. [70]. It can be shown that here χ_f becomes

$$\chi_f = \frac{1}{\delta\Omega^l} \int_0^{\mu^l} \int_0^{\mu^l} \int_{\mu_{d,0}}^{\mu_{d,\pi}} \frac{P_0(\theta_d)}{[(1-\mu^2)(1-\mu'^2)-(\mu_d-\mu\mu')^2]^{1/2}} \, d\mu_d \, d\mu \, d\mu' \tag{4.134}$$

where μ_d is a cosine of the scattering angle θ_d and $P_0(\theta_d)$ is a single droplet scattering phase function

$$P_0(\theta_d) = \frac{\lambda^2\left(|S_1(\theta_d)|^2 + |S_2(\theta_d)|^2\right)}{2\,C_s(r,\lambda)} \tag{4.135}$$

$S_1(\theta_d)$ and $S_2(\theta_d)$ are the scattering amplitudes, given by Mie-theory. The integration limit μ^l is a cosine of the polar angle defining the boundary of the symmetric control angle $\delta\Omega^l$

$$\mu^l = \cos(\theta^l) = 1 - \frac{2}{N_\Omega} \tag{4.136}$$

The limits of the innermost integral are

$$\mu_{d,0} = \mu\mu' + \sqrt{1-\mu^2}\sqrt{1-\mu'^2} \quad ; \quad \mu_{d,\pi} = \mu\mu' - \sqrt{1-\mu^2}\sqrt{1-\mu'^2} \tag{4.137}$$

When χ_f is integrated over the droplet size distribution to get an averaged value, it is multiplied by $C_s(r,\lambda)$. It is therefore $|S_1|^2 + |S_2|^2$, not $P_0(\theta_d)$, that is integrated. Physically, this means that intensities are added, not probabilities [54].

4.5.3 Heating and Evaporation of Liquid Droplets

The exchange of mass and energy between liquid droplets and the surrounding gases (or solid surfaces) is computed droplet by droplet. After the temperature of each droplet is computed, the appropriate amount of vaporized liquid is added to the given mesh cell, and the cell gas temperature is reduced slightly based on the energy lost to the droplet.

Equation (3.150) is solved semi-implicitly over the course of a gas phase time step as follows. Note that a few terms have been left out to make the algorithm more clear.

$$\frac{T_l^{n+1} - T_l^n}{\delta t} = \frac{1}{m_l c_l} \left[A h \left(T_g - \frac{T_l^{n+1} + T_l^n}{2} \right) - A h_m \rho \left(\frac{Y_l^{n+1} + Y_l^n}{2} - Y_g \right) h_v \right] \tag{4.138}$$

The equilibrium vapor mass fraction, Y_l^n, is a function of T_l^n via Eq. (3.151), and its value at the next time step is approximated via

$$Y_l^{n+1} \approx Y_l^n + \left(\frac{dY_l}{dT_l} \right)^n \left(T_l^{n+1} - T_l^n \right) \tag{4.139}$$

where the derivative of Y_l with respect to temperature is obtained via the chain rule:

$$\frac{dY_l}{dT_l} = \frac{dY_l}{dX_l} \frac{dX_l}{dT_l} = \frac{W_a/W_l}{(X_l(1 - W_a/W_l) + W_a/W_l)^2} \frac{h_v W_l}{\mathcal{R} T_l^2} \exp \left[\frac{h_v W_l}{\mathcal{R}} \left(\frac{1}{T_b} - \frac{1}{T_l} \right) \right] \tag{4.140}$$

The amount of evaporated liquid is given by

$$\delta m_l = \delta t A h_m \rho \left[Y_l^n + \frac{1}{2} \left(\frac{dY_l}{dT_l} \right)^n \left(T_l^{n+1} - T_l^n \right) \right] \tag{4.141}$$

The amount of heat extracted from the gas is

$$\delta q = \delta t A h \left(T_g - \frac{T_l^n + T_l^{n+1}}{2} \right) \tag{4.142}$$

Chapter 5

Conclusion

The equations and numerical algorithm described in this document form the core of an evolving fire model. As research into specific fire-related phenomena continues, the relevant parts of the model can be improved. Because the model was originally designed to predict the transport of heat and exhaust products from fires, it can be used reliably when the fire is prescribed and the numerical grid is sufficiently resolved to capture enough of the flow structure for the application at hand. It is the job of the user to determine what level of accuracy is needed.

Any user of the numerical model must be aware of the assumptions and approximations being employed. There are two issues for any potential user to consider before embarking on calculations. First, for both real and simulated fires, the growth of the fire is very sensitive to the thermal properties (conductivity, specific heat, density, burning rate, *etc.*) of the surrounding materials. Second, even if all the material properties are known, the physical phenomena of interest may not be simulated due to limitations in the model algorithms or numerical grid. Except for those few materials that have been studied to date at NIST, the user must supply the thermal properties of the materials, and then validate the performance of the model with experiments to ensure that the model has the necessary physics included. Only then can the model be expected to predict the outcome of fire scenarios that are similar to those that have actually been tested.

Bibliography

[1] American Society for Testing and Materials, West Conshohocken, Pennsylvania. *ASTM E 1355-04, Standard Guide for Evaluating the Predictive Capabilities of Deterministic Fire Models*, 2004. i, 5

[2] National Institute of Standards and Technology, Gaithersburg, Maryland, USA, and VTT Technical Research Centre of Finland, Espoo, Finland. *Fire Dynamics Simulator, Technical Reference Guide*, 5th edition, October 2007. NIST Special Publication 1018-5 (Four volume set). i, 11, 12

[3] K.B. McGrattan, S. Hostikka, and J.E. Floyd. Fire Dynamics Simulator (Version 5), User's Guide. NIST Special Publication 1019-5, National Institute of Standards and Technology, Gaithersburg, Maryland, October 2007. i, 7, 8, 11, 63

[4] H.C. Hottel. Stimulation of Fire Research in the United States After 1940 (A Historical Account). *Combustion Science and Technology*, 39:1–10, 1984. 1

[5] W.W. Jones. A Review of Compartment Fire Models. NBSIR 83-2684, National Bureau of Standards (now NIST), Gaithersburg, Maryland, 1983. 1

[6] J. Quintiere. A Perspective on Compartment Fire Growth. *Combustion Science and Technology*, 39:11–54, 1984. 1

[7] G.P. Forney and W.F. Moss. Analyzing and Exploiting Numerical Characteristics of Zone Fire Models. *Fire Science and Technology*, 14:49–60, 1994. 1

[8] S.V. Patankar. *Numerical Heat Transfer and Fluid Flow*. Hemisphere Publishing, New York, 1980. 2

[9] R.G. Rehm and H.R. Baum. The Equations of Motion for Thermally Driven, Buoyant Flows. *Journal of Research of the NBS*, 83:297–308, 1978. 2, 11, 15, 17, 49

[10] E.S. Oran and J.P. Boris. *Numerical Simulation of Reactive Flow*. Elsevier Science Publishing Company, New York, 1987. 2, 11

[11] V. Babrauskas. *Ignition Handbook*. Fire Science Publishers, Issaquah, Washington USA, 1st edition, 2003. Co-published by the Society of Fire Protection Engineers. 7

[12] G.P. Forney. Smokeview (Version 5), A Tool for Visualizing Fire Dynamics Simulation Data, Volume I: User's Guide. NIST Special Publication 1017-1, National Institute of Standards and Technology, Gaithersburg, Maryland, August 2007. 8, 11

[13] D.A. Anderson, J.C. Tannehill, and R.H. Pletcher. *Computational Fluid Mechanics and Heat Transfer*. Hemisphere Publishing Corporation, Philadelphia, Pennsylvania, 1984. 11, 15

[14] R. Peyret and T.D. Taylor. *Computational Methods for Fluid Flow*. Springer-Verlag, New York, 1983. 11

[15] J.H. Ferziger and M. Perić. *Computational Methods for Fluid Dynamics*. Springer-Verlag, Berlin, 2nd edition, 1999. 11

[16] R.W. Bilger. Turbulent Diffusion Flames. *Annual Review of Fluid Mechanics*, 21:101–135, 1989. 11

[17] J.P. Holman. *Heat Transfer*. McGraw-Hill, New York, 5th edition, 1989. 11, 38

[18] F.P. Incropera and D.P. De Witt. *Fundamentals of Heat and Mass Transfer*. John Wiley and Sons, New York, 4th edition, 1996. 11, 46

[19] R. Siegel and J. R. Howell. *Thermal Radiation Heat Transfer*. Taylor & Francis, New York, 4th edition, 2002. 11, 32, 37

[20] P.J. DiNenno, editor. *SFPE Handbook of Fire Protection Engineering*. National Fire Protection Association, Quincy, Massachusetts, 3rd edition, 2002. 11, 39, 40

[21] D. Drysdale. *An Introduction to Fire Dynamics*. John Wiley and Sons, New York, 2nd edition, 2002. 11

[22] J.G. Quintiere. *Principles of Fire Behavior*. Delmar Publishers, Albany, New York, 1998. 11

[23] K. Hill, J. Dreisbach, F. Joglar, B. Najafi, K. McGrattan, R. Peacock, and A. Hamins. Verification and Validation of Selected Fire Models for Nuclear Power Plant Applications. NUREG 1824, United States Nuclear Regulatory Commission, Washington, DC, 2007. 12

[24] H.R. Baum and K.B. McGrattan. Simulation of Large Industrial Outdoor Fires. In *Fire Safety Science – Proceedings of the Sixth International Symposium*. International Association for Fire Safety Science, 2000. 17

[25] H. Werner and H. Wengle. Large-eddy simulation of turbulent flow over and around a cube in a plate channel. In *8th Symposium on Turbulent Shear Flows*, pages 155–168, 1991. 20

[26] Stephen B. Pope. *Turbulent Flows*. Cambridge, 2000. 20

[27] H. Tennekes and J. L. Lumley. *A First Course in Turbulence*. MIT Press, 1972. 20

[28] M. V. Zagarola and A. J. Smits. Scaling of the mean velocity profile for turbulent pipe flow. *Phys. Rev. Lett.*, 78:239–242, 1997. 20

[29] Pierre Sagaut. *Large Eddy Simulation for Incompressible Flows*. Springer, 2001. 20, 101

[30] S.B. Pope. Ten questions concerning the large-eddy simulation of turbulent flows. *New Journal of Physics*, 6:1–24, 2004. 23

[31] J. Smagorinsky. General Circulation Experiments with the Primitive Equations. I. The Basic Experiment. *Monthly Weather Review*, 91(3):99–164, March 1963. 23

[32] J.W. Deardorff. Numerical Investigation of Neutral and Unstable Planetary Boundary Layers. *Journal of Atmospheric Sciences*, 29:91–115, 1972. 23

[33] M. Germano, U. Piomelli, P. Moin, and W.H. Cabot. A Dynamic Subgrid-Scale Eddy Viscosity Model. *Physics of Fluids A*, 3(7):1760–1765, 1991. 23

[34] D.K. Lilly. A Proposed Modification of the Germano Subgrid-Scale Closure Method. *Physics of Fluids A*, 4(3):633–635, 1992. 23

[35] H.R. Baum, K.B. McGrattan, and R.G. Rehm. Three Dimensional Simulations of Fire Plume Dynamics. *Journal of the Heat Transfer Society of Japan*, 35(139):45–52, 1997. 23

[36] B.E. Poling, J.M. Prausnitz, and J.P. O'Connell. *The Properties of Gases and Liquids*. McGraw-Hill, New York, 5th edition, 2000. 24, 57

[37] I.K. Puri and K. Seshadri. Extinction of Diffusion Flames Burning Diluted Methane and Diluted Propane in Diluted Air. *Combustion and Flame*, 65:137–150, 1986. 31

[38] C.K. Westbrook and F.L. Dryer. Simplified Reaction Mechanisms for the Oxidation of Hydrocarbon Fuels in Flames. *Combustion Science and Technology*, 27:31–43, 1981. 31

[39] W. Grosshandler. RadCal: A Narrow Band Model for Radiation Calculations in a Combustion Environment. NIST Technical Note TN 1402, National Institute of Standards and Technology, Gaithersburg, Maryland, 1993. 33

[40] K. Prasad, C. Li, K. Kailasanath, C. Ndubizu, R. Ananth, and P.A. Tatem. Numerical modelling of methanol liquid pool fires. *Combustion Theory and Modelling*, 3:743–768, 1999. 37

[41] G. Heskestad and R.G. Bill. Quantification of Thermal Responsiveness of Automatic Sprinklers Including Conduction Effects. *Fire Safety Journal*, 14:113–125, 1988. 39

[42] P. Ruffino and M. di Marzo. Temperature and Volumetric Fraction Measurements in a Hot Gas Laden with Water Droplets. *Journal of Heat Transfer*, 125(2):356–364, April 2003. 39

[43] P. Ruffino and M. di Marzo. The Effect of Evaporative Cooling on the Activation Time of Fire Sprinklers. In *Fire Safety Science – Proceedings of the Seventh International Symposium*, pages 481–492. International Association for Fire Safety Science, 2002. 39

[44] F. Gavelli, P. Ruffino, G. Anderson, and M. di Marzo. Effect of Minute Water Droplets on a Simulated Sprinkler Link Thermal Response. NIST GCR 99-776, National Institute of Standards and Technology, Gaithersburg, Maryland, July 1999. 39

[45] T. Cleary, A. Chernovsky, W. Grosshandler, and M. Anderson. Particulate Entry Lag in Spot-Type Smoke Detectors. In *Fire Safety Science – Proceedings of the Sixth International Symposium*, pages 779–790. International Association for Fire Safety Science, 1999. 40

[46] G.W. Mulholland and C. Croarkin. Specific Extinction Coefficient of Flame Generated Smoke. *Fire and Materials*, 24:227–230, 2000. 40

[47] R.J. Roby, S.J. Olenick, W. Zhang, D.J. Carpenter, M.S. Klassen, and J.L. Torero. A Smoke Detector Algorithm for Large Eddy Simulation Modeling. NIST GCR 07-911, National Institute of Standards and Technology, Gaithersburg, Maryland, 2007. 40

[48] T.S. Chan. Measurements of Water Density and Droplet Size Distributions of Selected ESFR Sprinklers. *Journal of Fire Protection Engineering*, 6(2):79–87, 1994. 42

[49] H.Z. Yu. Investigation of Spray Patterns of Selected Sprinklers with the FMRC Drop Size Measuring System. In *Fire Safety Science – Proceedings of the First International Symposium*, pages 1165–1176. International Association For Fire Safety Science, 1986. 42

[50] A. Hamins and K.B. McGrattan. Reduced-Scale Experiments to Characterize the Suppression of Rack Storage Commodity Fires. NISTIR 6439, National Institute of Standards and Technology, Gaithersburg, Maryland, 1999. 44, 47

[51] A. Hamins and K.B. McGrattan. Reduced-Scale Experiments on the Water Suppression of a Rack-Storage Commodity Fire for Calibration of a CFD Fire Model. In *Fire Safety Science – Proceedings of the Seventh International Symposium*, pages 457–468. International Association for Fire Safety Science, 2002. 44, 47

[52] T. Ravigururajan and M. Beltran. A Model for Attenuation of Fire Radiation Through Water Droplets. *Fire Safety Journal*, 15:171–181, 1989. 44

[53] A. Tuntomo, C. Tien, and S. Park. Optical Constants of Liquid Hydrocarbon Fuels. *Combustion Science and Technology*, 84:133–140, 1992. 44

[54] W.J. Wiscombe. Improved Mie Scattering Algorithms. *Applied Optics*, 19(9):1505–1509, 1980. 46, 73

[55] G.M. Hale and M.R. Querry. Optical constants of water in the 200 nm to 200 *mu*m wavelength region. *Applied Optics*, 12(3):555–563, 1973. 46

[56] N. Cheremisinoff. *Encyclopedia of Fluid Mechanics, Volume 3: Gas-Liquid Flows*. Gulf Publishing Company, Houston, Texas, 1986. 46

[57] H.Z. Yu, J.L. Lee, and H.C. Kung. Suppression of Rack-Storage Fires by Water. In *Fire Safety Science – Proceedings of the Fourth International Symposium*, pages 901–912. International Association For Fire Safety Science, 1994. 47

[58] K.B. McGrattan, R.G. Rehm, and H.R. Baum. Fire-Driven Flows in Enclosures. *Journal of Computational Physics*, 110(2):285–291, 1994. 49

[59] H.R. Baum, O.A. Ezekoye, K.B. McGrattan, and R.G. Rehm. Mathematical Modeling and Computer Simulation of Fire Phenomenon. *Theoretical and Computational Fluid Dynamics*, 6:125–139, 1994. 49

[60] G. Continillo, F.M Denaro, and F.S. Marra. Accuracy and Stability Analysis of Time-Integrated Schemes for Advection-Diffusion-Reaction Equations. In *Seventh International Conference on Numerical Combustion*, page 99, 1998. 52

[61] Jr. M.W. Chase. NIST-JANAF Thermochemical Tables, Fourth Edition. *J. Physical and Chemical Reference Data*, Monograph No. 9, 1998. 54

[62] W. Zhang, N. Ryder, R.J. Roby, and D. Carpenter. Modeling of the Combustion in Compartment Fires Using Large Eddy Simulation Approach. In *Proceedings of the 2001 Fall Technical Meeting, Eastern States Section*. Combustion Institute, Pittsburgh, Pennsylvania, December 2001. 57

[63] R.A. Sweet. Direct Methods for the Solution of Poisson's Equation on a Staggered Grid. *Journal of Computational Physics*, 12:422–428, 1973. 59

[64] V. Raman, H. Pitsch, and R.O. Fox. Hybrid large-eddy simulation/Lagrangian filtered-density-function approach for simulating turbulent combustion. *Combustion and Flame*, 143:56–78, 2005. 63

[65] L. Orloff and J. De Ris. Froude Modeling of Pool Fires. In *Proceedings of the Nineteenth Symposium (International) on Combustion*, pages 885–895. Combustion Institute, Pittsburgh, Pennsylvania, 1982. 63

[66] G.D. Raithby and E.H. Chui. A Finite-Volume Method for Predicting Radiant Heat Transfer in Enclosures with Participating Media. *Journal of Heat Transfer*, 112(2):415–423, 1990. 65

[67] S. Hostikka. Development of fire simulation models for radiative heat transfer and probabilistic risk assessment. VTT Publications 683, VTT Technical Research Centre of Finland, Espoo, Finland, 2008. 65

[68] J.Y. Murthy and S.R. Mathur. Radiative Heat Transfer in Axisymmetric Geometries Using an Unstructured Finite-Volume Method. *Numerical Heat Transfer, Part B*, 33:397–416, 1998. 66

[69] S.H. Kim and K.Y. Huh. Assessment of The Finite-Volume Method and The Discrete Ordinate Method for Radiative Heat Transfer In a Three-Dimensional Rectangular Enclosure. *Numerical Heat Transfer, Part B*, 35:85–112, 1999. 67

[70] W. Yang, T. Parker, H.D. Ladouceur, and R.J. Kee. The Interaction of Thermal Radiation and Water Mist in Fire Suppression. *Fire Safety Journal*, 39:41–66, 2004. 73

[71] M. Herrmann, G. Blanquart, and V. Raman. Flux corrected finite-volume scheme for preserving boundedness in large-eddy simulations. AIAA Paper 2005-25009, 2005. 105

[72] P.L. Roe. Characteristics-based schemes for the euler equations. *Ann. Rev. Fluid Mech.*, 18:337, 1986. 105

[73] G. Zhou. *Numerical simulations of physical discontinuities in single and multi-fluid flows for arbitrary Mach numbers*. PhD thesis, Chalmers Univ. of Tech., Goteborg, Sweden, 1995. 105

[74] E.F. Toro. *Riemann Solvers and Numerical Methods for Fluid Dynamics: A Practical Introduction*. Springer, 2nd edition, 1999. 105

Appendix A

Nomenclature

A_s	droplet surface area
$A_{\alpha\beta}$	pre-exponential factor for solid phase Arrhenius reaction
B	pre-exponential factor for gas phase Arrhenius reaction
C	Sprinkler C-Factor
C_D	drag coefficient
C_s	Smagorinsky constant (LES)
c_s	Solid material specific heat
c_p	constant pressure specific heat
D	diffusion coefficient
d_m	median volumetric droplet diameter
E	activation energy
$\mathbf{f}_b$	external force vector (excluding gravity)
g	acceleration of gravity
$\mathbf{g}$	gravity vector, normally $(0,0,-g)$
$\mathcal{H}$	total pressure divided by the density
$H_{r,\alpha\beta}$	heat of reaction for a solid phase reaction
h	enthalpy; heat transfer coefficient
h_α	enthalpy of species α
h_α^0	heat of formation of species α
I	radiation intensity
I_b	radiation blackbody intensity
k	thermal conductivity; suppression decay factor
$\dot{m}'''_{b,\alpha}$	mass production rate of species α by evaporating droplets/particles
$\dot{m}''_f$	fuel mass flux
$\dot{m}'''_\alpha$	mass production rate of species α per unit volume
$\dot{m}''_w$	water mass flux
m''_w	water mass per unit area
Nu	Nusselt number
Pr	Prandtl number
p	pressure
$\bar{p}_0$	atmospheric pressure profile
$\bar{p}_m$	background pressure of mth pressure zone
$\tilde{p}$	pressure perturbation
$\dot{\mathbf{q}}''$	heat flux vector

$\dot{q}'''$	heat release rate per unit volume
$\dot{q}_r''$	radiative flux to a solid surface
$\dot{q}_c''$	convective flux to a solid surface
$\dot{Q}$	total heat release rate
Q^*	characteristic fire size
$\mathcal{R}$	universal gas constant
Re	Reynolds number
r_d	droplet radius
$r_{\alpha\beta}$	solid phase reaction rate
RTI	Response Time Index of sprinkler
$\mathbf{s}$	unit vector in direction of radiation intensity
Sc	Schmidt number
Sh	Sherwood number
S_α	solid component production rate
T	temperature
t	time
U	integrated radiant intensity
$\mathbf{u} = (u, v, w)$	velocity vector
W_α	molecular weight of gas species α
$\overline{W}$	molecular weight of the gas mixture
We	Weber number
$\mathbf{x} = (x, y, z)$	position vector
X_α	volume fraction of species α
Y_α	mass fraction of species α
$Y_{O_2}^\infty$	mass fraction of oxygen in the ambient
Y_F^I	mass fraction of fuel in the fuel stream
y_s	soot yield
Z	mixture fraction
Z_f	stoichiometric value of the mixture fraction
γ	ratio of specific heats; Rosin-Rammler exponent
ΔH	heat of combustion
ΔH_{O_2}	energy released per unit mass oxygen consumed
δ	wall thickness
ε	dissipation rate
κ	absorption coefficient
μ	dynamic viscosity
ν_α	stoichiometric coefficient, species α
ν_s	yield of solid residue in solid phase reaction
$\nu_{g,\gamma}$	yield of gaseous species γ in solid phase reaction
ρ	density
τ_{ij}	viscous stress tensor
χ_r	radiative loss fraction
σ	Stefan-Boltzmann constant; constant in droplet size distribution; surface tension
σ_d	droplet scattering coefficient
σ_s	scattering coefficient
$\omega = (\omega_x, \omega_y, \omega_z)$	vorticity vector

Appendix B

Derivation of the Velocity Divergence Constraint

In this appendix we derive the divergence of the velocity field as presented in Eq. (3.14). Note that the constitutive relationships presented here for the mass diffusion and thermal heat fluxes are valid for direct numerical simulations (i.e., well-resolved calculations). The minor modifications required of the transport coefficients for large-eddy simulation are presented in Section 3.1.6. We start the derivation by rearranging the continuity equation. Next, we differentiate the equation of state to reveal the relationship between transport equations for mass and energy. We then show how the transport equations may be combined to yield the velocity divergence constraint. In the last section we present the final result in FDS notation.

Continuity Equation

Let ρ denote the fluid mass density; let $\mathbf{u} = [u, v, w]^T$ denote the fluid mass-average velocity; and let $\dot{m}_b'''$ denote a bulk source of mass per unit volume (which may come from the evaporation of water droplets, for example). The continuity equation may be rearranged to yield the following divergence constraint on the velocity

$$\nabla \cdot \mathbf{u} = \frac{1}{\rho} \left(\dot{m}_b''' - \frac{\mathrm{D}\rho}{\mathrm{D}t} \right) \tag{B.1}$$

where $\mathrm{D}(\ )/\mathrm{D}t \equiv \partial(\ )/\partial t + \mathbf{u} \cdot \nabla(\ )$ is the material derivative.

Equation of State

We consider the transport of n_s species mass fractions Y_α for $\alpha = \{1, \ldots, n_s\}$, $n_s - 1$ of which are independent. The molecular weight of a given species is denoted W_α and the molecular weight of the mixture, $\overline{W}$, is given by

$$\overline{W} = \left(\sum_\alpha \frac{Y_\alpha}{W_\alpha} \right)^{-1} \tag{B.2}$$

where as a shorthand notation, which is used throughout this document, we write $\sum_\alpha$ for $\sum_{\alpha=1}^{n_s}$. Let $\overline{p}_i(\mathbf{x}, t)$ denote the hydrostatic pressure in the ith zone of the domain, which in general we take to be a function of space and time. In practice, however, $\overline{p}_i = \overline{p}_i(t)$ for closed (i.e., sealed or pressurized) domains and $\overline{p}_i = \overline{p}_i(z)$, where z represents the coordinate aligned with the gravity vector, for large, open domains (e.g., forest fires large enough to interact with the stratified atmosphere). The divergence constraint derived below

is based on the ideal gas equation of state (EOS), which, for low-Mach flows, we write as

$$\overline{p}_i = \frac{\rho \mathcal{R} T}{\overline{W}} \tag{B.3}$$

where $\mathcal{R} = 8.3145$ kJ/(kmol K) is the gas law constant.

Differentiating the EOS (B.3) we obtain

$$\frac{D\overline{p}_i}{Dt} = \rho \mathcal{R} T \frac{D}{Dt}\left(\frac{1}{\overline{W}}\right) + \frac{\rho \mathcal{R}}{\overline{W}}\frac{DT}{Dt} + \frac{\mathcal{R}T}{\overline{W}}\frac{D\rho}{Dt} \tag{B.4}$$

which rearranges to

$$\frac{D\rho}{Dt} = \frac{\overline{W}}{\mathcal{R}T}\frac{D\overline{p}_i}{Dt} - \rho\overline{W}\frac{D}{Dt}\left(\frac{1}{\overline{W}}\right) - \frac{\rho}{T}\frac{DT}{Dt} \tag{B.5}$$

Species Transport Equation

The species transport equation plays a role in both the second and third terms on the RHS of (B.5). Including the bulk mass source, the evolution of species mass fractions is governed by

$$\frac{\partial (\rho Y_\alpha)}{\partial t} + \nabla \cdot (\rho Y_\alpha \mathbf{u}) = -\nabla \cdot \mathbf{J}_\alpha + \dot{m}_\alpha''' + \dot{m}_{b,\alpha}''' \tag{B.6}$$

where $\mathbf{J}_\alpha$ is the diffusive mass flux vector for species α (relative to the mass-average velocity), $\dot{m}_\alpha'''$ is the chemical mass production rate of α per unit volume [kg-α produced /(sec m^3)], and $\dot{m}_{b,\alpha}'''$ is the bulk mass source of α per unit volume [kg-α introduced /(sec m^3)]. Note that

$$\sum_\alpha \dot{m}_{b,\alpha}''' = \dot{m}_b''' \tag{B.7}$$

and

$$\sum_\alpha \dot{m}_\alpha''' = 0 \tag{B.8}$$

Additionally, by construction, the ith component of the species diffusive fluxes sum to zero,

$$\sum_\alpha J_{\alpha,i} = 0 \tag{B.9}$$

Thus, as must be the case, summing (B.6) over α yields the continuity equation.

It is convenient to work in terms of the material derivative of the mass fraction. Care must be exercised in obtaining this expression because the continuity equation is of a non-standard form. Expanding (B.6) we obtain

$$\rho\frac{\partial Y_\alpha}{\partial t} + Y_\alpha\frac{\partial \rho}{\partial t} + \rho\mathbf{u}\cdot\nabla Y_\alpha + Y_\alpha\nabla\cdot(\rho\mathbf{u}) = -\nabla\cdot\mathbf{J}_\alpha + \dot{m}_\alpha''' + \dot{m}_{b,\alpha}''',$$

$$\rho\frac{DY_\alpha}{Dt} + Y_\alpha\underbrace{\left[\frac{\partial\rho}{\partial t} + \nabla\cdot(\rho\mathbf{u})\right]}_{\dot{m}_b'''} = \tag{B.10}$$

Thus, the material derivative of the mass fraction can be written as

$$\frac{DY_\alpha}{Dt} = \frac{1}{\rho}\left(\dot{m}_\alpha''' + \dot{m}_{b,\alpha}''' - Y_\alpha\dot{m}_b''' - \nabla\cdot\mathbf{J}_\alpha\right) = \frac{1}{\rho}\left(\dot{m}_\alpha''' + \dot{m}_b'''[Y_{b,\alpha} - Y_\alpha] - \nabla\cdot\mathbf{J}_\alpha\right) \tag{B.11}$$

86

where in the second step we use the identity $\dot{m}'''_{b,\alpha} = Y_\alpha \dot{m}'''_b$ with $Y_{b,\alpha}$ being the mass fraction of α in the bulk prior to its introduction into the fluid mixture.

Utilizing (B.2) and (B.11) we obtain

$$\begin{aligned}
\frac{D}{Dt}\left(\frac{1}{\overline{\overline{W}}}\right) &= \frac{D}{Dt}\left(\sum_\alpha \frac{Y_\alpha}{W_\alpha}\right), \\
&= \sum_\alpha \frac{1}{W_\alpha}\frac{DY_\alpha}{Dt}, \\
&= \frac{1}{\rho}\sum_\alpha \frac{1}{W_\alpha}\left(\dot{m}'''_\alpha + \dot{m}'''_b[Y_{b,\alpha} - Y_\alpha] - \nabla \cdot \mathbf{J}_\alpha\right),
\end{aligned} \tag{B.12}$$

which is needed in the second term on the RHS of (B.5).

Enthalpy Transport Equation

The specific sensible enthalpy of species α relative to reference temperature T_0 is

$$h_{s,\alpha}(T) = \int_{T_0}^T c_{p,\alpha}(T')\,dT', \tag{B.13}$$

where the specific heat of α is

$$c_{p,\alpha} \equiv \frac{\partial h_{s,\alpha}}{\partial T}. \tag{B.14}$$

The specific sensible enthalpy of the mixture is then given by

$$h_s(\mathbf{Y},T) = \sum_\alpha Y_\alpha h_{s,\alpha}(T). \tag{B.15}$$

Neglecting viscous heating and the effect of the fluctuating pressure on dilation work (both assumptions are valid for low-Mach flows), the transport equation for the sensible enthalpy is

$$\rho\frac{Dh_s}{Dt} = -\sum_\alpha \Delta h^0_\alpha \dot{m}'''_\alpha + \frac{D\overline{p}_i}{Dt} - \nabla \cdot \dot{\mathbf{q}}'' - \dot{q}'''_b + \dot{m}'''_b(h_{s,b} - h_s) + \frac{\dot{m}'''_b}{2}|\mathbf{u}_b - \mathbf{u}|^2 \tag{B.16}$$

where Δh^0_α is the heat of formation of α at reference temperature T_0, $h_{s,b}$ is the specific sensible enthalpy of the bulk mass source, $\dot{q}'''_b$ is a volumetric heat sink due to convective heat transfer to the bulk phase, and $\dot{\mathbf{q}}''$ is the heat flux vector which contains contributions from conduction, molecular diffusion of sensible enthalpy, and radiation,

$$\dot{\mathbf{q}}'' = -k\nabla T + \sum_\alpha h_{s,\alpha}\mathbf{J}_\alpha + \dot{\mathbf{q}}''_r \tag{B.17}$$

Here k is the thermal conductivity of the mixture and $\dot{\mathbf{q}}''_r$ is the radiant heat flux. The last term in (B.16) accounts for the kinetic energy associated with the instantaneous mixing of the bulk and gas-phase momentum.

Relating Enthalpy, Temperature, and Species

Using the chain rule of calculus, we may expand the derivative of the sensible enthalpy $h_s(\mathbf{Y},T)$ to obtain

$$\frac{Dh_s}{Dt} = \left(\frac{\partial h_s}{\partial T}\right)\frac{DT}{Dt} + \sum_\alpha \left(\frac{\partial h_s}{\partial Y_\alpha}\right)\frac{DY_\alpha}{Dt} \tag{B.18}$$

87

Note that since $h_s = \sum_\alpha Y_\alpha h_{s,\alpha}$ we have

$$\frac{\partial h_s}{\partial Y_\alpha} = \frac{\partial}{\partial Y_\alpha} \sum_\beta (Y_\beta h_{s,\beta}) = \sum_\beta h_{s,\beta}\, \delta_{\alpha\beta} = h_{s,\alpha} \tag{B.19}$$

where $\delta_{\alpha\beta}$ is the Kronecker delta. Also,

$$\frac{\partial h_s}{\partial T} = \frac{\partial}{\partial T} \sum_\alpha Y_\alpha h_{s,\alpha} = \sum_\alpha Y_\alpha \left(\frac{\partial h_{s,\alpha}}{\partial T} \right) = \sum_\alpha Y_\alpha c_{p,\alpha} \equiv c_p \tag{B.20}$$

defining the specific heat of the mixture. Thus, by rearranging (B.18) and utilizing (B.19) and (B.20) we obtain

$$\frac{\mathrm{D}T}{\mathrm{D}t} = \frac{1}{c_p} \left[\frac{\mathrm{D}h_s}{\mathrm{D}t} - \sum_\alpha h_{s,\alpha} \frac{\mathrm{D}Y_\alpha}{\mathrm{D}t} \right] \tag{B.21}$$

Utilizing (B.11) and (B.16) in (B.21) yields

$$\begin{aligned}
\frac{\mathrm{D}T}{\mathrm{D}t} = {} & \frac{1}{\rho c_p} \left[-\sum_\alpha \Delta h_\alpha^0 \dot{m}_\alpha''' + \frac{\mathrm{D}\overline{p}_i}{\mathrm{D}t} - \nabla \cdot \dot{\mathbf{q}}'' - \dot{q}_b''' + \dot{m}_b'''(h_{s,b} - h_s) + \frac{\dot{m}_b'''}{2} |\mathbf{u}_b - \mathbf{u}|^2 \right. \\
& \left. - \sum_\alpha h_{s,\alpha} \left\{ \dot{m}_\alpha''' + \dot{m}_b'''[Y_{b,\alpha} - Y_\alpha] - \nabla \cdot \mathbf{J}_\alpha \right\} \right]
\end{aligned} \tag{B.22}$$

Note that $\sum_\alpha h_{s,\alpha} \dot{m}_b'''[Y_{b,\alpha} - Y_\alpha] - \dot{m}_b'''(h_{s,b} - h_s) = \dot{m}_b''' \sum_\alpha Y_{b,\alpha}(h_{s,\alpha}[T_b] - h_{s,\alpha}[T]) \approx \dot{m}_b''' \sum_\alpha Y_{b,\alpha} c_{p,\alpha}(T_b - T)$, leaving

$$\frac{\mathrm{D}T}{\mathrm{D}t} = \frac{1}{\rho c_p} \left[\frac{\mathrm{D}\overline{p}_i}{\mathrm{D}t} - \nabla \cdot \dot{\mathbf{q}}'' - \dot{q}_b''' - \sum_\alpha \Delta h_\alpha^0 \dot{m}_\alpha''' - \sum_\alpha h_{s,\alpha} \left(\dot{m}_\alpha''' - \nabla \cdot \mathbf{J}_\alpha \right) + \dot{m}_b''' \sum_\alpha Y_{b,\alpha} c_{p,\alpha}(T_b - T) + \frac{\dot{m}_b'''}{2} |\mathbf{u}_b - \mathbf{u}|^2 \right].$$

Assembling Terms

We now have all the pieces we need to construct the divergence constraint which we introduced in Eq. (B.1). Using (B.5) in (B.1) we obtain

$$\begin{aligned}
\nabla \cdot \mathbf{u} = {} & \frac{1}{\rho} \left(\dot{m}_b''' - \left[\frac{\overline{W}}{\mathcal{R}T} \frac{\mathrm{D}\overline{p}_i}{\mathrm{D}t} - \rho \overline{W} \frac{\mathrm{D}}{\mathrm{D}t} \left(\frac{1}{\overline{W}} \right) - \frac{\rho}{T} \frac{\mathrm{D}T}{\mathrm{D}t} \right] \right) \\
= {} & \frac{1}{\rho} \dot{m}_b''' - \frac{1}{\overline{p}_i} \frac{\mathrm{D}\overline{p}_i}{\mathrm{D}t} + \overline{W} \frac{\mathrm{D}}{\mathrm{D}t} \left(\frac{1}{\overline{W}} \right) + \frac{1}{T} \frac{\mathrm{D}T}{\mathrm{D}t}
\end{aligned} \tag{B.23}$$

where in the second step the EOS (B.3) is used to simplify the second term on the RHS. Using (B.12) and (B.23) in (B.23) yields

$$\begin{aligned}
\nabla \cdot \mathbf{u} = {} & \frac{1}{\rho} \dot{m}_b''' - \frac{1}{\overline{p}_i} \frac{\mathrm{D}\overline{p}_i}{\mathrm{D}t} + \overline{W} \left[\frac{1}{\rho} \sum_\alpha \frac{1}{W_\alpha} \left\{ \dot{m}_\alpha''' + \dot{m}_b'''[Y_{b,\alpha} - Y_\alpha] - \nabla \cdot \mathbf{J}_\alpha \right\} \right] \\
& + \frac{1}{T} \left[\frac{1}{\rho c_p} \left\{ \frac{\mathrm{D}\overline{p}_i}{\mathrm{D}t} - \nabla \cdot \dot{\mathbf{q}}'' - \dot{q}_b''' - \sum_\alpha \Delta h_\alpha^0 \dot{m}_\alpha''' - \sum_\alpha h_{s,\alpha} \left(\dot{m}_\alpha''' - \nabla \cdot \mathbf{J}_\alpha \right) + \dot{m}_b''' \sum_\alpha Y_{b,\alpha} c_{p,\alpha}(T_b - T) + \frac{\dot{m}_b'''}{2} |\mathbf{u}_b - \mathbf{u}|^2 \right\} \right].
\end{aligned} \tag{B.24}$$

Note that $\overline{W} \sum_\alpha (Y_\alpha / W_\alpha) = 1$ and also $\overline{W} \sum_\alpha (Y_{b,\alpha} / W_\alpha) = \overline{W} / \overline{W}_b$, where $\overline{W}_b$ is the molecular weight of the bulk mixture prior to its introduction into the fluid mixture. Equation (B.24) thus simplifies to

$$
\begin{aligned}
\nabla \cdot \mathbf{u} \;=\;& \left(\frac{1}{\rho c_p T} - \frac{1}{\overline{p}_i} \right) \frac{\mathrm{D}\overline{p}_i}{\mathrm{D}t} + \frac{1}{\rho} \left[\dot{m}_b''' \frac{\overline{W}}{\overline{W}_b} + \overline{W} \sum_\alpha \frac{1}{W_\alpha} \left\{ \dot{m}_\alpha''' - \nabla \cdot \mathbf{J}_\alpha \right\} \right] \\
&+ \frac{1}{\rho c_p T} \left[-\sum_\alpha \Delta h_\alpha^0 \dot{m}_\alpha''' - \sum_\alpha h_{s,\alpha} \left(\dot{m}_\alpha''' - \nabla \cdot \mathbf{J}_\alpha \right) - \nabla \cdot \dot{\mathbf{q}}'' - \dot{q}_b''' + \dot{m}_b''' \sum_\alpha Y_{b,\alpha} c_{p,\alpha} (T_b - T) + \frac{\dot{m}_b'''}{2} |\mathbf{u}_b - \mathbf{u}|^2 \right] .
\end{aligned}
$$
(B.25)

FDS Notation

The following relationships are used to rearrange (B.25) into the form shown in the FDS Technical Reference Guide. We employ the binary form of Fick's law using mixture-averaged diffusivities D_α as a constitutive relation for the diffusive flux,

$$
\mathbf{J}_\alpha = -\rho D_\alpha \nabla Y_\alpha .
$$
(B.26)

Note that summation is not implied over repeated suffixes. The heat release rate per unit volume is defined by

$$
\dot{q}''' \equiv -\sum_\alpha \dot{m}_\alpha''' \Delta h_\alpha^0 .
$$
(B.27)

Taking the z direction to be aligned with the gravity vector we have $\partial \overline{p}_i / \partial z = -\rho_i g$, where $g = 9.8$ m/s^2 and ρ_i is a specified background density for the ith zone. Thus, the material derivative of the background pressure may be written as

$$
\frac{\mathrm{D}\overline{p}_i}{\mathrm{D}t} = \frac{\partial \overline{p}_i}{\partial t} - w\rho_i g .
$$
(B.28)

Hence, utilizing (B.26), (B.27), and (B.28), and noting $1/(\rho T) = \mathcal{R}/(\overline{W}\overline{p}_i)$ from the EOS, for the ith zone we may write the divergence (B.25) as

$$
\nabla \cdot \mathbf{u} = \mathcal{D} - \mathcal{P} \frac{\partial \overline{p}_i}{\partial t}
$$
(B.29)

where

$$
\mathcal{P} = \frac{1}{\overline{p}_i} \left(1 - \frac{\overline{p}_i}{\rho c_p T} \right) = \frac{1}{\overline{p}_i} \left(1 - \frac{\mathcal{R}}{\overline{W} c_p} \right)
$$
(B.30)

and

$$
\begin{aligned}
\mathcal{D} \;=\;& \frac{\dot{m}_b'''}{\rho} \frac{\overline{W}}{\overline{W}_b} + \frac{\overline{W}}{\rho} \sum_\alpha \nabla \cdot (\rho D_\alpha \nabla [Y_\alpha / W_\alpha]) + \frac{1}{\rho} \sum_\alpha \left(\frac{\overline{W}}{W_\alpha} - \frac{h_{s,\alpha}}{c_p T} \right) \dot{m}_\alpha''' + \mathcal{P} w \rho_i g \\
&+ \frac{\mathcal{R}}{\overline{W} c_p \overline{p}_i} \left[\dot{q}''' - \dot{q}_b''' - \nabla \cdot \dot{\mathbf{q}}'' - \sum_\alpha h_{s,\alpha} \nabla \cdot \rho D_\alpha \nabla Y_\alpha + \dot{m}_b''' \sum_\alpha Y_{b,\alpha} c_{p,\alpha} (T_b - T) + \frac{\dot{m}_b'''}{2} |\mathbf{u}_b - \mathbf{u}|^2 \right]
\end{aligned}
$$
(B.31)

Equations (B.30) and (B.31) correspond to (3.15) and (3.16) in the FDS Tech Guide. Though, note that at present the bulk kinetic energy term is not included in the code.

A brief remark on the of the sensible enthalpy $h_{s,\alpha}$ vs. the [chemical + sensible] enthalpy $h_\alpha = \Delta h_\alpha^0 + h_{s,\alpha}$: The definition of the heat flux vector $\dot{\mathbf{q}}''$ can be a key source of confusion. When transporting the sensible enthalpy only, as we are doing here, the heat flux vector does not account for the molecular transport of the chemical enthalpy (the enthalpy of formation). If we were working in terms of the [chemical + sensible] enthalpy we would not have a "heat of reaction" $\dot{q}'''$, the heat flux vector would account for the transport of both the chemical and the sensible enthalpies, and the sensible enthalpies in (B.31) would be replaced by the [chemical + sensible] enthalpy h_α.

Appendix C

Domain Decomposition Strategy

The time advancement scheme for multiple meshes involves averaging of the velocity components at a patch boundary in order to maintain stability. It is extremely important to note that – because of the staggered grid storage arrangement – two values of the numerical solution for the velocity exist at a given point on a mesh interface. Consider meshes m (left) and om (right) which are joined side by side in the x direction. The staggered u velocity components are indexed from $\{0:nx\}$ (in the x direction) on a given mesh. The values $u^{(m)}_{nx,jk}$ and $u^{(om)}_{0,jk}$ therefore live at the same physical location, but are advanced separately (and by different processors) during the course of the algorithm. In the ideal circumstance these velocities are identical, as is the case if the PDEs (4.73) and (4.74) are enforced at the mesh interface. To improve the speed of our parallel algorithm, our strategy is instead to keep the difference between these values small while still enforcing global volume conservation. Our strategy recovers the ideal case in the limit $\delta t \rightarrow 0$. In fact, for reasonable time steps (CFL ≈ 0.5) we observe that the difference in the coincident velocities is negligible. While the primitive velocity components are indeed unique to a given mesh, for each mesh we may define the discrete "patch-averaged" field $\bar{\mathbf{u}}$ which includes ghost cell data and is identical at all overlapping mesh points. To do this we simply average the coincident values of the velocity components at the mesh interfaces and inject the ghost cell values from the neighboring mesh. For instance, considering the same side-by-side meshes m and om as before,

$$\bar{u}^{(m)}_{ijk} \equiv \begin{cases} u^{(m)}_{ijk} & \text{for} \quad 0 < i < nx \\ \frac{1}{2}\left[u^{(m)}_{nx,jk} + u^{(om)}_{0,jk} \right] & \text{for} \quad i = nx \\ u^{(om)}_{1,jk} & \text{for} \quad i = nx+1 \end{cases} \tag{C.1}$$

for all patch boundary cells j and k; nx identifies the right-most boundary cells for mesh m. Here, for simplicity, we are only considering the case in which the cell sizes are equivalent for the adjoining meshes (coarse-fine mesh interfaces are currently handled by the code, but details will be documented at a later date). The values of $\bar{u}^{(m)}$ for the index ranges not considered in (C.1) depend on the specific boundary conditions for the other faces of mesh m. The same ideas are used to define the patch-averaged fields for $\bar{v}$ and $\bar{w}$.

To see how the new patch-averaged fields are used, consider the predictor step in the time advancement, which may now be written as

$$\mathbf{u}^{(n+1)e} = \bar{\mathbf{u}}^n - \delta t \left[\mathbf{F}(\rho^n, \bar{\mathbf{u}}^n) + \nabla \mathcal{H}'^{(n+1)e} + \nabla \mathcal{H}''^{(n+1)e} \right]. \tag{C.2}$$

Note that (C.2) updates a $\bar{\mathbf{u}}$ field to a $\mathbf{u}$ field. Though this is perfectly legitimate, we should be aware of the following issues. First, the patch-averaging procedure is slightly dissipative. But as long as we

are accurate, this numerical dissipation is minimal and acceptable (much smaller than physical [molecular, viscous] dissipation). Second, we must now think of the time update in terms of a projection scheme in order to repair the damage made to the divergence by the averaging procedure (after the averaging procedure, the divergence for mesh boundary cells no longer exactly matches the divergence obtained from the equation of state). In practical terms, this means that the Poisson equation for the pressure fluctuation (in the predictor step) is given by

$$\nabla^2 \mathcal{H}'^{(n+1)e} = - \left[\frac{(\nabla \cdot \mathbf{u})^{(n+1)e} - (\nabla \cdot \bar{\mathbf{u}})^n}{\delta t} \right] - \mathbf{F}(\rho^n, \bar{\mathbf{u}}^n). \tag{C.3}$$

In (C.3), note that $\mathbf{F}$ is computed using the patch-averaged velocity field. Further, only the $(\nabla \cdot \mathbf{u})^{(n+1)e}$ term is obtained from the equation of state (3.14). The divergence of the patch-averaged field, $(\nabla \cdot \bar{\mathbf{u}})^n$, is obtained by explicitly applying the discrete divergence operator to $\bar{\mathbf{u}}^n$. Similarly, in the corrector Poisson equation analogous to (4.11), only the $(\nabla \cdot \mathbf{u})^{n+1}$ term is obtained from the equation of state; $(\nabla \cdot \bar{\mathbf{u}})^{(n+1)e}$ and $(\nabla \cdot \bar{\mathbf{u}})^n$ are obtained explicitly:

$$\nabla^2 \mathcal{H}'^{n+1} = - \left[\frac{2(\nabla \cdot \mathbf{u})^{n+1} - (\nabla \cdot \bar{\mathbf{u}})^{(n+1)e} - (\nabla \cdot \bar{\mathbf{u}})^n}{\delta t} \right] - \mathbf{F}(\rho^{(n+1)e}, \bar{\mathbf{u}}^{(n+1)e}). \tag{C.4}$$

Finally, the velocity corrector step is

$$\mathbf{u}^{n+1} = \frac{1}{2} \left[\bar{\mathbf{u}}^n + \bar{\mathbf{u}}^{(n+1)e} - \delta t \left(\mathbf{F}[\rho^{(n+1)e}, \bar{\mathbf{u}}^{(n+1)e}] + \nabla \mathcal{H}'^{n+1} + \nabla \mathcal{H}''^{n+1} \right) \right]. \tag{C.5}$$

The benefit of the averaging procedure is that $\mathbf{F}$ is now the same on each mesh for a given location along a mesh interface, since all force terms are determined using the patch-averaged field. This also means that stress tensors computed at a mesh interface (which are buried in $\mathbf{F}$) are symmetric; this symmetry is a requirement for angular momentum conservation. Thus, the patch-averaging procedure prevents the production of spurious vorticity at mesh interfaces.

It remains that we specify the boundary conditions for the Poisson and Laplace equations. At the interface of two adjoining meshes we apply the following Dirichlet boundary condition for the pressure fluctuation (again, mesh m is to the left of mesh om in this example):

$$\mathcal{H}'^{(m)}_{nx+\frac{1}{2},jk} = \mathcal{H}'^{(om)}_{1-\frac{1}{2},jk} = \frac{1}{2} \left[\mathcal{H}'^{(m),*}_{nx,jk} + \mathcal{H}'^{(om),*}_{1,jk} \right]. \tag{C.6}$$

Again, the asterisk denotes the most recent value. Note that the pressure boundary values are identical for each mesh at the interface. To a good approximation, this boundary condition maintains continuity of the pressure field from mesh to mesh without invoking an iterative procedure.

Pressure Correction

In its current state of development, the so-called pressure correction (PC) scheme (invoked by setting `PRESSURE_CORRECTION=.TRUE.` on the `MISC` line) is delicate and should be used with caution by practitioners who understand the scheme and are aware of its limitations. PC can be problematic if used "incorrectly". It is hard to know *a priori* exactly what this means. It is a bit like asking the question of whether or not grid resolution is sufficient (if the calculation gives the correct answer, then it is). With regard to the use of PC, as is usually the case with in CFD, the correctness mainly has to do with mesh setup, and, of course, it is up to the user to create the proper grid arrangement. PC works well if the flow is predominantly normal to the mesh interface. It works poorly (because the system is ill-conditioned) if the flow is predominantly parallel to the mesh interface. With an understanding of the scheme, this will make some intuitive

sense: as we will see below, the scheme sets a *uniform* pressure gradient across the mesh interface to correct the totality of the volume imbalance. If the flow is parallel to the interface, the volume error is likely to be an average of several small fluctuations going both ways across the interface, yet PC pushes everything in one direction. This "correction" may act as a nonphysical forcing and generate inaccurate, even unstable, solutions. With these words of caution in place, let us now examine how the scheme works.

To get the boundary conditions for the Laplace equation, we first need to solve a coarse-grained discrete Poisson equation over the global domain treating the individual meshes as coarse cells in an unstructured grid. This is much like the strategy adopted by zone and lumped parameter models, which assume that each compartment in a building has a uniform pressure found by solving a system of equations based on mass balances at compartment boundaries. A key difference here is that we have a *much* better initial estimate for the intermesh volume flow rates at the beginning of each time step. It is important to appreciate, therefore, that the accuracy of this method does not degenerate to that of a zone model.

To see how we develop the Neumann condition for the pressure correction, in this section imagine for a moment that on each mesh we are updating the fine-grained velocity field with an explicit Euler step from time t^k to $t^{k+1} = t^k + \delta t$ assuming $\mathcal{H}'' = 0$. Denote this intermediate velocity field $\mathbf{u}^+$. Thus,

$$\mathbf{u}^+ = \bar{\mathbf{u}}^k - \delta t \left[\mathbf{F}(\rho^k, \bar{\mathbf{u}}^k) + \nabla \mathcal{H}'^{k+1} \right]. \tag{C.7}$$

Now, because our guess for the mesh boundary value for $\mathcal{H}'^{k+1}$ is not perfect, the new field $\mathbf{u}^+$ does not conserve volume. That is, at an interface between meshes m and n with surface area $S_{m,n}$ we have

$$\int_{S_{m,n}} \mathbf{u}_m^+ \cdot \mathbf{n}_m \, dS \neq \int_{S_{m,n}} \mathbf{u}_n^+ \cdot \mathbf{n}_m \, dS, \tag{C.8}$$

where $\mathbf{n}_m$ is the unit vector normal to the surface pointing outward from mesh m. Consider now that there exists an interface velocity $\mathbf{U}_{m,n}^{k+1}$ such that

$$\mathbf{U}_{m,n}^{k+1} = \frac{1}{S_{m,n}} \int_{S_{m,n}} \mathbf{u}_m^{k+1} \, dS = \frac{1}{S_{m,n}} \int_{S_{m,n}} \mathbf{u}_n^{k+1} \, dS. \tag{C.9}$$

Also, note that we may rewrite (C.2) as

$$\mathbf{u}_m^{k+1} = \mathbf{u}_m^+ - \delta t \nabla \mathcal{H}_m''^{k+1}. \tag{C.10}$$

Substituting (C.10) into (C.9) yields

$$\mathbf{U}_{m,n}^{k+1} = \frac{1}{S_{m,n}} \int_{S_{m,n}} \left[\mathbf{u}_m^+ - \delta t \nabla \mathcal{H}_m''^{k+1} \right] dS. \tag{C.11}$$

Taking $\nabla \mathcal{H}''$ to be uniform along a mesh interface, (C.11) may be rearranged to give

$$\nabla \mathcal{H}_m''^{k+1} \Big|_{m,n} = \frac{1}{\delta t} \left[\frac{1}{S_{m,n}} \int_{S_{m,n}} \mathbf{u}_m^+ dS - \mathbf{U}_{m,n}^{k+1} \right]. \tag{C.12}$$

Equation (C.12) provides the pressure correction Neumann boundary condition for mesh m at the interface between meshes m and n that enforces volume conservation, i.e., forces the constraint (C.9) to be true. It remains that we determine the intermesh velocity $\mathbf{U}_{m,n}^{k+1}$.

The intermesh velocity is obtained from a projection method on the unstructured coarse mesh. After the update (C.7) we have two slightly different estimates of the intermesh velocity provided by the adjoining meshes. The average of these estimates, denoted $\bar{\mathbf{U}}_{m,n}^+$, is used as the initial guess in the coarse projection,

$$\bar{\mathbf{U}}_{m,n}^+ \equiv \frac{1}{2S_{m,n}} \int_{S_{m,n}} \left[\mathbf{u}_m^+ + \mathbf{u}_n^+ \right] dS. \tag{C.13}$$

This value is then projected to satisfy global divergence constraints as follows,

$$\mathbf{U}_{m,n}^{k+1} = \bar{\mathbf{U}}_{m,n}^{+} - \delta t \nabla_{m,n} \bar{\mathcal{H}}, \tag{C.14}$$

where $\nabla_{m,n}$ is the coarse-grid gradient operator (discussed below) and $\bar{\mathcal{H}}$ is the coarse-grid pressure (yet to be determined). Multiplying (C.14) by the surface area and unit normal pointing from mesh m to mesh n and then summing over all surfaces n which interface with m via interpolated (i.e., adjoining mesh), inlet, or open boundaries (denoted $n \in m$), we form a linear system for $\bar{\mathcal{H}}$,

$$\sum_{n \in m} S_{m,n} \mathbf{U}_{m,n}^{k+1} \cdot \mathbf{n}_m = \sum_{n \in m} S_{m,n} \bar{\mathbf{U}}_{m,n}^{+} \cdot \mathbf{n}_m - \delta t \sum_{n \in m} S_{m,n} \nabla_{m,n} \bar{\mathcal{H}} \cdot \mathbf{n}_m. \tag{C.15}$$

For a given mesh m, the left-hand-side of (C.15) may be determined by integrating $\mathbf{u}_m^{+}$ around the boundary $\partial\Omega_m$ of domain Ω_m. Using Gauss' theorem and Eqs. (C.10) and (4.74), the following are equivalent,

$$\sum_{n \in m} S_{m,n} \mathbf{U}_{m,n}^{k+1} \cdot \mathbf{n}_m = \int_{\partial\Omega_m} \mathbf{u}_m^{+} \cdot \mathbf{n}_m \, dS = \int_{\partial\Omega_m} \mathbf{u}_m^{k+1} \cdot \mathbf{n}_m \, dS = \int_{\Omega_m} \nabla \cdot \mathbf{u}_m^{k+1} \, dV. \tag{C.16}$$

Using (C.13) and (C.16), our linear system (C.15) may be written as

$$-\sum_{n \in m} S_{m,n} \nabla_{m,n} \bar{\mathcal{H}} \cdot \mathbf{n}_m = \frac{1}{\delta t} \left[\int_{\partial\Omega_m} \mathbf{u}_m^{+} \cdot \mathbf{n}_m \, dS - \sum_{n \in m} S_{m,n} \bar{\mathbf{U}}_{m,n}^{+} \cdot \mathbf{n}_m \right], \tag{C.17}$$

$$= \frac{1}{2\delta t} \int_{\partial\Omega_m} \left[\mathbf{u}_m^{+} - \mathbf{u}_n^{+} \right] \cdot \mathbf{n}_m \, dS. \tag{C.18}$$

The coarse-grid pressure gradient is approximated using a central difference, taking the coarse pressure to reside at the mesh centroid. Let $L_{m,n}$ correspond to the length scale of mesh m in the direction normal to the m–n interface ($L_{n,m}$ is the length scale of mesh n). Then the coarse gradient of the pressure is taken to be

$$-\nabla_{m,n} \bar{\mathcal{H}} \cdot \mathbf{n}_m = \frac{\bar{\mathcal{H}}_m - \bar{\mathcal{H}}_n}{\frac{1}{2}(L_{m,n} + L_{n,m})}. \tag{C.19}$$

We now translate (C.18) into matrix notation. Let M denote the number of meshes in the calculation, and let $\mathbf{x} = [\bar{\mathcal{H}}_1, \bar{\mathcal{H}}_2, ..., \bar{\mathcal{H}}_M]^T$ denote the solution vector for the mesh pressure. The linear system may be written as $\mathbf{Ax} = \mathbf{b}$, where $\mathbf{A}$ is an $M \times M$ symmetric, positive-definite matrix (which is sparse for large M) with diagonal elements

$$A(m,m) = \sum_{n \in m} \frac{2S_{m,n}}{L_{m,n} + L_{n,m}}, \tag{C.20}$$

and off-diagonal elements

$$A(m,n) = -\frac{2S_{m,n}}{L_{m,n} + L_{n,m}}. \tag{C.21}$$

The source $\mathbf{b}$ is an M-vector with elements

$$b(m) = \frac{1}{2\delta t} \int_{\partial\Omega_m} \left[\mathbf{u}_m^{+} - \mathbf{u}_n^{+} \right] \cdot \mathbf{n}_m \, dS. \tag{C.22}$$

At an inlet boundary the coarse pressure gradient is set to zero, i.e. $\bar{\mathcal{H}}_n = \bar{\mathcal{H}}_m$, and the diagonal and off-diagonal elements of the $\mathbf{A}$ matrix are modified accordingly. At an open boundary, at present we simply set $\bar{\mathcal{H}}_n = 0$ and $L_{n,m} = 0$, which is not entirely consistent with the fine-scale open boundary condition, but seems to be robust and has the added benefit that no modification of the source vector $\mathbf{b}$ is required.

At the present time, the coarse linear system is inverted directly using LU decomposition for simplicity. The **A** matrix is computed for the initial time step and for any subsequent changes in geometry during the simulation. We then perform the LU decomposition and store the inverse of **A**. In subsequent calls to the pressure correction routine, the coarse grid linear solve is obtained from a simple matrix-vector multiply which is $O(M^2)$ operations.

With the coarse-grid pressure $\bar{\mathcal{H}}$ now determined, we can perform the projection (C.14) and hence compute the Neumann condition for the Laplace equation for $\mathcal{H}''$ via (C.12). With a similar procedure used in the corrector step, the resulting velocity fields from the predictor (C.2) and corrector (C.5) steps obey the local divergence constraints and conserve volume from mesh to mesh.

Appendix D

A Simple Model of Flame Extinction

Frederick W. Mowrer, Department of Fire Protection Engineering, University of Maryland

A diffusion flame immersed in a vitiated atmosphere will extinguish before consuming all the available oxygen from the atmosphere. The classic example of this behavior is a candle burning within an inverted jar. This same concept has been applied within FDS to determine the conditions under which the local ambient oxygen concentration will no longer support a diffusion flame. In this appendix, the critical adiabatic flame temperature concept is used to estimate the local ambient oxygen concentration at which extinction will occur.

Consider a control volume characterized by a bulk temperature, T_m, a mass, m, an average specific heat, $\overline{c_p}$, and an oxygen mass fraction, Y_{O_2}. Complete combustion of the oxygen within the control volume would release a quantity of energy given by:

$$Q = mY_{O_2}\left(\frac{\Delta H}{r_{O_2}}\right) \tag{D.1}$$

where $\Delta H/r_{O_2}$ has a relatively constant value of approximately 13100 kJ/kg for most fuels of interest for fire applications.[1] Under adiabatic conditions, the energy released by combustion of the available oxygen within the control volume would raise the bulk temperature of the gases within the control volume by an amount equal to:

$$Q = m\overline{c_p}(T_f - T_m) \tag{D.2}$$

The average specific heat of the gases within the control volume can be calculated based on the composition of the combustion products as:

$$\overline{c_p} = \frac{1}{(T_f - T_m)}\sum_{\alpha}\int_{T_m}^{T_f} c_{p,\alpha}(T)\,dT \tag{D.3}$$

To simplify the analysis, the combustion products are assumed to have an average specific heat of 1.2 kJ/kg/K over the temperature range of interest, a value similar to that of nitrogen, the primary component of the products. The relationship between the oxygen mass fraction within the control volume and the adiabatic temperature rise of the control volume is evaluated by equating Eqs. (D.1) and (D.2):

$$Y_{O_2} = \frac{\overline{c_p}(T_f - T_m)}{\Delta H/r_{O_2}} \tag{D.4}$$

If the critical adiabatic flame temperature is assumed to have a constant value of approximately 1700 K for hydrocarbon diffusion flames, as suggested by Beyler,[2] then the relationship between the limiting oxygen

---

[1]C. Huggett, "Estimation of the Rate of Heat Release by Means of Oxygen Consumption," *Fire and Materials*, Vol. 12, pp. 61-65, 1980.

[2]C. Beyler, "Flammability Limits of Premixed and Diffusion Flames," *SFPE Handbook of Fire Protection Engineering* (3rd Ed.), National Fire Protection Association, Quincy, MA, 2003.

mass fraction and the bulk temperature of a control volume is given by:

$$Y_{O_2,lim} = \frac{\overline{c_p}(T_{f,lim} - T_m)}{\Delta H / r_{O_2}} \approx \frac{1.2\,(1700 - T_m)}{13100} \tag{D.5}$$

The relationship represented by Eq. (D.5) is shown *qualitatively* in Fig. 3.4. For a control volume at a temperature of 300 K, i.e., near room temperature, the limiting oxygen mass fraction would evaluate to $Y_{O_2,lim} = 0.128$. This value is consistent with the measurements of Morehart, Zukoski and Kubota,[3] who measured the oxygen concentration at extinction of flames by dilution of air with combustion products. They found that flames self-extinguished at oxygen concentrations of 12.4 % to 14.3 %. Note that their results are expressed as volume, not mass, fractions. Beyler's chapter in the SFPE Handbook references other researchers who measured oxygen concentrations at extinction ranging from 12 % to 15 %. The default value in FDS is 15 %.

---

[3]Morehart, J., Zukoski, E., and Kubota, T., "Characteristics of Large Diffusion Flames Burning in a Vitiated Atmosphere," *Third International Symposium on Fire Safety Science*, Elsevier Science Publishers, pp. 575-583, 1991.

Appendix E

Derivation of the Werner Wengle Wall Model

R. McDermott, BFRL

To obtain (3.26) we take the first off-wall value of the streamwise velocity to be

$$\tilde{u} = \frac{1}{\Delta z} \int_0^{\Delta z} u(z)\, \mathrm{d}z, \tag{E.1}$$

and then substitute the WW profile for $u(z)$ and integrate.

Let z_m denote the dimensional distance from wall where $z^+ = 11.81$. Equation (E.1) becomes

$$
\begin{aligned}
\tilde{u} &= \frac{1}{\Delta z}\left[\int_0^{z_m} u(z)\,\mathrm{d}z + \int_{z_m}^{\Delta z} u(z)\,\mathrm{d}z \right], \\
&= \frac{1}{\Delta z}\left[\int_0^{z_m} u^+ u^*\,\mathrm{d}z + \int_{z_m}^{\Delta z} u^+ u^*\,\mathrm{d}z \right], \\
&= \frac{1}{\Delta z}\left[\int_0^{z_m} z^+ u^*\,\mathrm{d}z + \int_{z_m}^{\Delta z} A(z^+)^B u^*\,\mathrm{d}z \right], \\
&= \frac{1}{\Delta z}\left[\int_0^{z_m} \frac{z}{\ell} u^*\,\mathrm{d}z + \int_{z_m}^{\Delta z} A\left(\frac{z}{\ell}\right)^B u^*\,\mathrm{d}z \right], \\
&= \frac{1}{\Delta z}\left[\int_0^{z_m} \frac{z\bar{\rho}u^*}{\bar{\mu}} u^*\,\mathrm{d}z + \int_{z_m}^{\Delta z} A\left(\frac{z\bar{\rho}u^*}{\bar{\mu}}\right)^B u^*\,\mathrm{d}z \right], \\
&= \frac{1}{\Delta z}\left[\underbrace{\int_0^{z_m} \frac{\tau_w}{\bar{\mu}} z\,\mathrm{d}z}_{I} + \underbrace{\int_{z_m}^{\Delta z} A\left(\frac{\bar{\rho}}{\bar{\mu}}\right)^B \left(\frac{\tau_w}{\bar{\rho}}\right)^{\frac{1+B}{2}} z^B\,\mathrm{d}z}_{II} \right].
\end{aligned}
\tag{E.2}
$$

We will integrate I and II separately. First, however, we must find a way to eliminate the unknown z_m. To do this we equate (3.23) and (3.24) at the point where the viscous and power law regions intersect, i.e.

$z^+ = 11.81 \equiv z_m^+ = z_m \bar{\rho} u^* / \bar{\mu}.$

$$
\begin{aligned}
u^+(z_m^+) = A(z_m^+)^B &= z_m^+ \\
A &= (z_m^+)^{1-B} \\
A^{\frac{1}{1-B}} &= z_m^+ = \frac{z_m \bar{\rho} u^*}{\bar{\mu}} \\
z_m &= \frac{\bar{\mu} A^{\frac{1}{1-B}}}{\bar{\rho} u^*} \\
z_m &= \frac{(\bar{\mu}/\bar{\rho}) A^{\frac{1}{1-B}}}{\sqrt{\tau_w/\bar{\rho}}} \,.
\end{aligned}
\tag{E.3}
$$

We now have z_m in terms of τ_w and otherwise known values.

Integrating section *I* of (E.2) we find

$$
\begin{aligned}
\int_0^{z_m} \frac{\tau_w}{\bar{\mu}} z \, dz &= \frac{\tau_w}{2\bar{\mu}} \left[z^2\right]_0^{z_m} \\
&= \frac{\tau_w}{2\bar{\mu}} z_m^2 \\
&= \frac{\tau_w}{2\bar{\mu}} \frac{(\bar{\mu}/\bar{\rho})^2 A^{\frac{2}{1-B}}}{\tau_w/\bar{\rho}} \\
&= \frac{\bar{\mu} A^{\frac{2}{1-B}}}{2\bar{\rho}} \,.
\end{aligned}
\tag{E.4}
$$

Integrating section *II* yields

$$
\begin{aligned}
\int_{z_m}^{\Delta z} A \left(\frac{\bar{\rho}}{\bar{\mu}}\right)^B \left(\frac{\tau_w}{\bar{\rho}}\right)^{\frac{1+B}{2}} z^B \, dz &= \left\{ A \left(\frac{\bar{\rho}}{\bar{\mu}}\right)^B \left(\frac{\tau_w}{\bar{\rho}}\right)^{\frac{1+B}{2}} \right\} \frac{1}{1+B} \left[z^{1+B}\right]_{z_m}^{\Delta z} \\
&= \{ \ \} \frac{1}{1+B} \left[\Delta z^{1+B} - z_m^{1+B}\right] \\
&= \{ \ \} \frac{1}{1+B} \left[\Delta z^{1+B} - \left(\frac{(\bar{\mu}/\bar{\rho}) A^{\frac{1}{1-B}}}{\sqrt{\tau_w/\bar{\rho}}}\right)^{1+B}\right] \\
&= \left\{ \frac{A}{1+B} \left(\frac{\bar{\rho}}{\bar{\mu}}\right)^B \left(\frac{\tau_w}{\bar{\rho}}\right)^{\frac{1+B}{2}} \right\} \left[\Delta z^{1+B} - \frac{(\bar{\mu}/\bar{\rho})^{1+B} A^{\frac{1+B}{1-B}}}{\left(\frac{\tau_w}{\bar{\rho}}\right)^{\frac{1+B}{2}}}\right] \\
&= \frac{A}{1+B} \left(\frac{\bar{\rho}}{\bar{\mu}}\right)^B \left(\frac{\tau_w}{\bar{\rho}}\right)^{\frac{1+B}{2}} \Delta z^{1+B} - \frac{(\bar{\mu}/\bar{\rho})}{1+B} A^{\frac{2}{1-B}} \,.
\end{aligned}
\tag{E.5}
$$

Plugging (E.4) and (E.5) back into (E.2) gives

$$
\begin{aligned}
\tilde{u} &= \frac{1}{\Delta z} \left[\frac{\bar{\mu} A^{\frac{2}{1-B}}}{2\bar{\rho}} + \frac{A}{1+B} \left(\frac{\bar{\rho}}{\bar{\mu}}\right)^B \left(\frac{\tau_w}{\bar{\rho}}\right)^{\frac{1+B}{2}} \Delta z^{1+B} - \frac{(\bar{\mu}/\bar{\rho})}{1+B} A^{\frac{2}{1-B}}\right] \\
&= \frac{1}{2} \left(\frac{\bar{\mu}}{\bar{\rho}\Delta z}\right) A^{\frac{2}{1-B}} - \frac{1}{1+B} \left(\frac{\bar{\mu}}{\bar{\rho}\Delta z}\right) A^{\frac{2}{1-B}} + \frac{A}{1+B} \left(\frac{\bar{\rho}\Delta z}{\bar{\mu}}\right)^B \left(\frac{\tau_w}{\bar{\rho}}\right)^{\frac{1+B}{2}} \,.
\end{aligned}
\tag{E.6}
$$

100

Rearranging for τ_w we find

$$
\begin{aligned}
\left(\frac{\tau_w}{\bar{\rho}}\right)^{\frac{1+B}{2}} &= \frac{1+B}{A}\left(\frac{\bar{\mu}}{\bar{\rho}\Delta z}\right)^{B}\left[\left(\frac{1}{1+B}-\frac{1}{2}\right)\left(\frac{\bar{\mu}}{\bar{\rho}\Delta z}\right)A^{\frac{2}{1-B}}+\tilde{U}\right] \\
&= \frac{1-B}{2}A^{\frac{1+B}{1-B}}\left(\frac{\bar{\mu}}{\bar{\rho}\Delta z}\right)^{1+B}+\frac{1+B}{A}\left(\frac{\bar{\mu}}{\bar{\rho}\Delta z}\right)^{B}\tilde{U} \\
\tau_w &= \bar{\rho}\left[\frac{1-B}{2}A^{\frac{1+B}{1-B}}\left(\frac{\bar{\mu}}{\bar{\rho}\Delta z}\right)^{1+B}+\frac{1+B}{A}\left(\frac{\bar{\mu}}{\bar{\rho}\Delta z}\right)^{B}\tilde{u}\right]^{\frac{2}{1+B}}, \quad\quad\quad \text{(E.7)}
\end{aligned}
$$

which corresponds to Eq. (9.46) in [29].

Appendix F

The Inflow/Outflow Pressure Boundary Condition

R. McDermott, BFRL

Outflow: The outflow condition is quite simple. Let $q \equiv |\mathbf{u}|$. By definition, $\mathcal{H} = \frac{1}{2}q^2 + \frac{\tilde{p}}{\rho_\infty}$. The pressure $\tilde{p}$ is set to $\tilde{p}_{ext}$ by the user (`DYNAMIC_PRESSURE`, 0 by default).

Inflow: When fluid is entering the domain at an `OPEN` vent we make the assumption that Bernoulli holds (i.e. inviscid, steady, incompressible) and that the fluid element on the boundary has accelerated from the state $\{\tilde{p}_1, \rho_1, q_1\}$ along a streamline:

$$\tilde{p}_1 + \tfrac{1}{2}\rho_1 q_1^2 = \tilde{p}_2 + \tfrac{1}{2}\rho_2 q_2^2 \tag{F.1}$$

Let's say the fluid has kinetic energy $\frac{1}{2}\rho_1 q_1$ at point 1 with ambient pressure $\tilde{p}_1 = \tilde{p}_{ext}$ and accelerates to q_2 at point 2 which is on an inflow boundary. Substituting the definition of $\mathcal{H}$ for point 2 we obtain

$$\tilde{p}_{ext} + \tfrac{1}{2}\rho_1 q_1^2 = \rho_\infty(\mathcal{H}_2 - \tfrac{1}{2}q_2^2) + \tfrac{1}{2}\rho_2 q_2^2 \tag{F.2}$$

which rearranges to

$$\mathcal{H}_2 = \underbrace{\frac{\tilde{p}_{ext}}{\rho_\infty}}_{\mathcal{H}_{ext}} + \underbrace{\frac{1}{2}q_1\frac{\rho_1}{\rho_\infty}}_{\mathcal{H}_0} + \frac{1}{2}q_2\left(1 - \frac{\rho_2}{\rho_\infty}\right) \tag{F.3}$$

The density ρ_2 (denoted ρ_w in Eq. (4.70)) is taken as the average density between the gas-phase and ghost cells adjacent to the boundary.

Appendix G

Scalar Boundedness Correction

R. McDermott, BFRL

Second-order central differencing of the advection term in the scalar transport equation leads to dispersion errors (spurious wiggles) and these errors, if left untreated, can lead to scalar fields which are physically not realizable, e.g., negative densities. To prevent this, FDS employs a boundedness correction to the scalar fields after the explicit transport step. The correction, which we describe below, acts locally and effectively adds the minimum amount of diffusion necessary to prevent boundedness violations. It is stressed that this correction does not make the scalar transport scheme total variation diminishing (TVD); it only serves to correct for boundedness. Similar schemes are employed by others (see e.g. [71]).

Optionally, the user may invoke TVD transport schemes by setting `FLUX_LIMITER={1-4}` on `MISC` (1=first-order upwinding (Godunov), 2=Superbee [72] (recommended for LES), 3=MINMOD, 4=CHARM [73] (recommended for DNS)). These TVD schemes are applied during the transport step and each can be shown to be TVD in 1D under certain CFL constraints. However, except for Godunov's scheme, the TVD proofs do not extend to 3D [74]. Still, these schemes do a much better job than pure central differencing at mitigating dispersion error. If the TVD schemes are applied, FDS still runs through the boundedness check in case any small violations are not prevented by the flux limiter.

A simple case

For simplicity we start by considering a minimum boundedness violation for density in 1D. That is, somewhere we have $\rho < \rho_{min}$. Let ρ_i^* denote the resulting density from the explicit transport step for cell i with volume V_i. Our goal is to find a correction $\delta\rho_i$ which:

(a) satisfies boundedness, $\rho_i = \rho_i^* + \delta\rho_i \geq \rho_{min}$ for all i

(b) conserves mass, $\sum_i \delta\rho_i V_i = 0$

(c) minimizes data variation, $\sum_i |\delta\rho_i|$ is minimized (i.e., we change the field as little as possible)

As mentioned, the basic idea is to apply a linear smoothing operator $\mathcal{L}$ to the density field in regions where boundedness violations have occurred. So, the correction may be viewed as an explicit diffusion step applied to the uncorrected field with diffusion coefficient c:

$$\rho = \rho^* + c\mathcal{L}\rho^* \tag{G.1}$$

To make matters simple, let us envision for the moment that the density in cell i is negative but that the densities in cells $i-1$ and $i+1$ are both safely in bounds (this actually is what happens most of the time

with dispersion error). We therefore want a correction that takes mass away from $i-1$ and $i+1$ and moves it to i to make up the deficit. We know that for cell i the minimum change in mass and therefore the minimum correction that will satisfy boundedness is $\delta\rho_i = \rho_{min} - \rho_i^*$. The operator $\mathcal{L}$ takes the form of the standard discrete Laplacian. The correction for cell i is simply

$$
\begin{aligned}
\rho_i &= \rho_i^* + \delta\rho_i \\
&= \rho_i^* + \rho_{min} - \rho_i^* \\
&= \rho_i^* + c_i(\rho_{i-1}^* - 2\rho_i^* + \rho_{i+1}^*)
\end{aligned}
\tag{G.2}
$$

Comparing the second and third lines, we find that the diffusion coefficient is given by

$$
c_i = \frac{\rho_{min} - \rho_i^*}{\rho_{i-1}^* - 2\rho_i^* + \rho_{i+1}^*}
\tag{G.3}
$$

Based on the third line of (G.2), the correction for cell i may be thought of as the sum to two mass fluxes from its neighboring cells. The change in mass of cell i is $\delta m_i = \delta\rho_i V_i$ and is balanced by changes in mass for cells $i-1$ and $i+1$:

$$
\begin{aligned}
\delta m_{i-1} &= -c_i(\rho_{i-1}^* - \rho_i^*)V_i \\
\delta m_{i+1} &= -c_i(\rho_{i+1}^* - \rho_i^*)V_i
\end{aligned}
$$

In this case the sum of the mass corrections is zero, as desired:

$$
\begin{aligned}
\sum_{j=i-1}^{i+1} \delta m_j &= \delta\rho_{i-1}V_{i-1} + \delta\rho_i V_i + \delta\rho_{i+1}V_{i+1} \\
&= -c_i(\rho_{i-1}^* - \rho_i^*)V_i + c_i(\rho_{i-1}^* - 2\rho_i^* + \rho_{i+1}^*)V_i - c_i(\rho_{i+1}^* - \rho_i^*)V_i \\
&= 0
\end{aligned}
$$

Realistic cases

The discussion above was to provide a simple case for understanding the basic idea behind the correction method. In a realistic case we must account for multi-dimensional aspects of the problem and for the possibility that neighboring cells may both be out of bounds. Here again we examine the case of a minimum density boundedness violation. Consider the cell $n = \{i, j, k\}$ in a 3D flow with volume V_n and density ρ_n^* obtained from the transport scheme. Let N denote the set of cells containing n and its neighbors excluding diagonal neighbors (in other words, only include cells which share a face with n). We want to correct any boundedness violations for the nth cell via

$$
\rho_n = \rho_n^* + \delta\rho_n
\tag{G.4}
$$

Let $\delta\rho_{mn}$ denote the density change for cell m in N (the neighborhood of n) due to a boundedness violation in n. We obtain the final correction for cell n by

$$
\delta\rho_n = \sum_{m \in \mathsf{N}} \delta\rho_{nm}
\tag{G.5}
$$

where

$$
\delta\rho_{mn} = \begin{cases} \max(0, \rho_{min} - \rho_n^*) & \text{if} \quad m = n \\ -c_n(\max[\rho_{min}, \rho_m^*] - \max[\rho_{min}, \rho_n^*])\dfrac{V_n}{V_m} & \text{if} \quad m \neq n \end{cases}
\tag{G.6}
$$

The smoothing parameter in (G.6) is obtained from

$$
c_n = \frac{\max(0, \rho_{min} - \rho_n^*)}{\sum_{s \in \mathsf{N}, s \neq n}(\max[\rho_{min}, \rho_s^*] - \max[\rho_{min}, \rho_n^*])}
\tag{G.7}
$$